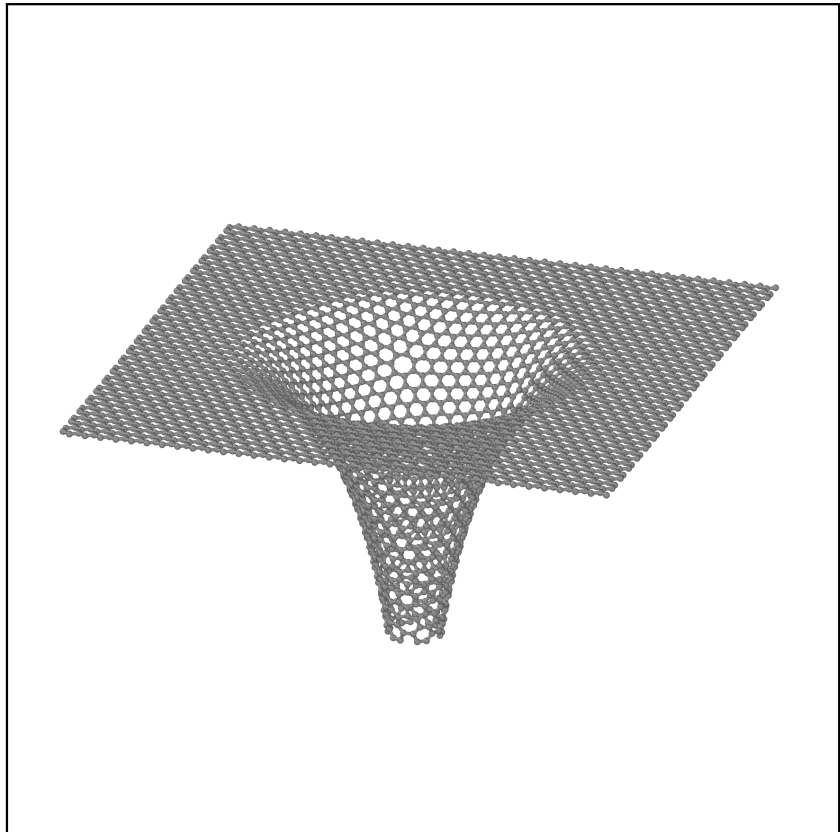




Tommaso Morresi

From atoms to extended structures via ab-initio and multi-scale simulations



UNIVERSITY OF TRENTO - Italy
Department of Civil, Environmental
and Mechanical Engineering



Doctoral School in Civil, Environmental and Mechanical Engineering
Topic 3. Modelling and Simulation - XXXI cycle 2015/2018

Doctoral Thesis - May 2019

Tommaso Morresi

From atoms to extended structures via ab-initio and multi-scale simulations

Supervisors

Prof. Nicola M. Pugno - University of Trento
Dr. Simone Taioli - FBK (ECT*)



Contents on this book are licensed under a Creative Common Attribution
Non Commercial - No Derivatives
4.0 International License, except for the parts already published by other publishers.

University of Trento
Doctoral School in Civil, Environmental and Mechanical Engineering
<http://web.unitn.it/en/dricam>
Via Mesiano 77, I-38123 Trento
Tel. +39 0461 282670 / 2611 - dicamphd@unitn.it



Abstract

This thesis deals with the theoretical and computational modelling of materials by using a variety of multi-scale approaches to accurately predict the properties of realistic structures. In particular, we analyse a number of known and novel carbon-based materials, exploiting the unique versatility of carbon to bind into several bonding configurations, with the aim of tailoring their electronic and mechanical characteristics.

In this regard, the methods used to carry out electronic structure simulations depend on the system size: from the Dirac-Hartree-Fock (DHF) approach to model molecular properties, where systems are composed by few atoms only, to Density Functional Theory (DFT) used for periodic solids, such as diamond and graphene-related materials composed by a few to some hundred of atoms, to Density Functional Tight Binding (DFTB) or plane Tight Binding (TB) to study nanowires or Beltrami pseudospheres, which are composed by some hundreds to a few millions atoms. We have chosen to introduce the details of these methods where they are used, and not to describe them in a separate introductory chapter.

The knowledge of the electronic structure is of paramount importance also for describing the macroscopic response of materials, e.g. to external electromagnetic or force fields. In this respect, a fundamental observable connecting the microscopic and macroscopic scale is provided by the dielectric matrix of the material. The knowledge of the energy and momentum dependent dielectric function gives access to a number of transport properties in solids, which are analysed in this thesis from first-principles and classical Monte Carlo approaches. Furthermore, the mechanical response of materials to external pressure fields is assessed in this thesis from the first-principles simulation of the electronic structure of the material, as well as several relevant derived characteristics, such as the Young's modulus, Poisson's ratio, and the stress-strain curves.

The criterion used in this thesis to present these concepts is to organize the chapters, with the exception of the last one, according to the increasing dimension of the systems. More in details, the first chapter uses the DHF approach to simulate atoms and molecules, such bromotrifluoromethane; the second chapter deals with periodic systems characterized by unit cells with a relatively small number of atoms, such as diamond and graphite; the third one discusses graphene and graphene-related materials with lower density; the fourth one present a new computational and experimental model of silicon carbide nanowires coated with silicon dioxide shell; the fifth chapter is focused on the study of sp^2 -hybridized carbon atoms, arranged on a Beltrami surface. The shape of the latter system has a constant negative Gaussian curvature and represents the counterpart of the fullerene, which has at variance a positive Gaussian curvature. To reproduce the architecture of the carbon pseudosphere in the size range to compare our theoretical predictions with experiments, we devised a method to scale up the structure up to millions of atomic centers, reaching the size of hundreds of nanometers. The latter topic spans different research fields such as geometrical topology (tessellation problem), physics (black-hole analogue) and mechanical engineering (stability of the structure). Finally, the last chapter is dedicated to an on going work and thus only partial results will be shown. This topic deals with the Non-Adiabatic Molecular Dynamics (NAMD) simulation of amorphous silica samples where we couple the nuclear dynamic of the system to the electronic structure.

Acknowledgements

A lot of people must be inserted in this section and I'm sorry if I'm forgetting someone. Also if it's normal sometime to feel lost in its own research, PhD is really a nice and exciting experience. Thus firstly I would like to thank my supervisors Prof. Nicola M. Pugno for his vision, motivation and for the opportunity to work in his group and Dr. Simone Taioli that totally supported my work during the PhD course and helped me get results of better quality. In particular I would like to thank Simone not only for the supervision and for teaching me how to become a researcher, but also for his true friendship that goes beyond science and that was fundamental for the realization of this work. Thanks also to his wife Szuzana, for her hospitality, her dinners and for the beautiful trekking shared in Trentino.

I am also grateful to the head of LISC group Dr. Maurizio Dapor and Dr. Giovanni Garberoglio for their always useful advices and acceptance in this nice group. Thank to ECT which is a fantastic place to make science, to ECT* people and in particular to Dr. Daniele Binosi for the collaboration about the graphene trumpet problem. Then I thank my doctoral colleagues Martina and Andrea for sharing with them the office and every day of these three PhD years; their feedback, cooperation and of course friendship were absolutely fundamental. A special mention also to my master degree thesis advisor Dr. Stefano Simonucci that continues to help me in understanding many physics issues and also because he is really a special person. About science, thank to all the people with which I collaborated: it was exciting to share ideas both with experimentalists and with theoreticians.*

Thank to my Trentino 'family', composed by Andrea, Chiara S. and Chiara C. with which I spent most of the free time and I enjoyed a lot the mountains of Trentino-Alto Adige. Thanks to all my friends of Sanbapolis and to the 'Volontari In Strada' association.

Then I would like to thank all my family which is the basis of my life and every time I go home it's wonderful. Without their support and everything that a family could give, I wouldn't arrive to the end of a PhD.

Finally, thank to Rebecca. My research is focused on computational physics, but the importance of her nearness to me is not computable. So thank for make me feel at least a lucky person.

Contents

Abstract	iv
Acknowledgements	vi
Introduction	1
Publications related to this thesis	9
1 A Dirac-Hartree-Fock approach for atomic and molecular electronic structure calculations	11
1.1 Wavefunction calculation within the mean field Dirac-Hartree-Fock method	12
1.2 Computational methods for the non-spherically symmetric systems . .	14
1.2.1 The Gaussian basis set	14
1.2.2 Mono-electronic integrals	15
1.2.3 Green's function matrix elements	16
1.2.4 The two-step recurrence relation of $G_m(x)$	17
1.2.5 Bi-electronic integrals	18
1.3 Gaussian functions at work: application of the polycentric approach to the electronic structure calculation of molecules	19
1.4 Conclusions	22
2 Ab-initio simulations of dielectric functions and reflection electron energy loss spectra of diamond and graphite	25
2.1 Density Functional Theory in a nutshell	26
2.2 Aim of the work	28
2.3 Experimental details	29
2.4 Computational details	30
2.4.1 Computed observables for charge transport simulations	30
2.4.2 Drude-Lorentz model	31
2.4.3 Ab initio simulations	32
2.4.4 Theory of Monte Carlo simulations	33
2.5 Results and discussion	35
2.5.1 Frequency-dependent dielectric function of diamond and graphite	35
2.5.2 Frequency-dependent energy-loss functions of diamond and graphite	36

2.5.3	Inelastic Mean Free Path and Stopping Power	39
2.6	Monte Carlo simulations	40
2.6.1	Diamond energy-loss spectra	40
2.6.2	Graphite energy-loss spectra	42
2.6.3	Graphite energy-loss spectra taking into account a model of anisotropy crystal directions	44
2.7	Conclusions	47
3	Graphene allotropes with lower densities	53
3.1	Aim of the work	53
3.2	Methods and computational details	54
3.2.1	Augmentation method for lowering the structure density	54
3.2.2	Structure optimization	55
3.2.3	Phonon band structure simulations	56
3.2.4	Electronic band structure and DOS	56
3.2.5	Mechanical properties	56
3.3	Results and discussion	57
3.3.1	Parent and augmented geometries with low density	57
	Graphene and graphene daughter.	57
	Tilene parent and tilene.	57
	Flakene parent and flakene.	59
	Beyond the regular and semi-regular tessellations: the Cairo pentagonal tiling. Liskene and liskene daughter.	59
	Relaxing the locally jammed packing constraint.	60
3.3.2	Structural optimization	60
3.3.3	Phonon band structures	61
3.3.4	Electronic properties	62
3.3.5	Elastic properties	64
3.3.6	Stress-strain curves	71
3.4	Conclusions	74
4	A theoretical model of SiC/SiO_x core/shell nanowire	79
4.1	State of the art and aim of the work	79
4.2	Experimental details	81
4.3	Computational details	82
4.3.1	Modeling of SiC and SiC/SiO _x core/shell NWs	82
	Structure of the SiC core	82
	Surface passivation of the SiC core	82
	SiC/SiO _x core/shell nanowire	85
	Characterization of bond lengths and angles of the SiC/SiO _x core/shell NW model	88
4.3.2	Electronic structure simulations of the SiC/SiO _x core/shell nanowire	88

4.3.3	Simulations of XANES spectra	89
4.4	Results and Discussion	91
4.4.1	Silicon K-edge XANES spectra	91
4.4.2	Oxygen K-edge XANES spectra	95
4.4.3	Carbon K-edge XANES spectra	100
4.5	Conclusions	104
5	Forging graphene pseudospheres to mimic curved space-times	113
5.1	A mathematical, physical and engineering problem	113
5.2	Computational Methods	115
5.2.1	Tiling the Beltrami's pseudosphere by three-coordinated carbon atoms	115
5.2.2	Evaluating the electronic properties of large systems by the Tight Binding plus Kernel Polynomial Method	121
	Multi-Orbital Tight Binding	121
	Kernel Polynomial Method	123
5.3	Results	127
5.3.1	Computational model of the Beltrami's surface tiling	127
5.3.2	The dualization algorithm for three-fold coordinated graphs	130
5.3.3	Density of States simulations	132
	Planar graphene	132
	Planar graphene with a single SW defect	133
	Planar graphene with random SW defect density	134
	LDOS of the extended Beltrami's pseudosphere	136
5.3.4	Is the Beltrami's pseudosphere a condensed matter analogue of a black-hole?	140
5.4	Conclusions	144
6	Future works	149
6.1	Theory of Non Adiabatic Molecular Dynamics	150
6.2	Partial results for different allotropes of SiO ₂	153
	Conclusions	157

List of Abbreviations

AI	Ab Initio
ALDA	Adiabatic Local Density Approximation
BO	Born Oppenheimer
CBM	Conduction Band Minimum
DFT	Density Functional Theory
DFTB	Density Functional based Tight Binding
DHF	Dirac Hartree Fock
DL	Drude Lorentz
DOS	Density Of States
ELF	Energy Loss Function
FWHM	Full Width Half Maximum
GBS	Gaussian Basis Set
HOPG	Highly Oriented Pyrolytic Graphite
IBZ	First Brillouin Zone
ICS	Inelastic Cross Section
IMFP	Inelastic Mean Free Path
KPM	Kernel Polynomial Method
LAPW	Linearized Augmented Plane Wave
LDA	Local Density Approximation
LDOS	Local Density Of States
LFE	Local Field Effects
LR-TDDFT	Linear Response Time Dependent Density Functional Theory
MC	Monte Carlo
MD	Molecular Dynamics
MSD	Mean Square Displacement
NA	Non Adiabatic
NAMD	Non Adiabatic Molecular Dynamics
NW	Nanowire
PDOS	Projected Density of States
REELS	Reflection Electron Energy Loss Spectrum
RPA	Random Phase Approximation
SP	Stopping Power
SW	Stone Wales

TB	Tight Binding
TDDFT	Time Dependent Density Functional Theory
TDOS	Total Density Of States
TEM	Transmission Electron Microscopy
TEY	Total Electron Yield
VBM	Valence Band Maximum
XANES	X-Ray Near Edge Absorption Spectra

Introduction

Computational science represents a tool of paramount importance for investigating complex phenomena emerging at different scales in systems relevant to fundamental physics and engineering. Indeed, computational methods have become nowadays the standard approach to prototype novel ideas in several fields of science. In particular, a fundamental branch of computational science is the modeling and prediction of material's properties by first-principles (or *ab-initio*) methods, i.e. a body of techniques that do not need the introduction of external parameters or information derived from experiments. *Ab initio* methods can be completely derived by the basic axioms of the quantum theory and they just involve several layers of approximation to solve the basic equations that are completely under control.

Following the Moore's trend of modern computers, whose computational power increases linearly over the years in terms of number of operations delivered per second, this research area is constantly under development. These advances are related to both numerical accuracy and algorithms. However, the definitive answer to the solution of the many-body problem, despite some novel approaches based on artificial intelligence, or the future advent of quantum computers which can possibly deliver a more comprehensive view on this issue, is still hampered by two major factors, that are i) the complexity exponentially growing with the number of particles basically due to the correlation, and ii) the dimensionality. In particular, the latter element affects dramatically the physical properties of materials owing to the different way that Coulomb repulsion acts upon the electrons in three-dimensional (3D), two-dimensional (2D), one-dimensional (1D), and molecular (0D) structures. Indeed, the presence of constraints on the particle's motion in one or more degrees of freedom leads to remarkable consequences, such as quantum confinement, anisotropic characteristics and new phases. These effects can completely modify the properties that low-dimensional physical systems exhibit with respect to their bulk counterparts. Additionally, quantum objects do interfere with one another, so that the quantum state of a many-body system is the result of the interaction between its constituent particles. This many-body potential depends on dimensionality and confinement, and thus is much more than the simple sum of the interaction between its building blocks. This concept was masterly described by Philip W. Anderson in his article "More is different" [1], where he argues that "the behaviour of large and complex aggregations of elementary particles, it turns out, is not to be understood in terms of a simple extrapolation of the properties of a few particles. Instead at each level

of complexity entirely new properties appear...". In this regard for example, while at angstrom scale it is hard to differentiate between 0D point-like atomic species, such as tantalum or niobium, nevertheless at 3D macroscale the former is a lustrous transition metal while the latter undergoes a phase transition to a BCS-type II superconductor at 9.26 K. This means that at the time we reach the microscale, electrons of Nb pair up in Cooper pairs and condensate, transforming the materials in a superconductor characterized by zero-resistance conductivity.

On the other side, from the beginning of the 20th century several theoretical methods adopting different approximations were proposed to tackle the correlation problem, starting from the Thomas-Fermi model (1927) and the density functional theory introduced by Hohenberg and Kohn in 1964. Based on these theoretical frameworks, a variety of computational approaches have been developed to deal accurately with the Coulomb repulsion in single atoms to molecular assembly and structures containing even millions of atoms. Using these approaches, the electronic structure equations and the nuclear (ionic) motion problem can be approximated, so that one can nowadays safely predict many electronic and mechanical properties of materials.

In this thesis we deal mainly with the solution of the electronic structure problem and related quantities for a variety of systems, most notably carbon-based materials. Indeed, carbon is one of the most versatile chemical elements: its relatively small atomic radius and the tetravalent character mean that carbon can easily form covalent bonds with several chemical elements, including itself, also at room conditions [2, 3, 4, 5]. This is the very reason why the number of known chemical compounds constituted of carbon – which is only the fourth most abundant element in the universe by mass after hydrogen, helium, and oxygen, and only the 15th most abundant in the Earth's crust – is by far higher than the sum of all the others (in excess of 10 million). For example, at odds, silicon is another element in group 14 of the periodic table having also four valence electrons which can bind into both molecular and crystalline compounds. However, due to its atomic radius 1.5 times larger than that of carbon, Si is too big to fit together into as great a variety of molecules as carbon atoms can. This remarkable ability of carbon to bind in different ways by sharing from one single to four electrons may lead to the formation of single to triple bonds. This makes for an enormous number of possible bond combinations forming straight chains, such as polymers, rings, such as aromatic hydrocarbons, crystals, such as silicon carbide, and also amorphous phases. The all-carbon materials that carbon can form by binding in different ways are called allotropes of carbon, be those naturally available or man-made. The most common are graphite, diamond, fullerene, and amorphous carbon. In this thesis, we will focus on the description of the physical properties of carbon allotropes with the aim to show how the dimensionality leaves its signature on the electronic, optical, and mechanical properties of these carbon-based materials. For example, on the one side graphite is a quasi-two-dimensional material whose distinctive traits are to be opaque, black, and sufficiently soft to be used in pencils. Furthermore, graphite is a good electrical conductor. On the other side diamond is

a 3D transparent, hard solid showing low electrical conductivity. Nevertheless, at room conditions, 3D diamond, 1D carbon nanotubes, and 2D graphene have all large thermal conductivities.

In this thesis we present several results obtained by using first-principles and multiscale simulations on the electronic, mechanical, and optical properties of carbon-based materials at different level of aggregation. These results are generally compared with experiments recorded in-house or available in the literature. We chose not to present the theoretical and computational methods in one separate chapter, but to thoroughly discuss their fundamentals and application when used, avoiding unnecessary details.

In particular, in the first chapter we study a few molecules containing carbon relevant in astrophysical scenarios (HMgNC, MgNCO, MgCN and MgNC) and in environmental sciences (CF₃Br). These systems are composed only by three to five atoms and their electronic structure is assessed by solving the Dirac-Hartree-Fock (DHF) equations to include relativistic effects. We use a Gaussian basis set (GBS), which turns out to be useful for treating polycentric systems. This method, which will be discussed in detail in chapter 1, can deal with non-spherical non-periodic systems composed by a few atoms.

In the second and third chapters we investigate periodic carbon-based systems with small unit cells. In particular, in the second chapter we calculate the dielectric ($\epsilon(\mathbf{q}, \omega)$) and energy loss ($ELF = Im[-\frac{1}{\epsilon(\mathbf{q}, \omega)}]$) functions of diamond and graphite. These are pure materials properties and can be derived from the electronic wavefunctions assessed by solving the many-electron problem. Dielectric functions are key physical quantities as they are intimately related to the response of a system perturbed via external probes, such as electron or photon beams. The dielectric and energy loss functions of graphite and diamond were calculated within the framework of DFT and then used as input for Monte Carlo (MC) simulations of the charge transport in these solids to interpret the experimental spectra of back-scattered electrons [6, 7, 8]. The specific goal of our analysis was to unravel the impact of different theoretical approaches for calculating the dielectric functions, comparing ab-initio methods with other semi-classical models, such as the Drude-Lorentz approach. We found out that it is necessary to go beyond the optical limit ($|\mathbf{q}| \rightarrow 0$) in the calculation of dielectric function of insulator systems, such as diamond, to accurately reproduce energy loss spectra and that the widely used Random Phase Approximation (RPA) can be used successfully only for metal or semi-metal, such as graphite.

In the third chapter we deal with novel bi-dimensional structures using graphene geometry as a texture. Over the last decade graphene is arguably one of the most investigated materials among all the existing carbon allotropic forms [9, 10, 11, 12, 13]. Nevertheless, the possibility to introduce new interesting features also in 2D carbon-based materials without chemical functionalization, while keeping the desirable properties of graphene, such as its planar periodic structure and the sp^2 bonding network, might be very convenient to the existing technology. In this chapter thus

we report an approach for finding novel energetically stable structures characterized by sp^2 -bonded carbon atoms of decreasing density using graphene as a frame of reference. In particular, we aim to find planar structures with density lower than graphene, possibly decreasing it up to the least dense form of carbon allotrope that could ever be synthesized under the locally jammed packing condition, while displaying almost unchanged specific mechanical characteristics with respect to graphene. Then, we fully characterized these new 2D materials by computing i) the electronic properties, such as band structure and Density Of States (DOS); ii) the mechanical properties, such as the Young's modulus and the Poisson's ratio, derived from the elastic coefficients of the stiffness matrix; iii) finally the stress-strain curves from which we gain information on ultimate strength, fracture strain and toughness of the systems. These calculations were performed again within the DFT framework, and computational details are reported in this chapter.

In the fourth chapter we present a computational model of a SiC/SiO_x core/shell nanowire (NW), which we use to reproduce in-house acquired X-ray absorption experimental spectra. The relevance of SiC/SiO_x core/shell NWs is related to the discovery that this system, coated with light-absorbing organic molecules (so-called photosensitizers), can be efficiently applied to anti-cancer therapies using X-ray excitation [14] (photodynamic therapy). The work reported in this chapter is aimed at the theoretical understanding of the phenomena underlying these processes. Unfortunately, the simulation supercell of this NW is made by a few hundred of atoms. Thus, we decided to use a combined DFT/Density Functional Tight Binding (DFTB) approach to overcome the unfavourable scaling with system size of first-principles methods. In particular, DFTB was used to build the atomistic model of the NW and to study the NWs characterised by different radii and surface terminations, while by DFT we computed the X-ray absorption spectra.

In the fifth chapter we study the physics of graphene arranged in the shape of a Beltrami's pseudosphere. This work stems from previous investigations on black-hole analogue systems [15, 16, 17], where it is shown from analytical calculations that a graphene sheet arranged in this particular form can be used to test the physics of curved space-times with a singularity (event horizon), and in particular some specific outcomes, such as the Hawking-Unruh effect. The latter states that the ground state of an inertial observer is seen in thermodynamic equilibrium with a non-zero temperature by a uniformly accelerating observer. Thus, a quantum field in a space-time with an horizon should exhibit a thermal character. Our goal is to perform a *computational experiment* to reproduce the theoretical prediction on a realistic Beltrami's geometry. To do so, we first build the geometrical model of the Beltrami's pseudosphere by tiling the hyperbolic surface with polygons, and second we derive the electronic properties of the system, and in particular the local density of state (LDOS), which is a quantity closely related to the Hawking-Unruh effect. In this respect, in order to have a large wavelength of the electrons, able to feel the curvature, we had to solve the difficult task of achieving a ratio between the pseudosphere radius R_p

and the interatomic distance in graphene l (1.42 \AA) $\frac{R_p}{l} \gg 1$. This means that the structure must be extremely large. Typically, this results in structures containing millions of carbon atoms, which cannot be treated by standard, needless to say *ab-initio*, approaches. Thus, in this chapter we discuss a multiscale method developed to scale up the pseudosphere dimension, building structures with such an high number of particles. Our method can be easily generalized, at least for graphenic structures. Finally, a second challenge is to simulate the LDOS of these enormous structures for different radii of the pseudosphere. A suitable approach to deal with this issue is the Tight Binding (TB) method, which has been used along with the Kernel Polynomial Method (KPM) to expand the DOS in terms of Chebyshev polynomials [18]. These two methods, thoroughly explained in this fifth chapter, made the electronic structure simulations a computationally feasible task. At the end of the chapter, we argue in which sense the Beltrami's pseudosphere can be considered a black-hole analogue.

Finally, the last chapter is dedicated to a work that is on going at the time of submitting this thesis. This work is about Non-Adiabatic Molecular Dynamics (NAMD) simulations of amorphous silica samples. In particular, we are interested in the influence that electronic excitations could have on the nuclear dynamics of the SiO_2 sample at room temperature. We are considering different kinds of amorphousness and we will show the complexity of studying non-crystal systems by *ab-initio* methods. Results of these simulations are only partial and currently we are trying to achieve better outcomes.

Bibliography

- [1] P. W. Anderson, More is different, *Science* 177 (4047) (1972) 393–396. arXiv:<http://science.sciencemag.org/content/177/4047/393.full.pdf>, doi:10.1126/science.177.4047.393.
URL <http://science.sciencemag.org/content/177/4047/393>
- [2] E. H. Falcao, F. Wudl, Carbon allotropes: beyond graphite and diamond, *Journal of Chemical Technology & Biotechnology* 82 (6) (2007) 524–531. arXiv:<https://onlinelibrary.wiley.com/doi/pdf/10.1002/jctb.1693>, doi:10.1002/jctb.1693.
URL <https://onlinelibrary.wiley.com/doi/abs/10.1002/jctb.1693>
- [3] S. Taioli, P. Umari, M. De Souza, Electronic properties of extended graphene nanomaterials from gw calculations, *physica status solidi (b)* 246 (11-12) (2009) 2572–2576.
- [4] A. Pedrielli, S. Taioli, G. Garberoglio, N. Pugno, Mechanical and thermal properties of graphene random nanofoams via molecular dynamics simulations, *Carbon* 132 (2018) 766–775.

- [5] M. Itoh, M. Kotani, H. Naito, T. Sunada, Y. Kawazoe, T. Adschiri, New metallic carbon crystal, *Physical review letters* 102 (2009) 055703. doi:10.1103/PhysRevLett.102.055703.
- [6] S. Taioli, S. Simonucci, L. Calliari, M. Dapor, Electron spectroscopies and inelastic processes in nanoclusters and solids: theory and experiment, *Physics Reports* 493 (5) (2010) 237–319.
- [7] D. Emfietzoglou, I. Kyriakou, I. Abril, R. Garcia-Molina, I. Petsalakis, H. Nikjoo, A. Pathak, Electron inelastic mean free paths in biological matter based on dielectric theory and local-field corrections, *Nuclear Instruments and Methods in Physics Research Section B: Beam Interactions with Materials and Atoms* 267 (1) (2009) 45 – 52. doi:<https://doi.org/10.1016/j.nimb.2008.11.008>.
URL <http://www.sciencedirect.com/science/article/pii/S0168583X08012718>
- [8] M. Dapor, *Electron-Beam Interactions with Solids: Application of the Monte Carlo Method to Electron Scattering Problems*, Springer Tracts in Modern Physics, Springer Berlin Heidelberg, 2003.
URL <https://books.google.it/books?id=h71sCQAAQBAJ>
- [9] A. K. Geim, K. S. Novoselov, The rise of graphene, *Nature Materials* 6 (3) (2007) 183–191. doi:10.1038/nmat1849.
URL <https://doi.org/10.1038/nmat1849>
- [10] L.-C. Xu, R.-Z. Wang, M.-S. Miao, X.-L. Wei, Y.-P. Chen, H. Yan, W.-M. Lau, L.-M. Liu, Y.-M. Ma, Two dimensional dirac carbon allotropes from graphene, *Nanoscale* 6 (2014) 1113–1118. doi:10.1039/C3NR04463G.
URL <http://dx.doi.org/10.1039/C3NR04463G>
- [11] R. Tatti, L. Aversa, R. Verucchi, E. Cavaliere, G. Garberoglio, N. M. Pugno, G. Speranza, S. Taioli, Synthesis of single layer graphene on cu (111) by c 60 supersonic molecular beam epitaxy, *RSC Advances* 6 (44) (2016) 37982–37993.
- [12] S. Taioli, Computational study of graphene growth on copper by first-principles and kinetic monte carlo calculations, *Journal of molecular modeling* 20 (7) (2014) 2260.
- [13] D. Haberer, L. Petaccia, M. Farjam, S. Taioli, S. Jafari, A. Nefedov, W. Zhang, L. Calliari, G. Scarduelli, B. Dora, et al., Direct observation of a dispersionless impurity band in hydrogenated graphene, *Physical Review B* 83 (16) (2011) 165433.
- [14] F. Rossi, E. Bedogni, F. Bigi, T. Rimoldi, L. Cristofolini, S. Pinelli, R. Alinovi, M. Negri, S. C. Dhanabalan, G. Attolini, F. Fabbri, M. Goldoni, A. Mutti, G. Benecchi, C. Ghetti, S. Iannotta, G. Salviati, Porphyrin conjugated sic/siox

- nanowires for x-ray-excited photodynamic therapy, *Sci Rep* 5 (2015) 7606. doi: 10.1038/srep07606.
- [15] A. Iorio, G. Lambiase, Quantum field theory in curved graphene spacetimes, lobachevsky geometry, weyl symmetry, hawking effect, and all that, *Phys. Rev. D* 90 (2014) 025006. doi:10.1103/PhysRevD.90.025006.
URL <https://link.aps.org/doi/10.1103/PhysRevD.90.025006>
- [16] A. Iorio, G. Lambiase, The hawking-unruh phenomenon on graphene, *Physics Letters B* 716 (2) (2012) 334 – 337. doi:10.1016/j.physletb.2012.08.023.
URL <http://www.sciencedirect.com/science/article/pii/S037026931200860X>
- [17] S. Taioli, R. Gabbrielli, S. Simonucci, N. M. Pugno, A. Iorio, Lobachevsky crystallography made real through carbon pseudospheres, *Journal of Physics: Condensed Matter* 28 (13) (2016) 13LT01.
URL <http://stacks.iop.org/0953-8984/28/i=13/a=13LT01>
- [18] A. Weiße, G. Wellein, A. Alvermann, H. Fehske, The kernel polynomial method, *Rev. Mod. Phys.* 78 (2006) 275–306. doi:10.1103/RevModPhys.78.275.
URL <https://link.aps.org/doi/10.1103/RevModPhys.78.275>

Publications related to this thesis

Every chapter of this thesis, with the exception of the sixth one, is related to a published paper or a submitted paper.

In particular:

- Chapter 1: *reference* [1]; this article gained the journal cover (<https://onlinelibrary.wiley.com/doi/10.1002/adts.201870030>).
- Chapter 2: *references* [2, 3];
- Chapter 3: *submitted to '2D Materials' (IOP)* [4];
- Chapter 4: *reference* [5];
- Chapter 5: [6].

Bibliography

- [1] T. Morresi, S. Taioli, S. Simonucci, Relativistic theory and ab initio simulations of electroweak decay spectra in medium-heavy nuclei and of atomic and molecular electronic structure, *Advanced Theory and Simulations* 1 (11) (2018) 1800086. arXiv:<https://onlinelibrary.wiley.com/doi/pdf/10.1002/adts.201800086>, doi:10.1002/adts.201800086. URL <https://onlinelibrary.wiley.com/doi/abs/10.1002/adts.201800086>
- [2] M. Azzolini, T. Morresi, G. Garberoglio, L. Calliari, N. M. Pugno, S. Taioli, M. Dapor, Monte carlo simulations of measured electron energy-loss spectra of diamond and graphite: Role of dielectric-response models, *Carbon* 118 (2017) 299 – 309. doi:<https://doi.org/10.1016/j.carbon.2017.03.041>. URL <http://www.sciencedirect.com/science/article/pii/S0008622317302816>
- [3] M. Azzolini, T. Morresi, K. Abrams, R. Masters, N. Stehling, C. Rodenburg, N. M. Pugno, S. Taioli, M. Dapor, Anisotropic approach for simulating electron transport in layered materials: Computational and experimental study of

- highly oriented pyrolytic graphite, *The Journal of Physical Chemistry C* 122 (18) (2018) 10159–10166. arXiv:<https://doi.org/10.1021/acs.jpcc.8b02256>, doi: 10.1021/acs.jpcc.8b02256.
URL <https://doi.org/10.1021/acs.jpcc.8b02256>
- [4] T. Morresi, A. Pedrielli, S. A. Beccara, R. Gabbrielli, N. M. Pugno, S. Taioli, Structural, electronic and mechanical properties of all-sp² graphene allotropes: the specific strength of tilene parent is higher than that of graphene and flakene has the minimal density, arXiv preprint arXiv:1811.01112.
- [5] T. Morresi, M. Timpel, A. Pedrielli, G. Garberoglio, R. Tatti, R. Verucchi, L. Pasquali, N. M. Pugno, M. V. Nardi, S. Taioli, A novel combined experimental and multiscale theoretical approach to unravel the structure of sic/siox core/shell nanowires for their optimal design, *Nanoscale* 10 (2018) 13449–13461. doi:10.1039/C8NR03712D.
URL <http://dx.doi.org/10.1039/C8NR03712D>
- [6] T. Morresi, R. Piergallini, S. Roche, D. Binosi, N. M. Pugno, S. Simonucci, S. Taioli, Forging graphene pseudospheres to mimic curved space-times, to be submitted soon (2019).

Chapter 1

A Dirac-Hartree-Fock approach for atomic and molecular electronic structure calculations

The relativistic extension of quantum mechanics for many-electron systems, such as atoms to molecules and solids, represents the most fundamental theory of all molecular sciences. Indeed, it combines the laws of special relativity, to which natural systems must obey, with the realm of quantum mechanical concepts. In this chapter, aiming at finding a numerical solution of the Dirac-Hartree-Fock (DHF) equations, we describe our theoretical and computational approach to relativistic quantum mechanics using Gaussian basis sets. The description is kept as general as possible, so to be able to deal with different types of interactions, not limited to the Coulomb potential but including e.g. the Yukawa potential used in nuclear physics applications (for which our work on beta-decay of medium to heavy nuclei was initially devised). However, the application to nuclear physics, for which we refer the reader to our publication for further details [1], goes beyond the scope of this thesis: thus, here we report only the theory and relevant computational details with a few results on molecules.

Here we stress that in order to describe the chemistry of the atomic bonds within a molecule, a relativistic approach in principle is not necessary, as the valence shell electrons can be described accurately also by Schrödinger equation adding "by hand" a spin-orbit coupling term to the equation. However, this "phenomenological" approach fails when the molecular systems are characterized by the presence of heavy atomic species. Indeed, in this case a rigorous bi-spinorial approach is mandatory as the small or lower part of the bispinor cannot be neglected. Furthermore, this way of proceeding can be easily extended to describe phenomena induced by forces other than the Coulomb interaction, such the ElectroWeak force driving the beta-decay in

atomic and molecular systems. Following this formalism the spin-orbit coupling and fine structure properties are rigorously taken into account.

The methodological approach here described has been awarded the journal cover of *Advanced Theory & Simulations*.

1.1 Wavefunction calculation within the mean field Dirac-Hartree-Fock method

The time independent Dirac Hamiltonian of a many particles system can be written as follows [2]:

$$\left[\sum_i \left(c\alpha_i \cdot \mathbf{p}_i + \beta_i mc^2 + V_i \right) + \sum_{i < j} \left(1 - \alpha_i \cdot \alpha_j \right) g_{ij} \right] \psi(\mathbf{r}_1, \dots, \mathbf{r}_N) = E\psi(\mathbf{r}_1, \dots, \mathbf{r}_N) \quad (1.1)$$

In the case of two different types of interactions, e.g. represented by scalar (g_S) and vector (g_V) potentials, the Dirac equation reads:

$$\left\{ \sum_i \left(c\alpha_i \cdot \mathbf{p}_i + \beta_i mc^2 + V_i \right) + \sum_{i < j} \left[\beta_i \beta_j g_{S,ij} + \left(1 - \alpha_i \cdot \alpha_j \right) g_{V,ij} \right] \right\} \psi(\mathbf{r}_1, \dots, \mathbf{r}_N) = E\psi(\mathbf{r}_1, \dots, \mathbf{r}_N) \quad (1.2)$$

which in second quantization can be written as follows:

$$\begin{aligned} H = & \sum_{s_1 s_2} \int d\mathbf{r} \hat{\psi}_{s_1}^+(\mathbf{r}) \left[-ic\alpha_{s_1 s_2} \cdot \nabla + \beta_{s_1 s_2} mc^2 + \delta_{s_1 s_2} V(\mathbf{r}) \right] \hat{\psi}_{s_2}(\mathbf{r}) + \\ & + \frac{1}{2} \sum_{s_1 s_2 s'_1 s'_2} \int d\mathbf{r} d\mathbf{r}' \hat{\psi}_{s_1}^+(\mathbf{r}) \hat{\psi}_{s'_1}^+(\mathbf{r}') \left[\beta_{s_1 s_2} \beta_{s'_1 s'_2} g_S(\mathbf{r}, \mathbf{r}') + \left(\delta_{s_1 s_2} \delta_{s'_1 s'_2} - \alpha_{s_1 s_2} \cdot \alpha'_{s'_1 s'_2} \right) g_V(\mathbf{r}, \mathbf{r}') \right] \hat{\psi}_{s'_2}(\mathbf{r}') \hat{\psi}_{s_2}(\mathbf{r}) \end{aligned} \quad (1.3)$$

where s_1, s_2, s'_1, s'_2 index the two components of the bispinor. We notice that Equation (1.3) is totally general as g_S and g_V may represent different types of scalar or vector interactions respectively. The Hartree-Fock approximation of the Hamiltonian (1.3) can be introduced by assuming that the average value of the field operator can be factorized as follows:

$$\langle \hat{\psi}_{s_1}^+(\mathbf{r}) \hat{\psi}_{s'_1}^+(\mathbf{r}') \hat{\psi}_{s_2}(\mathbf{r}) \hat{\psi}_{s'_2}(\mathbf{r}') \rangle = \langle \hat{\psi}_{s_1}^+(\mathbf{r}) \hat{\psi}_{s_2}(\mathbf{r}) \rangle \langle \hat{\psi}_{s'_1}^+(\mathbf{r}') \hat{\psi}_{s'_2}(\mathbf{r}') \rangle - \langle \hat{\psi}_{s_1}^+(\mathbf{r}) \hat{\psi}_{s'_2}(\mathbf{r}') \rangle \langle \hat{\psi}_{s'_1}^+(\mathbf{r}') \hat{\psi}_{s_2}(\mathbf{r}) \rangle \quad (1.4)$$

By defining the 4×4 density matrix at \mathbf{r}, \mathbf{r}' as:

$$\rho_{s'_2 s_1}(\mathbf{r}', \mathbf{r}) = \langle \hat{\psi}_{s_1}^+(\mathbf{r}) \hat{\psi}_{s'_2}(\mathbf{r}') \rangle \quad (1.5)$$

the second quantized form of the Dirac-Hartree-Fock Hamiltonian can be written as:

$$\begin{aligned} H_{DHF} = \sum_{s_1 s_2} \int d\mathbf{r} \hat{\psi}_{s_1}^+(\mathbf{r}) \left\{ -\alpha_{s_1 s_2} \cdot [ic\nabla + \mathbf{A}_H(\mathbf{r})] + \beta_{s_1 s_2} [mc^2 + V_{HS}(\mathbf{r})] + \delta_{s_1 s_2} [V(\mathbf{r}) + V_H(\mathbf{r})] \right\} \hat{\psi}_{s_2}(\mathbf{r}) \\ - \sum_{s'_1 s'_2} \int d\mathbf{r} d\mathbf{r}' \hat{\psi}_{s'_1}^+(\mathbf{r}') \left[V_{FS, s'_1 s'_2}(\mathbf{r}', \mathbf{r}) - A_{F, s'_1 s'_2}(\mathbf{r}', \mathbf{r}) + V_{F, s'_1 s'_2}(\mathbf{r}', \mathbf{r}) \right] \hat{\psi}_{s'_2}(\mathbf{r}) \end{aligned} \quad (1.6)$$

where

$$\begin{aligned} \mathbf{A}_H(\mathbf{r}) &= \int d\mathbf{r}' \sum_{s'_1 s'_2} \left[\rho_{s'_2 s'_1}(\mathbf{r}', \mathbf{r}') \alpha_{s'_1 s'_2} \right] g_V(\mathbf{r}, \mathbf{r}') \\ V_H(\mathbf{r}) &= \int d\mathbf{r}' \sum_{s'_1 s'_2} \left[\rho_{s'_2 s'_1}(\mathbf{r}', \mathbf{r}') \delta_{s'_1 s'_2} \right] g_V(\mathbf{r}, \mathbf{r}') \\ V_{HS}(\mathbf{r}) &= \int d\mathbf{r}' \sum_{s'_1 s'_2} \left[\rho_{s'_2 s'_1}(\mathbf{r}', \mathbf{r}') \beta_{s'_1 s'_2} \right] g_S(\mathbf{r}, \mathbf{r}') \end{aligned} \quad (1.7)$$

and

$$\begin{aligned} A_{F, s'_1 s'_2}(\mathbf{r}', \mathbf{r}) &= \sum_{s_1 s'_2} \alpha_{s_1 s_2} \cdot \alpha_{s'_1 s'_2} \rho_{s'_2 s_1}(\mathbf{r}, \mathbf{r}') g_V(\mathbf{r}, \mathbf{r}') \\ V_{F, s'_1 s'_2}(\mathbf{r}', \mathbf{r}) &= \sum_{s_1 s'_2} \delta_{s_1 s_2} \delta_{s'_1 s'_2} \rho_{s'_2 s_1}(\mathbf{r}, \mathbf{r}') g_V(\mathbf{r}, \mathbf{r}') \\ V_{FS, s'_1 s'_2}(\mathbf{r}', \mathbf{r}) &= \sum_{s_1 s'_2} \beta_{s_1 s_2} \beta_{s'_1 s'_2} \rho_{s'_2 s_1}(\mathbf{r}, \mathbf{r}') g_S(\mathbf{r}, \mathbf{r}') \end{aligned} \quad (1.8)$$

In Equations (1.8) the sums on bi-spinorial indices s_1 and s'_2 can be treated as matrix products. By writing the density matrix as a 2×2 bloc matrix

$$\rho(\mathbf{r}', \mathbf{r}) = \begin{pmatrix} \rho_{LL}(\mathbf{r}', \mathbf{r}) & \rho_{LS}(\mathbf{r}', \mathbf{r}) \\ \rho_{SL}(\mathbf{r}', \mathbf{r}) & \rho_{SS}(\mathbf{r}', \mathbf{r}) \end{pmatrix} \quad (1.9)$$

where L (S) label the 'large' or up (smaller or down) part of the Dirac spinor we obtain:

$$\begin{aligned} A_F(\mathbf{r}', \mathbf{r}) &= \begin{pmatrix} 0 & \sigma \\ \sigma & 0 \end{pmatrix} \cdot \begin{pmatrix} \rho_{LL}(\mathbf{r}', \mathbf{r}) & \rho_{LS}(\mathbf{r}', \mathbf{r}) \\ \rho_{SL}(\mathbf{r}', \mathbf{r}) & \rho_{SS}(\mathbf{r}', \mathbf{r}) \end{pmatrix} \cdot \begin{pmatrix} 0 & \sigma \\ \sigma & 0 \end{pmatrix} g_V(\mathbf{r}', \mathbf{r}) \\ &= \begin{pmatrix} \sigma \cdot \rho_{SS}(\mathbf{r}', \mathbf{r}) \cdot \sigma & \sigma \cdot \rho_{LS}(\mathbf{r}', \mathbf{r}) \cdot \sigma \\ \sigma \cdot \rho_{SL}(\mathbf{r}', \mathbf{r}) \cdot \sigma & \sigma \cdot \rho_{LL}(\mathbf{r}', \mathbf{r}) \cdot \sigma \end{pmatrix} g_V(\mathbf{r}', \mathbf{r}) \end{aligned} \quad (1.10)$$

$$V_{FS}(\mathbf{r}', \mathbf{r}) = \begin{pmatrix} \rho_{LL}(\mathbf{r}', \mathbf{r}) & \rho_{SL}(\mathbf{r}', \mathbf{r}) \\ \rho_{LS}(\mathbf{r}', \mathbf{r}) & \rho_{SS}(\mathbf{r}', \mathbf{r}) \end{pmatrix} g_V(\mathbf{r}', \mathbf{r}) \quad (1.11)$$

$$\begin{aligned} V_S(\mathbf{r}', \mathbf{r}) &= \begin{pmatrix} 1 & 0 \\ 0 & -1 \end{pmatrix} \cdot \begin{pmatrix} \rho_{LL}(\mathbf{r}', \mathbf{r}) & \rho_{LS}(\mathbf{r}', \mathbf{r}) \\ \rho_{SL}(\mathbf{r}', \mathbf{r}) & \rho_{SS}(\mathbf{r}', \mathbf{r}) \end{pmatrix} \cdot \begin{pmatrix} 1 & 0 \\ 0 & -1 \end{pmatrix} g_S(\mathbf{r}', \mathbf{r}) \\ &= \begin{pmatrix} \rho_{LL}(\mathbf{r}', \mathbf{r}) & -\rho_{SL}(\mathbf{r}', \mathbf{r}) \\ -\rho_{LS}(\mathbf{r}', \mathbf{r}) & \rho_{SS}(\mathbf{r}', \mathbf{r}) \end{pmatrix} g_S(\mathbf{r}', \mathbf{r}) \end{aligned} \quad (1.12)$$

With these definitions, Equation (1.6) can be explicitly written as a generalized Dirac equation of the following type:

$$\begin{pmatrix} mc^2 + W_V + W_S + \mathbf{A}_P \cdot \boldsymbol{\sigma} - E & -c\boldsymbol{\sigma} \cdot i\nabla - \boldsymbol{\sigma} \cdot \mathbf{A} + W_{PS} \\ -c\boldsymbol{\sigma} \cdot i\nabla - \boldsymbol{\sigma} \cdot \mathbf{A} + W_{PS} & -mc^2 + W_V + \mathbf{A}_P \cdot \boldsymbol{\sigma} - W_S - E \end{pmatrix} \begin{pmatrix} \psi_L \\ \psi_S \end{pmatrix} = 0 \quad (1.13)$$

where

- W_S - scalar potential
- W_V - vectorial potential
- W_{PS} - pseudoscalar potential
- \mathbf{A}_P - pseudo-vectorial potential

1.2 Computational methods for the non-spherically symmetric systems

1.2.1 The Gaussian basis set

The implementation of the projection of the Dirac Hamiltonian on a functional space can be achieved by using a Gaussian basis set. Gaussian functions are defined by a coefficient α and a center \mathbf{R}

$$g(\alpha, \mathbf{R}; \mathbf{r}) = \left(\frac{2\alpha}{\pi}\right)^{\frac{3}{4}} e^{-\alpha(\mathbf{r}-\mathbf{R})^2} \quad (1.14)$$

Non-normalized Gaussian functions are characterized by the following multiplication property

$$g(\alpha_1, \mathbf{R}_1; \mathbf{r}) g(\alpha_2, \mathbf{R}_2; \mathbf{r}) = g\left(\alpha_1 + \alpha_2, \frac{\alpha_1 \mathbf{R}_1 + \alpha_2 \mathbf{R}_2}{\alpha_1 + \alpha_2}; \mathbf{r}\right) e^{-\frac{\alpha_1 \alpha_2}{\alpha_1 + \alpha_2}(\mathbf{R}_1 - \mathbf{R}_2)^2} \quad (1.15)$$

which is again a Gaussian. Gaussian basis sets are not orthonormal, as Gaussian functions cannot be orthogonalized, while their normalization condition is

$$\langle g_1 | g_2 \rangle = \left(\frac{2\alpha_1}{\pi} \right)^{\frac{3}{4}} \left(\frac{2\alpha_2}{\pi} \right)^{\frac{3}{4}} \left(\frac{\pi}{\alpha_1 + \alpha_2} \right)^{\frac{3}{2}} e^{-\frac{\alpha_1 \alpha_2}{\alpha_1 + \alpha_2} (\mathbf{R}_1 - \mathbf{R}_2)} = \left(\frac{2\sqrt{\alpha_1 \alpha_2}}{\alpha_1 + \alpha_2} \right)^{\frac{3}{2}} e^{-\frac{\alpha_1 \alpha_2}{\alpha_1 + \alpha_2} (\mathbf{R}_1 - \mathbf{R}_2)}$$

This represents a very useful property particularly when dealing with poly-centric systems.

1.2.2 Mono-electronic integrals

Using Gaussian functions one can analytically calculate mono-electronic integrals, which for the Coulomb potential can be written as:

$$\begin{aligned} \int d\mathbf{r} g(\alpha, \mathbf{R}; \mathbf{r}) &= \left(\frac{\pi}{\alpha} \right)^{\frac{3}{2}} = \langle g \rangle \\ \int d\mathbf{r} \frac{1}{r} g(\alpha, \mathbf{R}; \mathbf{r}) &= \left(\frac{\pi}{\alpha} \right)^{\frac{3}{2}} \frac{\text{erf}(\sqrt{\alpha}R)}{R} = \left\langle g \frac{1}{r} \right\rangle \end{aligned} \quad (1.16)$$

The electron-electron interaction potential (or the nucleon-nucleon using a simplified approach) can be modeled by a Yukawa potential with exponential coefficient set equal to zero (while it can be set different from zero for the nucleon-nucleon case), and thus it is important to find the matrix elements of this interaction potential using Gaussian functions. Mono-electronic integrals for the Yukawa potential can be written as follows:

$$\begin{aligned} \int d\mathbf{r} \frac{e^{-\frac{r}{\xi}}}{r} g(\alpha, \mathbf{R}; \mathbf{r}) &= \left\langle g \frac{e^{-\frac{r}{\xi}}}{r} \right\rangle = 2\pi \int_0^\infty r^2 dr \left[e^{-\alpha(r^2 - 2rR + R^2)} - e^{-\alpha(r^2 + 2rR + R^2)} \right] \frac{e^{-\frac{r}{\xi}}}{r} \\ &= \frac{1}{2} \left(\frac{\pi}{\alpha} \right)^{\frac{3}{2}} \frac{\left[-\text{erfc} \left(\frac{1}{2\sqrt{\alpha}\xi} + \sqrt{\alpha}R \right) e^{\left(\frac{1}{4\alpha\xi^2} + \frac{R}{\xi} \right)} + \text{erfc} \left(\frac{1}{2\sqrt{\alpha}\xi} - \sqrt{\alpha}R \right) e^{\left(\frac{1}{4\alpha\xi^2} - \frac{R}{\xi} \right)} \right]}{R} \\ &= \frac{1}{2} \left(\frac{\pi}{\alpha} \right)^{\frac{3}{2}} \frac{\left[-\text{erfcx} \left(\frac{1}{2\sqrt{\alpha}\xi} + \sqrt{\alpha}R \right) + \text{erfcx} \left(\frac{1}{2\sqrt{\alpha}\xi} - \sqrt{\alpha}R \right) \right]}{R} e^{-\alpha R^2} \end{aligned} \quad (1.17)$$

where $\text{erfcx}(x) = \text{erfc}(x)e^{x^2}$ and

$$\operatorname{erfc}(x) = \frac{2}{\sqrt{\pi}} \int_x^{\infty} e^{-u^2} du \quad , \quad \operatorname{erfcx}(x) = \frac{2}{\sqrt{\pi}} \int_x^{\infty} e^{x^2-u^2} du$$

By Taylor expanding Equation (1.17) from $\operatorname{erfcx}(a+x)$ and observing that $\frac{d}{dx}\operatorname{erfcx}(a+x)e^{-x^2} = -\frac{2}{\sqrt{\pi}}e^{-x^2} + 2a\operatorname{erfcx}(a+x)e^{-x^2}$ and $\frac{d}{dx}\operatorname{erfcx}(a-x)e^{-x^2} = \frac{2}{\sqrt{\pi}}e^{-x^2} - 2a\operatorname{erfcx}(a-x)e^{-x^2}$, we obtain

$$\begin{aligned} \left\langle m \frac{e^{-\frac{r}{\zeta}}}{r} \right\rangle &= \frac{2\pi^{\frac{3}{2}}}{\alpha} \left[\frac{1}{\sqrt{\pi}} - a\operatorname{erfcx}(a) + \frac{1}{3} \left(-2a^3\operatorname{erfcx}(a) + \frac{2a^2-1}{\sqrt{\pi}} \right) x^2 + \right. \\ &\quad \left. + \frac{2}{15} \left(-4a^5\operatorname{erfcx}(a) + \frac{4a^4-2a^2+3}{\sqrt{\pi}} \right) + \dots \right] \end{aligned}$$

where $a = \frac{1}{2\sqrt{\alpha}\zeta}$ and $x = \sqrt{\alpha}R$.

1.2.3 Green's function matrix elements

The Green's function projected on Gaussian functions reads:

$$\left\langle s_1 \left| \frac{1}{p_0^2 + \nabla^2} \right| s_2 \right\rangle \tag{1.18}$$

where $p_0 \in \mathbb{C}$. The integral in Equation (1.18) can be more easily calculated in the Fourier space as the kinetic operator ∇^2 is diagonal:

$$\begin{aligned} \left\langle s_1 \left| \frac{1}{p_0^2 + \nabla^2} \right| s_2 \right\rangle &= \left(\frac{2\pi}{\sqrt{\alpha_1\alpha_2}} \right)^{\frac{3}{2}} \int d\mathbf{p} \frac{e^{-\frac{\alpha_1+\alpha_2}{4\alpha_1\alpha_2}p^2 + i\mathbf{p}\cdot(\mathbf{R}_1-\mathbf{R}_2)}}{p_0^2 - p^2} \\ &= \left(\frac{2\pi}{\sqrt{\alpha_1\alpha_2}} \right)^{\frac{3}{2}} 4\pi \int_0^{\infty} \frac{p^2 dp}{p|\mathbf{R}_1 - \mathbf{R}_2|} \frac{e^{-\frac{\alpha_1+\alpha_2}{4\alpha_1\alpha_2}p^2} \sin(p|\mathbf{R}_1 - \mathbf{R}_2|)}{p_0^2 - p^2} \\ &= \left(\frac{2\pi}{\sqrt{\alpha_1\alpha_2}} \right)^{\frac{3}{2}} 2\pi \int_{-\infty}^{\infty} \frac{p dp}{|\mathbf{R}_1 - \mathbf{R}_2|} \frac{e^{-\frac{\alpha_1+\alpha_2}{4\alpha_1\alpha_2}p^2 + ip|\mathbf{R}_1 - \mathbf{R}_2|}}{p_0^2 - p^2} \end{aligned}$$

These integrals can be reduced to integrals of the *erf* function in the complex space by considering that $w(z) = e^{-z^2} \operatorname{erfc}(-iz)$ and that

$$\int_{-\infty}^{\infty} \frac{e^{-t^2}}{z-t} dt = \begin{cases} -i\pi w(z) & \text{Im}z > 0 \\ -i\pi w(z) - 2e^{-z^2} & \text{Im}z < 0 \end{cases}$$

1.2.4 The two-step recurrence relation of $G_m(x)$

The Yukawa potential matrix element can be calculated for Gaussians of any order (s, p, d symmetry modified Gaussian functions) by a recurrence relation. To demonstrate that, we define the following quantities:

$$G_m(x) = \left(-\frac{1}{2x} \frac{d}{dx}\right)^m \left(\frac{\alpha}{\pi}\right)^{\frac{3}{2}} \left\langle m \frac{e^{-\frac{r}{\alpha}}}{r} \right\rangle = \left(-\frac{1}{2x} \frac{d}{dx}\right)^m \frac{\sqrt{\alpha} [-\text{erfcx}(a+x) + \text{erfcx}(a-x)] e^{-x^2}}{2x} \quad (1.19)$$

$$I_0(a, x) = [-\text{erfcx}(a+x) + \text{erfcx}(a-x)] e^{-x^2} \quad (1.20)$$

$$I_1(a, x) = [\text{erfcx}(a+x) + \text{erfcx}(a-x)] e^{-x^2} \quad (1.21)$$

Furthermore, we observe that $\frac{dI_0}{dx} = \frac{4}{\sqrt{\pi}} e^{-x^2} - 2aI_1$ and $\frac{dI_1}{dx} = -2aI_0$. The first element of the recurrence relation is

$$G_0(x) = \frac{\sqrt{\alpha} I_0(a, x)}{2x} \quad (1.22)$$

while the second one can be obtained by:

$$\begin{aligned} G_1(x) &= \left(\frac{1}{2x} \frac{d}{dx}\right) G_0(x) = \frac{\sqrt{\alpha}}{4x^2} \left\{ -\frac{4}{\sqrt{\pi}} e^{-x^2} + 2aI_1(a, x) + \frac{I_0(a, x)}{x} \right\} \\ &= \frac{1}{x^2} \left[\frac{1}{2} G_0(x) - \sqrt{\frac{\alpha}{\pi}} e^{-x^2} + \frac{\sqrt{\alpha}}{2} a I_1(a, x) \right] \end{aligned} \quad (1.23)$$

Moreover the third, fourth and fifth elements can be written as follows

$$\begin{aligned} G_2(x) &= \left(-\frac{1}{2x} \frac{d}{dx}\right) G_1(x) = \frac{1}{x^2} G_1(x) - \frac{\sqrt{\alpha}}{4x^2} \left\{ \frac{4}{\sqrt{\pi}} e^{-x^2} + 2a^2 \frac{I_0(a, x)}{x} - \frac{1}{2x} \frac{d}{dx} \frac{I_0(a, x)}{x} \right\} \\ &= \frac{3}{2x^2} G_1(x) - \frac{\sqrt{\alpha}}{\sqrt{\pi} x^2} e^{-x^2} + \frac{a^2}{x^2} G_0(x) = \frac{1}{x^2} \left[\frac{3}{2} G_1(x) - \sqrt{\frac{\alpha}{\pi}} e^{-x^2} + a^2 G_0(x) \right] \end{aligned} \quad (1.24)$$

$$G_3(x) = \frac{1}{x^2} \left[G_2(x) + \frac{3}{2}G_2(x) - \sqrt{\frac{\alpha}{\pi}}e^{-x^2} + a^2G_1(x) \right] = \frac{1}{x^2} \left[\frac{5}{2}G_2(x) - \sqrt{\frac{\alpha}{\pi}}e^{-x^2} + a^2G_1(x) \right] \quad (1.25)$$

$$G_4(x) = \frac{1}{x^2} \left[G_3(x) + \frac{5}{2}G_3(x) - \sqrt{\frac{\alpha}{\pi}}e^{-x^2} + a^2G_2(x) \right] = \frac{1}{x^2} \left[\frac{7}{2}G_3(x) - \sqrt{\frac{\alpha}{\pi}}e^{-x^2} + a^2G_2(x) \right] \quad (1.26)$$

Thus the recurrence relation can be generally written as:

$$G_{m+2}(x) = \frac{1}{x^2} \left[\left(m + \frac{3}{2} \right) G_{m+1}(x) - \sqrt{\frac{\alpha}{\pi}}e^{-x^2} + a^2G_m(x) \right] \quad (1.27)$$

1.2.5 Bi-electronic integrals

Bi-electronic integrals using Gaussian functions read:

$$\begin{aligned} \left\langle s_1 s_3 \left| \frac{e^{-\frac{|\mathbf{r}-\mathbf{r}'|}{\zeta}}}{|\mathbf{r}-\mathbf{r}'|} \right| s_2 s_4 \right\rangle &= \left(\frac{2\alpha_1}{\pi} \right)^{\frac{3}{4}} \left(\frac{2\alpha_2}{\pi} \right)^{\frac{3}{4}} \left(\frac{2\alpha_3}{\pi} \right)^{\frac{3}{4}} \left(\frac{2\alpha_4}{\pi} \right)^{\frac{3}{4}} \\ &\cdot \int d\mathbf{r} \int d\mathbf{r}' e^{-\alpha_1(\mathbf{r}-\mathbf{R}_1)^2} e^{-\alpha_2(\mathbf{r}-\mathbf{R}_2)^2} e^{-\alpha_3(\mathbf{r}'-\mathbf{R}_3)^2} e^{-\alpha_4(\mathbf{r}'-\mathbf{R}_4)^2} \\ &= \left[\frac{2(\alpha_1\alpha_2\alpha_3\alpha_4)^{\frac{1}{4}}}{\pi} \right]^3 e^{-\frac{\alpha_1\alpha_2}{\alpha_1+\alpha_2}(\mathbf{R}_1-\mathbf{R}_2)} e^{-\frac{\alpha_3\alpha_4}{\alpha_3+\alpha_4}(\mathbf{R}_3-\mathbf{R}_4)} \\ &\cdot \int d\mathbf{r} \int d\mathbf{r}' e^{-(\alpha_1+\alpha_2)(\mathbf{r}-\mathbf{P}_{12})^2} e^{-(\alpha_3+\alpha_4)(\mathbf{r}'-\mathbf{P}_{34})^2} \frac{e^{-\frac{|\mathbf{r}-\mathbf{r}'|}{\zeta}}}{|\mathbf{r}-\mathbf{r}'|} \end{aligned} \quad (1.28)$$

where $\mathbf{P}_{12} = \frac{\alpha_1\mathbf{R}_1+\alpha_2\mathbf{R}_2}{\alpha_1+\alpha_2}$ and $\mathbf{P}_{34} = \frac{\alpha_3\mathbf{R}_3+\alpha_4\mathbf{R}_4}{\alpha_3+\alpha_4}$. By defining $\mathbf{s} = \frac{\mathbf{r}+\mathbf{r}'}{2}$ and $\mathbf{q} = \mathbf{r} - \mathbf{r}'$ we obtain:

$$\begin{aligned} \int d\mathbf{r} \int d\mathbf{r}' e^{-(\alpha_1+\alpha_2)(\mathbf{r}-\mathbf{P}_{12})^2} e^{-(\alpha_3+\alpha_4)(\mathbf{r}'-\mathbf{P}_{34})^2} \frac{e^{-\frac{|\mathbf{r}-\mathbf{r}'|}{\zeta}}}{|\mathbf{r}-\mathbf{r}'|} \\ = \int d\mathbf{s} \int d\mathbf{q} e^{-(\alpha_1+\alpha_2)(\mathbf{s}+\frac{\mathbf{q}}{2}-\mathbf{P}_{12})^2} e^{-(\alpha_3+\alpha_4)(\mathbf{s}-\frac{\mathbf{q}}{2}-\mathbf{P}_{34})^2} \frac{e^{-\frac{q}{\zeta}}}{q} \\ = \left(\frac{\pi}{\alpha_1 + \alpha_2 + \alpha_3 + \alpha_4} \right)^{\frac{3}{2}} \int d\mathbf{q} e^{-\frac{(\alpha_1+\alpha_2)(\alpha_3+\alpha_4)}{\alpha_1+\alpha_2+\alpha_3+\alpha_4}[\mathbf{q}-(\mathbf{P}_{12}-\mathbf{P}_{34})]^2} \frac{e^{-\frac{q}{\zeta}}}{q} \end{aligned}$$

which can be reduced to an integral of the type reported in Equation (1.17).

Further details on the calculation of mono- and bi-electronic integrals using Gaussian functions of different orders (modified Gaussian functions) can be found in the reference [3].

1.3 Gaussian functions at work: application of the polycentric approach to the electronic structure calculation of molecules

To show the wide spectrum of applications that can be dealt with our relativistic approach, in this section we apply our method to investigate the electronic structure properties of several molecular systems of interest in astrophysics and atmospheric science.

In particular, we start our analysis by studying the bromotrifluoromethane (CF_3Br) molecule. This molecule is of paramount importance in environmental and climate sciences. Indeed, to protect the stratospheric ozone layer the Montreal Protocol banned ozone-depleting substances, such as chlorofluorocarbons (CFCs) as well as CF_3Br , present in the atmosphere due to their use in making foams for furniture and buildings, in aerosols and as refrigerants. The presence of these contaminants in our atmosphere declined steadily until 2013, when a sharp and mysterious rise in emissions of a key ozone-destroying chemicals has been detected by scientists, despite its production being banned around the world [4]. Ozone layer protects life on Earth from damaging UV radiation, and thus these chemicals are potentially harmful for mankind. Among the ozone-destroying molecules, responsible for both ozone depletion and global warming, CF_3Br (commercially known as Halon 1301, Freon 13B1) is potentially particularly harmful, due its long photo-dissociation time (65 years) under UV irradiation. This molecule can diffuse into our stratosphere, where enters the catalytic cycle of ozone depletion. Moreover, it displays a great capacity to absorb light between 8-12 μm , actively participating to climate change. Furthermore, due to its unique chemical-physical properties CF_3Br has been used as agent in fire extinguisher.

The atomic positions in CF_3Br have been optimized using Density Functional Theory (DFT), by means of VASP program suite [5, 6, 7, 8]. To find the equilibrium structure of CF_3Br we used a PBE-PAW pseudo-potential [9, 10] with a plane-wave cut-off equal to 400 eV to deal with the ion- valence electron interaction, a Gaussian smearing of the partial occupancies with a width of $\sigma = 0.05$ eV, using only the Γ point and an orthorhombic calculation supercell with dimensions equal to $20 \times 10 \times 10$. The equilibrium structure of CF_3Br is represented in the right hand side of Fig. (1.1). CF_3Br presents a tetrahedral molecular geometry, having Br to C equilibrium bond distance equal to 1.95 Å, while C-F is equal to 1.34 Å.

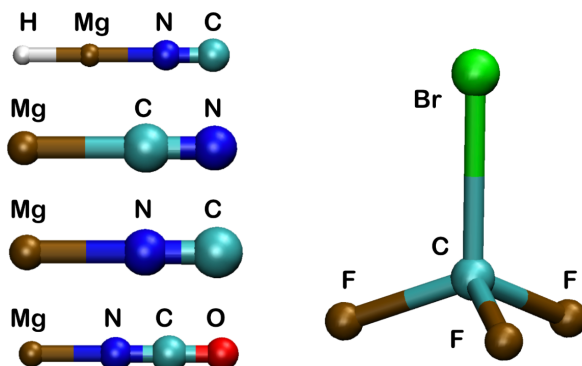


FIGURE 1.1: Optimized molecular structures of bromotrifluoromethane (CF_3Br , right), HydroMagnesium isocyanide (HMgNC), magnesium isocyanide isomers (MgCN and MgNC), and magnesium fulminate radical (MgNCO)

The same parameters have been used for optimizing the atomic structure of the other molecular systems under investigation, such as magnesium-bearing ($[\text{H},\text{Mg},\text{C},\text{N},\text{O}]$) compounds, whose atomic structures at equilibrium are reported in the left hand side of Figure (1.1). We find that all the equilibrium structures of these compounds are linear and we report the equilibrium bond distances in Table (1.1).

Magnesium has a cosmic abundance comparable to Si and Fe, and thus is one of the most abundant metals in space.

Furthermore, magnesium-bearing molecules in space, such as magnesium isocyanide isomers, MgCN and MgNC [11], and hydro-magnesium isocyanide, HMgNC [12, 13], are all relevant astrochemical molecules. MgCN isomers were identified by radioastronomers in the circumstellar envelope of the IRC+10216 star in 1995 and also observed in protoplanetary nebulae. More recently, in 2013, the discovery of hydromagnesium isocyanide, HMgNC , in the carbon-rich evolved star IRC +10216 was reported after laboratory characterization. In this regard, it is important to study the stability and the electronic structure of $[\text{Mg},\text{C},\text{N},\text{O}]$ compounds, such as MgNCO [14], as plausible astronomical molecules. Indeed, this investigation could help their laboratory or astronomical detection.

To calculate the relative stability of isomers we used our relativistic approach based on the projection onto a functional space spanned by Gaussian functions (see

TABLE 1.1: Equilibrium bond distances in Å for the compounds reported in the first column

	<i>H-Mg</i>	<i>Mg-N</i>	<i>N-C</i>	<i>C-O</i>	<i>Mg-C</i>	<i>C-N</i>
HMgNC	1.69484	1.92995	1.18833	-	-	-
MgNCO	-	1.90087	1.21114	1.19227	-	-
MgCN	-	-	-	-	2.08919	1.1745
MgNC	-	1.95322	1.18828	-	-	-

section 1.2). In particular aug-cc-PVTZ Gaussian basis sets were used to reach good accuracy.

TABLE 1.2: Total energies calculated at mean-field level of theory for the molecules reported in the first column. Second and third column report the non relativistic values obtained by using aug-cc-PVTZ contracted and uncontracted basis set. Last column reports the relativistic values of the total energy for the aug-cc-PVTZ uncontracted basis set

	Total Energy [eV]		
	<i>Contracted Non Relativistic</i>	<i>Uncontracted Non Relativistic</i>	<i>Uncontracted Relativistic</i>
CBrF ₃	-	-2908.5838	-2928.3396
HMgNC	-292.5525	-292.5530	-292.5601
MgNCO	-349.3263	-349.4938	-349.4274
MgCN	-291.8744	-291.8864	-291.8945
MgNC	-291.8981	-291.8986	-291.9064

In Table (1.2) we report the Hartree-Fock (second and third columns) and the DHF (last column) relative energies of all species corresponding to true minima on the [Mg,C,N,O] compounds after the structural minimization. We notice that in our relativistic simulations the most stable isomer is MgNC (last row of Table (1.2)), being MgCN located higher in energy of 0.324 eV, suggesting a slower rate for the isomerization reaction.

We remind that in order to reach better accuracy on the total energy we need to include in the basis set both ψ and $V\psi$ to make sure that the projected potential approach contains the eigenvalues corresponding to the true potential. We found out empirically that this goal can be more effectively accomplished if the basis set is made by uncontracted Gaussian functions. Thus, in Table (1.2) we report the results of our calculations using both contracted and uncontracted basis set as well as the non-relativistic calculations for the same molecules. We notice that moving

from non-relativistic contracted to non-relativistic uncontracted and finally to uncontracted relativistic simulations the total energy decreases.

1.4 Conclusions

This chapter was focused on the development of a theoretical and computational method for the solution of the Dirac–Hartree–Fock equations of a general system of interacting fermions. In particular, this approach makes use of Gaussian basis sets and is able to treat multicentric systems, such as molecules. In this regard, we discussed several applications of our method to molecular systems of interest in astrophysical scenarios, such as the MgCN isomers, and in environmental science, such as the CF₃Br molecule. Only a few results were reported in this thesis, as our model was used mainly to study beta-decay spectra in heavy atomic systems; nevertheless, we decided to discuss it here as this method is very general and can be useful for developing tailored electronic structure code.

Bibliography

- [1] T. Morresi, S. Taioli, S. Simonucci, Nuclear beta decay: Relativistic theory and ab initio simulations of electroweak decay spectra in medium-heavy nuclei and of atomic and molecular electronic structure (adv. theory simul. 11/2018), *Advanced Theory and Simulations* 1 (11) (2018) 1870030. arXiv:<https://onlinelibrary.wiley.com/doi/pdf/10.1002/adts.201870030>, doi:10.1002/adts.201870030.
URL <https://onlinelibrary.wiley.com/doi/abs/10.1002/adts.201870030>
- [2] M. Rehher, A. Wolf, *Relativistic Quantum Chemistry: The Fundamental Theory of Molecular Science*, Wiley-VCH Verlag GmbH & Co. KGaA, 2009. doi:10.1002/9783527627486.
- [3] G. A., M. J., Modified gaussian functions and their use in quantum chemistry. i. integrals, *International Journal of Quantum Chemistry* 7 (3) 623–634. arXiv:<https://onlinelibrary.wiley.com/doi/pdf/10.1002/qua.560070315>, doi:10.1002/qua.560070315.
URL <https://onlinelibrary.wiley.com/doi/abs/10.1002/qua.560070315>
- [4] S. A. Montzka, G. S. Dutton, P. Yu, E. Ray, R. W. Portmann, J. S. Daniel, L. Kuipers, B. D. Hall, D. Mondeel, C. Siso, J. D. Nance, M. Rigby, A. J. Manning, L. Hu, F. Moore, B. R. Miller, J. W. Elkins, An unexpected and persistent increase in global emissions of ozone-depleting cfc-11, *Nature* 557 (2018) 413.

- [5] G. Kresse, J. Hafner, Ab initio molecular dynamics for liquid metals, *Phys. Rev. B* 47 (1993) 558–561. doi:10.1103/PhysRevB.47.558.
URL <https://link.aps.org/doi/10.1103/PhysRevB.47.558>
- [6] G. Kresse, J. Furthmüller, Efficiency of ab-initio total energy calculations for metals and semiconductors using a plane-wave basis set, *Computational Materials Science* 6 (1) (1996) 15–50. doi:[https://doi.org/10.1016/0927-0256\(96\)00008-0](https://doi.org/10.1016/0927-0256(96)00008-0).
URL <http://www.sciencedirect.com/science/article/pii/S0927025696000080>
- [7] G. Kresse, J. Hafner, Ab initio molecular-dynamics simulation of the liquid-metal–amorphous-semiconductor transition in germanium, *Phys. Rev. B* 49 (1994) 14251–14269. doi:10.1103/PhysRevB.49.14251.
URL <https://link.aps.org/doi/10.1103/PhysRevB.49.14251>
- [8] G. Kresse, J. Furthmüller, Efficient iterative schemes for ab initio total-energy calculations using a plane-wave basis set, *Phys. Rev. B* 54 (1996) 11169–11186. doi:10.1103/PhysRevB.54.11169.
URL <https://link.aps.org/doi/10.1103/PhysRevB.54.11169>
- [9] P. E. Blöchl, Projector augmented-wave method, *Phys. Rev. B* 50 (1994) 17953–17979. doi:10.1103/PhysRevB.50.17953.
URL <https://link.aps.org/doi/10.1103/PhysRevB.50.17953>
- [10] G. Kresse, D. Joubert, From ultrasoft pseudopotentials to the projector augmented-wave method, *Phys. Rev. B* 59 (1999) 1758–1775. doi:10.1103/PhysRevB.59.1758.
URL <https://link.aps.org/doi/10.1103/PhysRevB.59.1758>
- [11] M. Anderson, L. Ziurys, The millimeter-wave spectrum of 25mgnc and 26mgnc: bonding in magnesium isocyanides, *Chemical Physics Letters* 231 (2) (1994) 164–170. doi:[https://doi.org/10.1016/0009-2614\(94\)01259-8](https://doi.org/10.1016/0009-2614(94)01259-8).
URL <http://www.sciencedirect.com/science/article/pii/S0009261494012598>
- [12] M. Gronowski, R. Kolos, Ab initio studies of the structure and spectroscopy of chnmg stoichiometry molecules and van der waals complexes, *The Journal of Physical Chemistry A* 117 (21) (2013) 4455–4461, PMID: 23639064. arXiv:<https://doi.org/10.1021/jp312861s>, doi:10.1021/jp312861s.
URL <https://doi.org/10.1021/jp312861s>
- [13] C. Cabezas, J. Cernicharo, J. L. Alonso, M. Agundez, S. Mata, M. Guelin, I. Pena, Laboratory and astronomical discovery of hydromagnesium isocyanide, *The Astrophysical Journal* 775 (2) (2013) 133.
URL <http://stacks.iop.org/0004-637X/775/i=2/a=133>

- [14] A. Vega-Vega, A. Largo, P. Redondo, C. Barrientos, Structure and spectroscopic properties of [mg,c,n,o] isomers: Plausible astronomical molecules, ACS Earth and Space Chemistry 1 (3) (2017) 158. arXiv:<https://doi.org/10.1021/acsearthspacechem.7b00019>, doi:10.1021/acsearthspacechem.7b00019. URL <https://doi.org/10.1021/acsearthspacechem.7b00019>

Chapter 2

Ab-initio simulations of dielectric functions and reflection electron energy loss spectra of diamond and graphite

Moving up the “dimensional ladder”, in this chapter we study periodic systems with a unit cell containing a relatively small number of electrons. Periodicity enables one to use the Bloch’s theorem [1] to build the wavefunctions of the bound electrons. A common framework in periodic simulations of condensed matter systems is Density Functional Theory (DFT) in connection with plane-wave basis sets, which are complete and orthonormal basis sets. At variance with the localised functions, such as the position-dependent Gaussians that we used in the previous chapter 1 for dealing with molecular systems, plane waves treat the space on the same foot, be it filled with matter or empty. The next two chapters will use several plane-wave DFT code suites to solve the electronic structure problem. In this chapter, in particular, the ELK code was used [2], which is an all-electron full-potential linearised augmented-plane wave (LAPW) program [3]. The LAPW approach takes into account also the core-shell electrons in the self-consistent iterations. This approach is thus different from the pseudopotential method, where the core-electron screening is not computed explicitly on-the-fly, rather it is added to the nuclear potential in tabulated external files. Of course pseudopotential approaches are computationally faster and less memory-intensive than LAPW methods, nevertheless the latter have the advantage to be more transferable and, in principle, more accurate [3]. Before presenting the work on diamond and graphite, we will give a brief review of the philosophy behind DFT, which will be useful also in the next chapters.

2.1 Density Functional Theory in a nutshell

Density Functional Theory became the state-of-the-art method in condensed matter physics calculations when, in 1964, Hohenberg and Kohn enunciated two fundamental theorems [4], stating that: i) *there is a one-to-one correspondence between the ground-state density $\rho(\mathbf{r})$ of a many-electron system (atom, molecule, solid) and the external potential V_{ext}* , ii) *$E[\rho]$ reaches its minimal value (equal to the ground-state total energy) for the ground-state density corresponding to V_{ext}* . Indeed these powerful theorems enable one to express the ground state energy as a functional of the electron density, which depends on three degrees of freedom, instead of the wavefunctions which carries much more information. In this way an exact framework was set to the many-body electronic structure problem. Furthermore, in order to have a practical exploitation of these fundamental theoretical concepts, in a follow-up work Kohn and Sham delivered a recipe to obtain the ground state electronic density [5] as the sum of the square of single-particle wavefunctions of a 'fictitious' system. In this thesis we use this DFT formulation: here we sketch a short derivation (taken mostly from [6]) of the self-consistent equations that one needs to solve to obtain the ground state properties of our many-body systems.

For a fixed ionic configuration, the Hamiltonian for N electrons reads:

$$\hat{H} = -\frac{\hbar^2}{2} \sum_{i=1}^N \nabla_{\mathbf{r}_i}^2 + \frac{1}{2} \sum_{i \neq j} \frac{e^2}{|\mathbf{r}_i - \mathbf{r}_j|} + \sum_i v_{ext}(\mathbf{r}_i) = \hat{T} + \hat{V}_{ee} + \hat{V}_{ext} \quad (2.1)$$

The ground state energy E_{gs} can be found by minimizing $\langle \Psi | \hat{H} | \Psi \rangle$ under the constraint $\langle \Psi | \Psi \rangle = 1$. However such minimization over the possible $\Psi(\{\mathbf{r}\}) = \Psi(\mathbf{r}_1, \mathbf{r}_2, \dots, \mathbf{r}_N)$ can be practically done only when N is small enough. The idea of Hohenberg and Kohn was to express E_{gs} in terms of the density, which is defined as

$$n(\mathbf{r}) = N \int d\mathbf{r}_2 \dots d\mathbf{r}_N \Psi^*(\mathbf{r}, \mathbf{r}_2, \dots, \mathbf{r}_N) \Psi(\mathbf{r}, \mathbf{r}_2, \dots, \mathbf{r}_N) \quad (2.2)$$

In particular, they introduced the energy functional

$$E_{HK}[n] = F[n] + \int d\mathbf{r} n(\mathbf{r}) v_{ext}(\mathbf{r}) \quad (2.3)$$

where $F[n] = \min_{\Psi \rightarrow n} \langle \Psi | \hat{T} + \hat{V}_{ee} | \Psi \rangle$ is a universal and unique functional of the density and where the energy functional E_{HK} obeys a variational principle $E_{HK} \geq E_{gs}$. In the paper [5], the two authors proposed an approximation for the functional $F[n]$ that maps the problem of a system of interacting particles onto a system of independent electrons with the same density $n(\mathbf{r})$. This permits to express the energy $E = \langle \Psi | \hat{H} | \Psi \rangle$ as

$$E[n] = T_s[n] + E_H[n] + E_{xc}[n] + E_{ext}[n] \quad (2.4)$$

with

$$E_{xc} = \langle \Psi | \hat{T} | \Psi \rangle - T_s[n] + \langle \Psi | \hat{V}_{ee} | \Psi \rangle - E_H[n] \quad (2.5)$$

In this section we refer to Ψ as the wavefunction of the true many-body system while to $\{\phi_n\}$ for the set of independent particle wavefunctions of the Kohn-Sham 'fictitious' system. The functional $T_s[n]$ is the kinetic energy of the fictitious single-particle system for which the density is

$$n(\mathbf{r}) = 2 \sum_{i_{occ}} |\phi_i(\mathbf{r})|^2 \quad (2.6)$$

By introducing the Hartree potential

$$v_H[n](\mathbf{r}) = \int d\mathbf{r}' \frac{n(\mathbf{r}')}{|\mathbf{r} - \mathbf{r}'|} \quad (2.7)$$

and the unknown $\mu_{xc}[n](\mathbf{r})$ energy density per particle, one can rewrite the energy as

$$E[n] = T_s[n] + \int d\mathbf{r} n(\mathbf{r}) \left[\frac{1}{2} v_H[n](\mathbf{r}) + \mu_{xc}(\mathbf{r}) + v_{ext}(\mathbf{r}) \right] = T_s[n] + \int d\mathbf{r} n(\mathbf{r}) v_{KS}[n](\mathbf{r}) \quad (2.8)$$

The ground state energy E_{gs} can be found by minimizing Eq. (2.8) with respect to the density $n(\mathbf{r})$ or solving the Kohn Sham equations

$$\left(-\frac{\hbar^2}{2} \nabla^2 + v_H[n](\mathbf{r}) + v_{xc}[n](\mathbf{r}) + v_{ext}(\mathbf{r}) \right) \phi_n = \epsilon_n \phi_n \quad (2.9)$$

where the exchange-correlation potential $v_{xc}[n](\mathbf{r})$ is defined as $v_{xc}[n](\mathbf{r}) = \frac{\delta E_{xc}[n]}{\delta n(\mathbf{r})}$. These equations (2.9) must be solved self-consistently because the potentials depend on the density and thus on the wavefunctions themselves. We notice that by following this derivation all the unknown physics is hidden in the exchange and correlation term.

Thus within the formalism of the Kohn-Sham DFT, the ground state energy E_{gs} and ground state density (2.6) can be calculated by solving a set of single particle Schrödinger equations. However, the exchange-correlation potential $v_{xc}[n]$ in eq. (2.9) is unknown and it is only at this point that some approximations must be introduced to model the interaction between electrons. In [5], Kohn and Sham model the exchange-correlation energy of their system using the exchange-correlation energy density of a homogeneous electron gas, which is called Local Density Approximation (LDA). After the revolutionary paper [5], a lot of exchange-correlation functionals were introduced trying to improve the LDA approximation, the most popular being the Generalized Gradient Approximation (GGA) and in particular within this class the Perdew-Burke-Ernzerhof (PBE) one [7]. A library of the implemented and free-to-use functionals can be found at [8].

2.2 Aim of the work

Naturally occurring allotropic forms of carbon, such as diamond, multi-layer graphene, and graphite, along with its intercalation compounds, could be used as viable candidates for an all-carbon electronics revolution. In particular, diamond was long considered an ideal candidate for enhancing the performances of electronic devices due to its high thermal conductivity and charge mobility, wide band gap, optical isotropic structure and robustness owing to its strong covalent sp^3 -hybridized structure. On the other hand, graphite is the most stable carbon allotrope, arranged in the form of a layered solid, showing both strong two-dimensional sp^2 -hybridized lattice bonds, similar in strength to those found in diamond, and weak interplanar bonds that make it soft and malleable as well as anisotropic to external perturbations. Furthermore, graphite shows optimal heat and electrical conductivity retaining the highest natural strength and stiffness even at temperatures in excess of 3000 °C.

In this respect, the work presented in this chapter is aimed at modelling the electron-transport properties of diamond and graphite films by calculating a number of observables of paramount importance for designing novel optical and electronic devices, such as inelastic mean free path, stopping power, plasmons and secondary electron spectra. The specific goal of our analysis is to unravel the impact that different theoretical approaches for calculating the dielectric function, ranging from ab initio calculations to the use of a parametrized models, such as Drude–Lorentz (DL), may have on the assessment of the dielectric response of these two materials by comparing our simulations with experimental reflection electron energy-loss spectra (REELS). This study represents thus a step towards a better understanding of the basic properties characterizing both bulk and thin-film carbon materials as well as an important contribution towards the development of an all-carbon electronics.

We notice that all the observables considered in our analysis are based on the accurate assessment of the frequency-dependent dielectric function, which links microscopic properties, such as the band structure of solids, to macroscopic features that are the direct outcome of spectroscopic experiments, such as the absorption coefficient, the surface impedance or the electron energy loss.

To compute the dielectric function dependence on the transferred momentum we proceed along three different routes: i) first, we use a semi-classical approach, whereby one assumes the knowledge of the long-wavelength or optical limit of the dielectric function ($q \rightarrow 0$ limit); this information is usually provided by experimental measurements of optical absorption [9], transmission electron energy-loss experiments [10, 11] or ab initio simulations [12]. To go beyond the optical limit, we extend the dielectric response to finite momenta by using a DL model. In this approach, the dielectric function is approximated by a number of damped harmonic oscillators with frequencies equal to the plasmon frequencies obtained by fitting experimental data [13, 14] and a friction-type force to simulate general dissipative processes; ii) second approach uses ab initio simulations to calculate the dielectric response for vanishing

momentum transfer, eventually extended to finite momenta by a DL model; iii) third, we find the dispersion law of the dielectric function at finite momentum q , taken along some specific symmetry directions, by using a full ab initio (AI) approach, based on time-dependent density functional simulations [15] in the linear response (LR-TDDFT) [16].

The combination of ab initio calculations with electron-gas models for calculating physical observables such as the inelastic mean free path, has been previously studied also by Nguyen-Truong [17], Chantler *et al.* [18] and Sorini *et al.* [19]. In particular, the extension of the dielectric response at finite momenta with the Drude–Lorentz approach turned out to be the most accurate semi-empirical model available, as reported by Garcia-Molina *et al.* [20].

The so-derived dielectric functions are used as input for a Monte Carlo description of the inelastic scattering probability to calculate the energy loss of electrons along their path within the solid. The comparison between our simulated and recorded REELS allows us to assess the impact that external tuneable parameters and semi-classical assumptions might have on the accuracy of simulated spectral lineshapes.

Furthermore, we develop a new model for taking into account the anisotropy of graphite, in which the ab initio calculation of the dielectric function in the optical limit ($\epsilon(q \rightarrow 0, W)$) is performed also along the direction orthogonal to the plane (identified by the \mathbf{c} directional vector), which accounts for inter-planar interactions. In this case we obtain two different ELFs, one along and the other perpendicular to \mathbf{c} , which represents the direction perpendicular to the graphite planes. Then, after fitting these two dielectric functions in the optical limit by using DL functions, we combine them via an “anisotropy parameter” tuned to obtain the best agreement with in-house recorded REELS experimental data. Finally, we extend the fitted dielectric functions to finite momenta by a quadratic dispersion law. In this way, the energy losses in planar and inter-planar directions were both taken into account in our Monte Carlo simulations.

2.3 Experimental details

Here we report some details about the experiments recorded in our laboratories which were used to test numerical simulations.

A polycrystalline diamond film was deposited on a silicon substrate in a microwave tubular reactor using a $\text{CH}_4\text{-H}_2$ gas mixture. After exposure to atmospheric pressure, the film was inserted into an Ultra High Vacuum (UHV) system equipped with both a sample preparation and an analysis chamber. Highly Oriented Pyrolytic Graphite (HOPG) was cleaved ex-situ before inserting into the UHV system. The two samples

were cleaned by annealing at 600 °C for 10 minutes in UHV. REEL spectra were acquired in a PHI 545 system operating at a base pressure of $\approx 2 \times 10^{-10}$ mbar. The instrument is equipped with a double-pass cylindrical mirror analyzer (CMA), a coaxial electron gun, a non-monochromatic MgK α ($h\nu = 1253.6$ eV) X-ray source and a He discharge lamp. In CMA, incoming electrons cross the surface at a fixed angle with respect to the sample normal, while outgoing electrons cross the surface at a variable angle dependent on the angle between the surface normal and the CMA axis (30°), the entrance angle to the analyser ($42^\circ \pm 6^\circ$) and the azimuth angle in a plane normal to the CMA axis. Spectra are taken at a constant energy resolution of 0.6 eV, as measured on a Pd Fermi edge. The measured FWHM of the zero-loss peak (ZLP) is 0.9 eV. The energy of incident electrons ranges from $T = 250$ eV to $T = 2000$ eV. Once acquired, REEL spectra are corrected for the energy dependence ($E^{-0.9}$) of the analyser transmission function.

2.4 Computational details

2.4.1 Computed observables for charge transport simulations

The physical quantity relating the microscopic and macroscopic description of the electron-beam interaction with matter is given by the dielectric response function. It is important to distinguish between microscopic and macroscopic quantities, where the latter are defined as averages over the unit cell of the former. In fact, the total electric field induced by an external perturbing field can exhibit rapid oscillations at the atomic level, while at larger scale the response function is homogeneous. For periodic crystals (as we model diamond and graphite films periodic in the in-plane direction), one can exploit the translational symmetry and the microscopic dielectric function can be conveniently written in reciprocal space, i.e. $\epsilon_{\mathbf{G},\mathbf{G}'}(\mathbf{q}, W) = \epsilon(\mathbf{q} + \mathbf{G}, \mathbf{q} + \mathbf{G}', W)$, where \mathbf{G} and \mathbf{G}' are reciprocal lattice vectors, \mathbf{q} is the transferred momentum contained in the first Brillouin zone (IBZ) and W is the transferred energy. Using this notation $\epsilon_{\mathbf{G},\mathbf{G}'}(\mathbf{q}, W)$ is also often called dielectric matrix. It can be shown [16] that the relation between the experimentally measurable macroscopic dielectric function and the microscopic one is [21, 22]:

$$\epsilon(\mathbf{q}, W) = \left[\epsilon_{\mathbf{G}=0, \mathbf{G}'=0}^{-1}(\mathbf{q}, W) \right]^{-1} \quad (2.10)$$

In particular, electron transport observables, such as the energy loss per unit path or the inelastic scattering cross section, are proportional to the imaginary part of minus the inverse of the dielectric function [23], which is called energy loss function (ELF):

$$\text{ELF} = \text{Im} \left[-\frac{1}{\epsilon(\mathbf{q}, W)} \right] \quad (2.11)$$

In general, the momentum transferred by electrons upon collisions is neither negligible nor constant in different energy ranges. Thus one needs to evaluate the dielectric function also out of the optical limit before calculating the expression in Eq. (2.11). In this regard, the computation of the dielectric response for finite momentum transfer is a major issue in the treatment of inelastic interactions, and has a dramatic influence on energy-loss spectra and secondary-electron lineshapes. In the following sections we describe two different approaches at different levels of accuracy to overcome this issue, notably the DL and the full AI models.

We stress that the assumption behind the validity of Eq. (2.11) is the first order Born approximation, which is reliable only for sufficiently fast charged particles that can thus be considered point-like and weakly deflected in each collision by the potential scattering. In general, the latter hypothesis means that the incident particle kinetic energy T should exceed the energy of the target electrons. In our case, this request means that $T(\text{eV}) \gg 13.6Z^2 \simeq 490 \text{ eV}$. However, calculations performed using Eq. (2.11) can be considered reliable well below the above mentioned limit [24]. Indeed, the latter value is referred to core-level electrons, while in our case only target valence electrons, having much lower kinetic energy, enter the model.

2.4.2 Drude–Lorentz model

The DL model approximates the material dielectric response to an applied uniform external field of frequency $\omega = \frac{W}{\hbar}$, with W the perturbation energy and \hbar the reduced Planck constant, by considering the target screening electrons as harmonic oscillators of frequency equal to the plasmon frequency $\omega_n = \frac{E_n}{\hbar}$, with E_n the plasmon energy. Charge oscillation is damped via a damping constant Γ_n , that takes into account friction-like forces affecting the oscillatory harmonic motion. Furthermore, within this approach the ELF is extrapolated outside the optical domain, for not-vanishing momentum, by using a quadratic dispersion law that resembles the Random Phase Approximation (RPA) [24, 20, 25]. In the RPA, valence electrons in the solid are approximated by a non-interacting homogeneous gas, and the plasmon energy is expanded to second order in q as:

$$E_n(q \neq 0) = E_n(q = 0) + \frac{\hbar^2 q^2}{2m} \quad (2.12)$$

The ELF can thus be expressed as a sum over all oscillators of q -dependent generalized DL functions with a full-width-half-maximum Γ_n as follows [26, 27, 24]:

$$\text{Im} \left[-\frac{1}{\epsilon(q, W)} \right] = \sum_n \frac{A_n \Gamma_n W}{(E_n^2(q) - W^2)^2 - (\Gamma_n W)^2} \quad (2.13)$$

where A_n is the oscillator strength of the n^{th} -oscillator and can be obtained by fitting procedures of optical data. Most importantly, it can be shown that the f -sum rule is exactly satisfied by the Drude dielectric function.

2.4.3 Ab initio simulations

Ab initio simulations of diamond and graphite dielectric functions have been carried out using a TDDFT approach in the linear-response (LR) approximation [28]. TDDFT has shown great potential to replace computationally expensive many-body perturbation methods for accessing excitation energies and spectra of solids in their interaction with electromagnetic fields. The key quantity to perform LR-TDDFT simulation is the polarization function $\chi(\mathbf{r}, t, \mathbf{r}', t')$ describing the change of the density δn at (\mathbf{r}, t) due to a small deviation in the external perturbation δv_{ext} at (\mathbf{r}', t') :

$$\delta n(\mathbf{r}, t) = \int dt' \int d^3r' \chi(\mathbf{r}, t, \mathbf{r}', t') \delta v_{\text{ext}}(\mathbf{r}', t') \quad (2.14)$$

The TDDFT many-body response function $\chi(\mathbf{r}, t, \mathbf{r}', t')$ is related to the independent-particle polarizability $\chi_{KS}(\mathbf{r}, t, \mathbf{x}, \tau)$ by a Dyson-type equation as follows:

$$\chi(\mathbf{r}, t, \mathbf{r}', t') = \chi_{KS}(\mathbf{r}, t, \mathbf{r}', t') \left\{ \int d\tau \int d^3x \int d\tau' \int d^3x' \chi_{KS}(\mathbf{r}, t, \mathbf{x}, \tau) \left[\frac{\delta(\tau - \tau')}{|\mathbf{x} - \mathbf{x}'|} + f_{xc}(\mathbf{x}, \tau, \mathbf{x}', \tau') \right] \chi(\mathbf{x}', \tau', \mathbf{r}', t') \right\} \quad (2.15)$$

where $f_{xc}(\mathbf{r}, t, \mathbf{r}', t') = \left. \frac{\delta v_{xc}(\mathbf{r}, t)}{\delta n(\mathbf{r}', t')} \right|_{n_{\text{gs}}(\mathbf{r}, t)}$ is the energy-dependent exchange-correlation kernel. The independent-particle response function χ_{KS} is calculated usually via a mean-field approach, such as Kohn–Sham DFT. As in static DFT, the time-dependent exchange-correlation potential is an unknown density functional and calculations usually rely on the so-called adiabatic local-density approximation (ALDA) in which the time-dependence of the functional is neglected [15]. However, in systems where excitonic effects are expected to have a strong influence on spectral features due to an ineffective electronic screening, e.g. in insulators such as diamond, the use of a bootstrap kernel [29] that includes effects beyond the RPA is necessary.

Assuming translational invariance, the ELF can be computed inserting Eq. (2.10) into Eq. (2.11). The inversion procedure can be cumbersome for large basis sets and large k-point grids. Thus, one can calculate the so-called dielectric matrix without local-field effects (LFE), in which the dielectric matrix off-diagonal elements ($\epsilon_{\mathbf{G}, \mathbf{G}'}(\mathbf{q}, W)$, $\mathbf{G}, \mathbf{G}' \neq 0$) for different values of \mathbf{q} are neglected [22]. In the latter case, the macroscopic dielectric matrix is obtained by simply inverting the head of the microscopic dielectric matrix. However, in these off-diagonal terms the fluctuations on atomic scale of the polarization are encoded. For highly inhomogeneous electron density systems or highly locally polarizable atoms, such as in the case of diamond and graphite, LFE can play a significant role in the description of the dielectric properties [30], particularly at small wavelengths, to the point of invalidating even qualitative results. Thus, in our analysis we include LFE in the dielectric properties of

these carbon-based materials, where strong microscopic local fields can be created. Including LFE, one can show that the dielectric function in reciprocal space is [31]:

$$\epsilon_{\mathbf{G},\mathbf{G}'}^{-1}(\mathbf{q}, W) = \delta_{\mathbf{G},\mathbf{G}'} + v_{\mathbf{G},\mathbf{G}'}^s(\mathbf{q})\chi_{\mathbf{G},\mathbf{G}'}(\mathbf{q}, W) \quad (2.16)$$

where $v_{\mathbf{G},\mathbf{G}'}^s(\mathbf{q}) = \frac{4\pi e^2}{|\mathbf{q}+\mathbf{G}||\mathbf{q}+\mathbf{G}'|}$ is the Fourier transform of the Coulomb potential, and $\chi_{\mathbf{G},\mathbf{G}'}(\mathbf{q}, W)$ is the microscopic polarizability.

The computation of the dielectric and energy-loss functions within the TDDFT framework has been carried out by using the ELK code, which is an all-electron full-potential linearised augmented-plane-wave (FP-LAPW) program [2]. More specifically, the electron-electron interaction in diamond crystals was described via the generalized gradient approximation (GGA) [32] using a “bootstrap” exchange-correlation kernel f_{xc} [29], with the cut-off for the augmented plane waves set to 665 eV. Brillouin zone sampling was performed using a $20 \times 20 \times 20$ k -point grid along with an electron occupancy Fermi smearing of 0.2 eV, which ensures convergence of the dielectric observables for the primary cell below chemical accuracy.

In the case of graphite, a local spin-density approximation (LSDA) [33] to the exchange-correlation functional has been used together with an ALDA for the exchange-correlation kernel f_{xc} . The Brillouin zone was sampled using a $16 \times 16 \times 16$ k -point grid, while the other DFT parameters were kept the same as for diamond. This k -point grid is sufficiently fine to obtain a converged ELF (a finer k -point mesh is instead needed to converge the dielectric function). Indeed, calculations performed with a significantly higher number of k -points ($24 \times 24 \times 20$) showed some negligible deviations of the ELF, particularly below 30 eV, with a small increased or decreased peak height. However, we remind that the ELF appears as an integrand in the calculation of the observables used in our MC simulations (that is, the Inelastic Scattering Probability and the Inelastic Mean Free Path). Thus, in average, these small differences compensate and the observables of interest for electronic charge transport are not significantly affected. Thus, we decided to use the coarser grid.

2.4.4 Theory of Monte Carlo simulations

The transport of electrons within a material can be simulated by a classical MC approach, assuming that the non-relativistic electron beam wavelength is small with respect to interatomic separation [24] and that the scattering cross sections for the different processes occurring within materials are known.

At this level the target is assumed to be semi-infinite, homogeneous and amorphous, the latter conditions supporting the assumption of incoherent scattering between different events. In our transport model, we consider a mono-energetic electron beam with N electrons impacting on the target with kinetic energy T and angle of incidence θ with respect to the surface normal.

Electrons can undergo elastic and inelastic scattering. The scattering is usually elastic

when electrons scatter nuclei with far heavier mass, and only a trajectory change by an angle θ is recorded. In this case, the elastic cross section σ_{el} is calculated by using the Mott theory, which is based on the solution of the Dirac equation in a central field [34]. In contrast, inelastic scattering processes resulting in both an energy loss W and a directional change θ are mainly due to electron–electron interactions. In this occurrence, the inelastic cross section σ_{inel} is assessed via the dielectric model [23]. Within this approach the differential inelastic cross section is calculated as follows:

$$\frac{d\sigma_{inel}}{dW} = \frac{1}{\rho\pi a_0 T} \int_{q_-}^{q_+} \frac{dq}{q} \text{Im} \left[-\frac{1}{\epsilon(q, W)} \right] \quad (2.17)$$

where a_0 is the Bohr radius, ρ the atomic density of the target material, q is the transferred momentum and the integration limits are $q_- = \sqrt{2m}(\sqrt{T} - \sqrt{T - W})$ and $q_+ = \sqrt{2m}(\sqrt{T} + \sqrt{T - W})$.

The electron mean free path λ is given by [34]:

$$\lambda = \frac{1}{\rho(\sigma_{el} + \sigma_{inel})} \quad (2.18)$$

Furthermore, we assume that the path travelled by a test charge between two subsequent collisions is Poisson–distributed, so that the cumulative probability that the electron moves a distance Δs before colliding is given by:

$$\Delta s = -\lambda \cdot \ln(r_1) \quad (2.19)$$

The random numbers r_1 , as well as all random numbers employed in our MC simulations, are sampled in the range [0,1] with a uniform distribution. A second random number r_2 is compared with the elastic ($p_{el} = \frac{\lambda_{el}}{\lambda_{el} + \lambda_{inel}}$) and inelastic ($p_{inel} = 1 - p_{el}$) scattering probabilities to determine whether the scattering is elastic ($r_2 < p_{el}$) or inelastic ($r_2 \geq p_{el}$). The outcome of an elastic interaction is given by the trajectory deflection of an angle θ' with respect to the direction before the collision, which can be computed by equalizing the following cumulative elastic probability with a third random number r_3 :

$$P_{el}(\theta', T) = \frac{1}{\sigma_{el}} 2\pi \int_0^{\theta'} \frac{d\sigma_{el}}{d\theta} d\theta = r_3 \quad (2.20)$$

On the other hand, inelastic processes are dealt with by computing the inelastic scattering probability as:

$$P_{inel}(W, T) = \frac{1}{\sigma_{inel}} \int_0^W \frac{d\sigma_{inel}}{dW'} dW' = r_4 \quad (2.21)$$

As customary in electronic transport MC calculations, the maximum energy loss corresponds to half of the kinetic energy of the incident electron. To determine the energy loss W , we generate a database of P_{inel} values for different W and T and we equalize the integral in Eq. (2.21) to a random number r_4 .

The Monte Carlo routines used for performing these simulations are embedded in the in-house developed suite SURPRISES [35, 36].

2.5 Results and discussion

2.5.1 Frequency-dependent dielectric function of diamond and graphite

The central quantity of our analysis is represented by the dielectric function, which links the microscopic features of diamond and graphite, accessible from ab initio or model simulations, to REELS experimental data. The real and imaginary part of the frequency-dependent dielectric function of diamond and graphite from our ab initio simulations are reported respectively in Figs. (2.1) and (2.2) for several transferred momenta in the IBZ along the ΓL direction for diamond and along the ΓM direction for graphite. We notice that both real and imaginary parts of ϵ are strongly dependent on the transferred momentum, showing a high degree of anisotropy in the dielectric response for both solids. Furthermore, we stress that the dielectric function real and imaginary parts expected asymptotic behaviour (that is the real part goes to one, while the imaginary part goes to zero for increasing energy transfer at any \mathbf{q}) are rigorously satisfied for both solids.

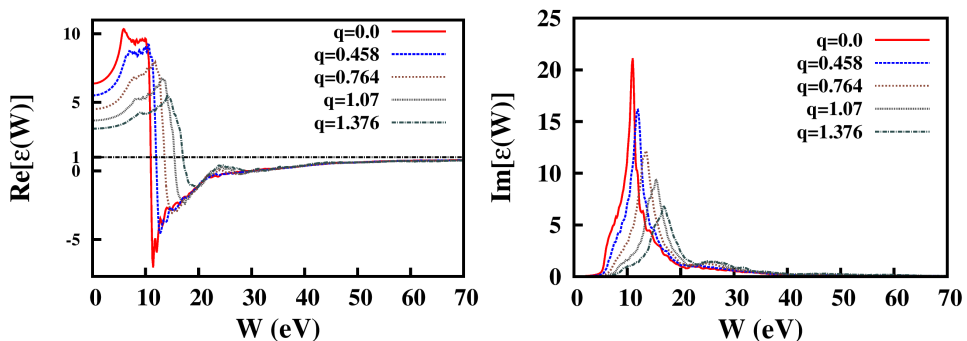


FIGURE 2.1: Real (left panel) and imaginary (right panel) parts of the dielectric function, obtained from ab initio calculations, of diamond vs. energy transfer (eV) for different momentum transfer q (\AA^{-1}) along the ΓL direction.

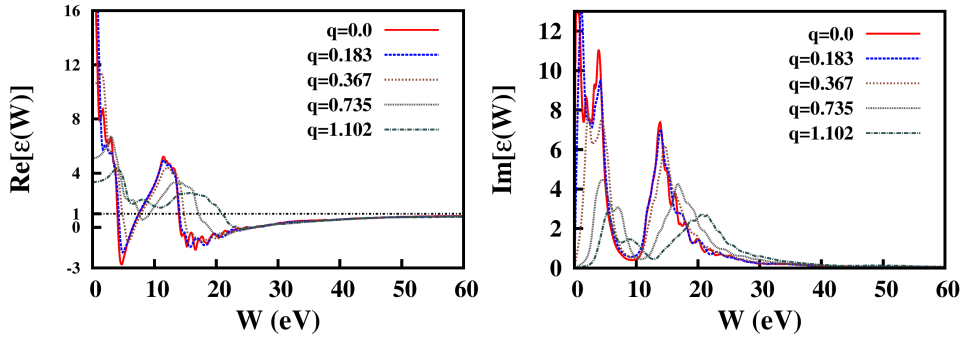


FIGURE 2.2: Real (left panel) and imaginary (right panel) parts of the dielectric function, obtained from ab initio calculations, of graphite vs. energy transfer (eV) for different momentum transfer q (\AA^{-1}) along the ΓM direction.

2.5.2 Frequency-dependent energy-loss functions of diamond and graphite

The ELF can be accurately computed via Eq. (2.11) within a full ab initio model once the dielectric function appearing in Eq. (2.16) is known in a fine grid of q points. A computationally less expensive approach could be used, in which the dielectric function in the optical limit is computed from ab initio simulations or taken from transmission electron energy-loss experimental data [10, 11] while the extension to finite momentum transfer is obtained by applying a RPA-type dispersion law. In this regard, to test the accuracy of different models, we calculated the ELF by three approaches.

Full ab initio (AI): Within this computational framework, the ELF was computed via full AI approach both for $\mathbf{q} \rightarrow 0$ and outside the optical limit. The ELF, plotted as a function of energy and momentum transfer along the ΓL (ΓM) direction for diamond (graphite), are shown in Figs. (2.3) and (2.4), respectively.

Drude-Lorentz from AI optical data (DL-AI): Within this approach, the dielectric response in the optical domain was still obtained from AI simulations of the dielectric function. The ELF was computed in the optical limit by using Eq. (2.11) and then fitted via DL-functions as indicated by Eq. (2.13). The extension to finite transfer momentum was finally achieved by using the dispersion law for plasmons reported in Eq. (2.12).

In the case of diamond, four harmonic oscillators were sufficient to obtain an optimal fit of the AI optical data, while for graphite only two harmonic oscillators were used. In Fig. (2.5) we compare the AI dielectric response (red curve) for diamond (left

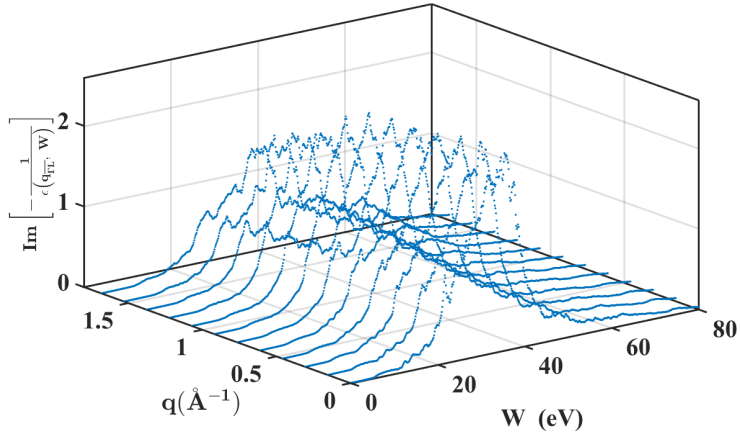


FIGURE 2.3: ELF of diamond, obtained from ab initio simulations vs. energy (eV) and momentum (\AA^{-1}) transfer along the IBZ Γ L direction.

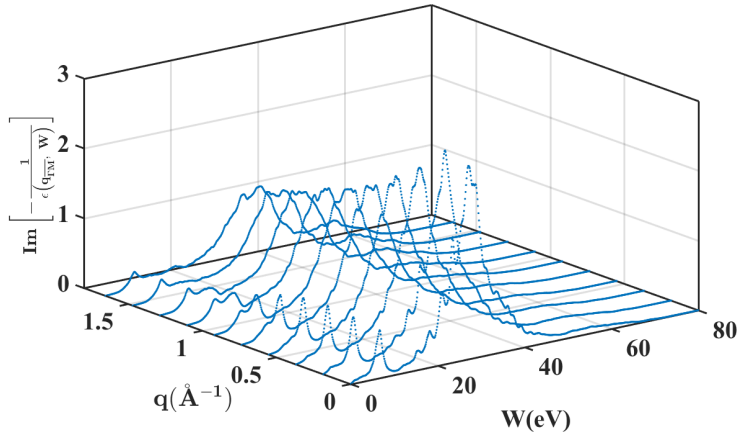


FIGURE 2.4: ELF of graphite, obtained from ab initio simulations vs. energy (eV) and momentum (\AA^{-1}) transfer along the IBZ Γ M direction.

panel) and graphite (right panel) obtained in the optical limit with the DL fit (dashed black line).

The fitting parameters E_n , Γ_n and A_n have a clear physical meaning, representing

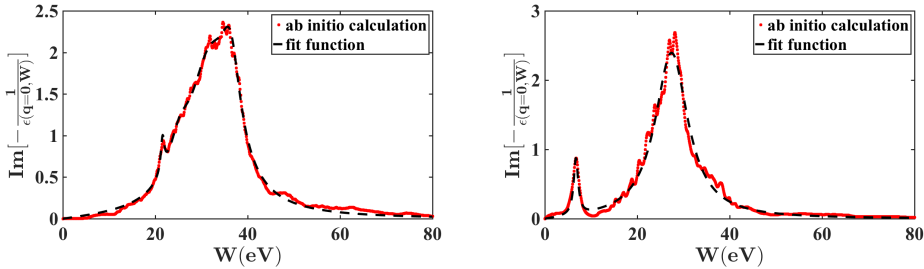


FIGURE 2.5: ELF in the optical limit ($\omega \rightarrow 0$) obtained from AI simulations (continuous red curve) along with the data fit (dashed black line) for diamond (left panel) and graphite (right panel).

respectively, the plasmon peak energies, the damping constants characterizing the finite life-time of the quasi-particle excitation, and the oscillator strengths. The parameters obtained from this fitting procedure are reported in Tab. (2.1) for diamond and graphite, respectively.

n	E_n (eV)	Γ_n (eV)	A_n (eV ²)
Diamond			
1	21.59	0.95	8.58
2	25.40	5.68	61.62
3	32.28	11.38	626.46
4	36.39	5.25	224.76
Graphite			
1	6.75	1.17	6.38
2	27.76	8.68	573.09

TABLE 2.1: Fitting parameters obtained by fitting the AI ELF in the optical limit with DL functions for diamond and graphite, respectively.

We notice that our fit functions satisfy the f -sum rule [37], stating that the integral of the ELF multiplied by the energy loss sums up to the number of effective-electrons per atom [38], i.e. the valence electrons in our model.

Drude-Lorentz from experimental optical data (DL-E): The ELF in the optical domain can be directly measured in transmission electron energy-loss experiments, fitted with DL functions as reported by Garcia-Molina *et al.* [39] and extended out of the optical limit by applying the dispersion law reported in Eq. (2.12).

In Fig. (2.6) we compare the ELF of diamond (left panel) and graphite (right panel) obtained from our AI simulations with the experimental data from Refs. [10] and [11]

and the fit model by Garcia-Molina *et al.* [39]. We notice that Garcia-Molina *et al.* used a different number of oscillators, plasmon peak energies and FWHM to accurately fit the experimental data with respect to our model derived from AI simulations.

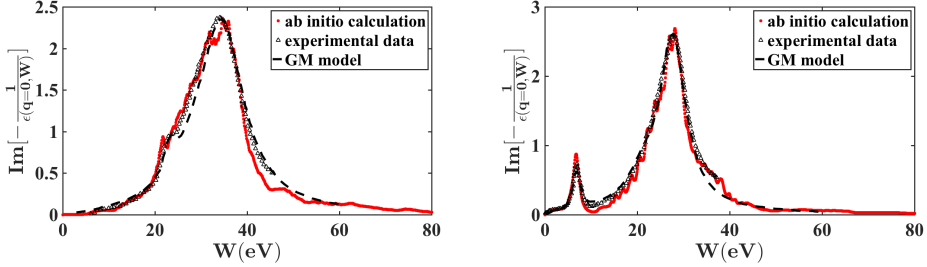


FIGURE 2.6: Comparison between the ELF of diamond (left panel) and graphite (right panel) in the optical limit obtained from AI simulations (continuous red curve), experimental data from Refs. [10] and [11] (black triangles) and fit obtained with the model of Garcia-Molina *et al.* [39] (dashed black line).

2.5.3 Inelastic Mean Free Path and Stopping Power

Using these different models of the ELF, we calculated a number of measurable physical quantities, such as the Inelastic Cross Section (ICS), the Inelastic Mean Free Path (IMFP) and the Stopping Power (SP). These quantities will be used as input to our Monte Carlo calculation of electron energy-loss spectra. We note that the IMFP (λ_{inel}), ICS (σ_{inel}) and the SP ($S(T)$) are given by:

$$\lambda_{\text{inel}} = \frac{1}{\rho\sigma_{\text{inel}}}, \quad \sigma_{\text{inel}} = \int_{E_g}^{\frac{T+E_g}{2}} \frac{d\sigma_{\text{inel}}}{dW} dW, \quad (2.22)$$

$$S(T) = \int_{E_g}^{\frac{T+E_g}{2}} \frac{\lambda_{\text{inel}}^{-1}}{dW} W dW$$

where ρ is the atomic density of the material. We notice that the upper and lower integration limits are, conventionally, fixed to the energy gap E_g and one half of the initial kinetic energy T plus the band gap energy E_g respectively. In Fig. (2.7) we plot the IMFP of diamond (left) and graphite (right) calculated according to the three approaches mentioned above. Calculations performed using the Tanuma-Powell-Penn (TPP) model [40] are also reported for reference: these results were obtained by including the K-shell excitations.

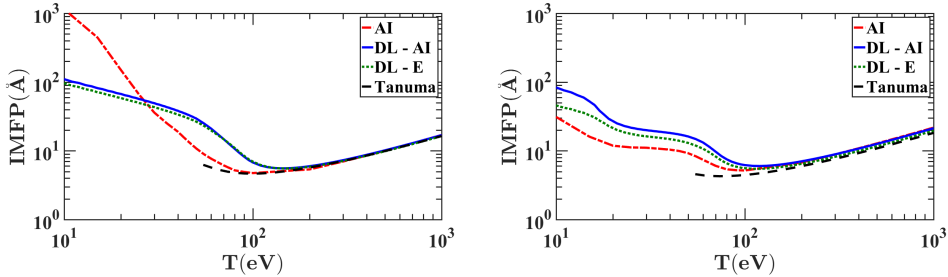


FIGURE 2.7: IMFP of diamond (left) and graphite (right). Data obtained from AI simulations are reported in red (AI), DL-AI in blue and with the DL-E in green. Black dashed lines correspond to the same quantities obtained by Tanuma *et al.* [40].

The agreement between the different approaches and Tanuma’s data is remarkably good, for both diamond and graphite, at energy transfers higher than 100 eV. However, for energies below 100 eV we find a significant discrepancy between the IMFP obtained by full AI calculations and the IMFP obtained via the DL dispersion law of Eq. (2.12) (about one order of magnitude in the case of diamond). The large discrepancy will also affect our Monte Carlo simulations: an AI IMFP bigger by one order of magnitude at low energy with respect to DL models means that electrons have significantly lower probability to undergo inelastic scattering within the target material. One can explain this substantial difference between the AI and DL models as due to the application of the quadratic dispersion law of Eq. (2.12). In fact, this dispersion law is obtained using an homogeneous electron gas model within a RPA framework, which fails in the case of wide band-gap semiconductors or insulators, such as diamond. On the other hand, this approximation works better for graphite, which shows an almost semi-metallic behaviour along the in-plane direction. Finally, the SP obtained by using the three different approaches is reported in Fig. (2.8) for diamond (left panel) and graphite (right panel) and is compared with previous simulations by Shinotsuka *et al.* [41]. Differently from our approach, the SP reported in Ref. [41] includes also K-shell excitations, similarly to the TTP calculations [40]. Discrepancies among the different approaches at energies below 100 eV are evident also in this case.

2.6 Monte Carlo simulations

2.6.1 Diamond energy-loss spectra

To compare our experimental REELS data of diamond with the three different models of ELF presented above, we performed Monte Carlo (MC) simulations following the

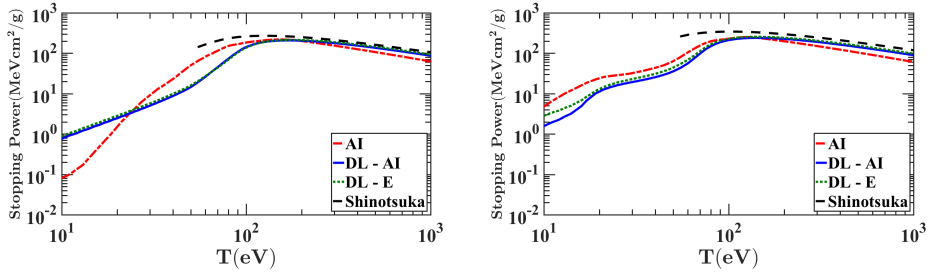


FIGURE 2.8: Stopping power of diamond (left panel) and graphite (right panel). Data obtained with the AI approach are reported in red, DL-AI in blue, DL-E in green. Results from Shinotsuka *et al.* [41] are sketched using a black dashed line.

scheme reported in section 2.4.4. In our MC simulations, diamond crystals are approximated by a homogeneous system with density 3.515 g/cm^3 [39]. Consequently, one assumes also that the ELF is almost similar in all directions and thus we can retain our simulated ELF along the ΓL direction for calculating the energy-loss spectra. The band gap of diamond was set equal to 4.16 eV, to be consistent with our DFT ab initio calculations. The electron-beam direction is orthogonal to the target surface and the initial kinetic energy ranges from 250 to 2000 eV. The number of impinging electrons is 10^9 .

In Fig. (2.9) spectra of backscattered electrons simulated in terms of the three different models of the ELF are compared with our REELS experimental data. We notice that we define as backscattered electrons those beam electrons reflected after both elastic and inelastic collisions. Simulated and experimental spectra present the σ plasmon peak at ~ 35 eV, related to the four valence electrons of the equivalent covalently bonded carbon atoms. This finding is in agreement with the ELF function of Fig. (2.3), showing a maximum at about the same energy.

Furthermore, the two-plasmon excitation at higher energy (~ 70 eV) in the experimental spectrum is also present in our MC simulations. We observe that while the MC simulations carried out using the dispersion law of Eq. (2.12) show a blue shift with respect to experimental data, the use of a full AI approach results in a better agreement with experiments. Incidentally, we notice that the DL approach seems to describe more accurately the experimental data at ~ 40 eV. We believe that this is due to the fact that DL linewidth of the plasmon peak is broader than the AI curve. The very same reason explains the poor description of the DL model of the experimental minimum between 40 and 50 eV. We can conclude that at least in the case of insulators, due to the strongly inhomogeneous electron density and, thus, to the complexity of the dielectric response, the DL model is quantitatively less accurate than a full AI approach in the prediction of the experimental REELS. This behaviour

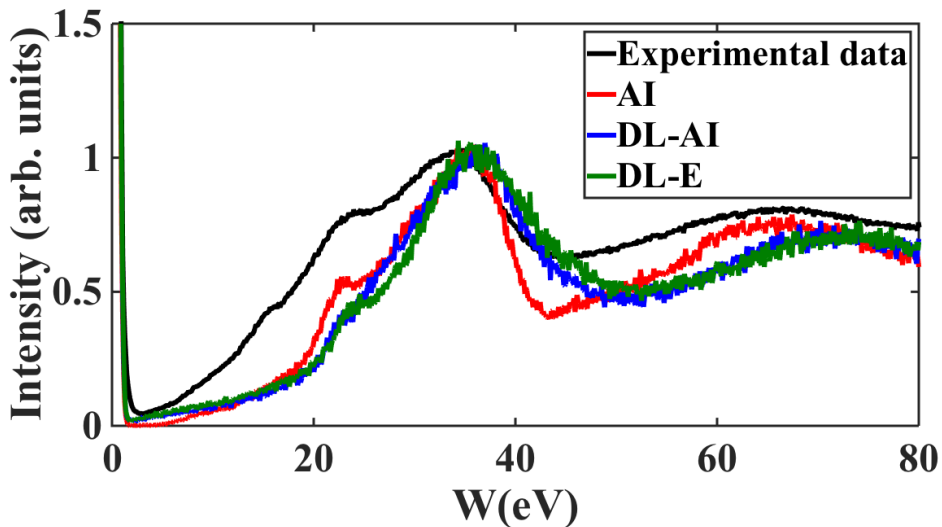


FIGURE 2.9: REELS of diamond: experimental data are reported in black, while simulated results using the three different dielectric models are sketched in red (AI), blue (DL-AI) and green (DL-E). Electron beam kinetic energy is 1000 eV. Data are normalized with respect to the σ plasmon peak.

worsens at higher transferred momenta, where particle-hole excitations, rather than collective plasma excitation, come into play. Single-particle excitations generally cannot be well described by a simple RPA or by the DL model of the ELF, while TDDFT AI simulations are also able to take into account these spectral features even if the ALDA functional is the basic approximation one can do.

REEL experimental spectra and MC simulated spectra obtained using the full AI method are compared in Fig. (2.10) for different kinetic energies of the primary beam. The agreement between our MC and experimental data improves with increasing kinetic energy. This behaviour is indeed expected as the MC approach assumes that electrons are classical point-like particles. Moreover, our simulated spectra do not include the surface plasmon contribution, whose importance decreases at higher electron beam kinetic energies.

2.6.2 Graphite energy-loss spectra

Graphite crystals were considered to have a density of 2.25 g/cm^3 [39]. The band gap was set equal to 0.06 eV according to our DFT calculations. MC simulations of REELS were carried out using the three different approaches to the calculation of the ELF

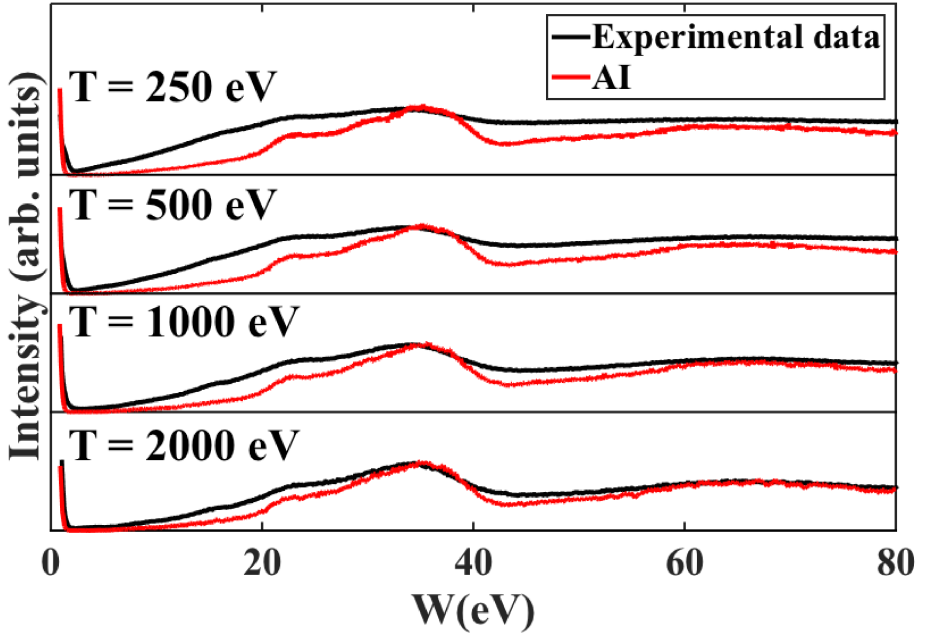


FIGURE 2.10: REELS of diamond obtained by calculating the ELF with the full AI approach (red line) at different momentum transfer compared to experimental data (black line) for several primary electron beam kinetic energies T . Data are normalized with respect to the σ plasmon peak.

mentioned above, with a number of electrons in the beam equal to 10^9 . Here, only the in-plane component of the energy loss function was dealt with in the calculation (i.e. we considered the component of the momentum transfer only along the single graphite layers). In Fig. (2.11) we report the MC REELS simulations compared to our experimental measurements (black line).

We notice that our MC simulations reproduce both the π (due to the collective excitation of valence electrons in the π band) and the $\pi + \sigma$ (due to collective excitation of all valence electrons) plasmon peaks. These findings are in agreement with the ELF function of Fig. (2.4), showing maxima at about same energies. While the results of the simulations show good agreement with experimental data independently of the ELF model, nevertheless, using the ab initio calculated ELF at finite momentum transfer, a third peak around 60 eV can be found. This peak corresponds to two-plasmon excitation, and its presence is less apparent by adopting DL models. Indeed, in DL models the RPA approximation describes the system as composed of

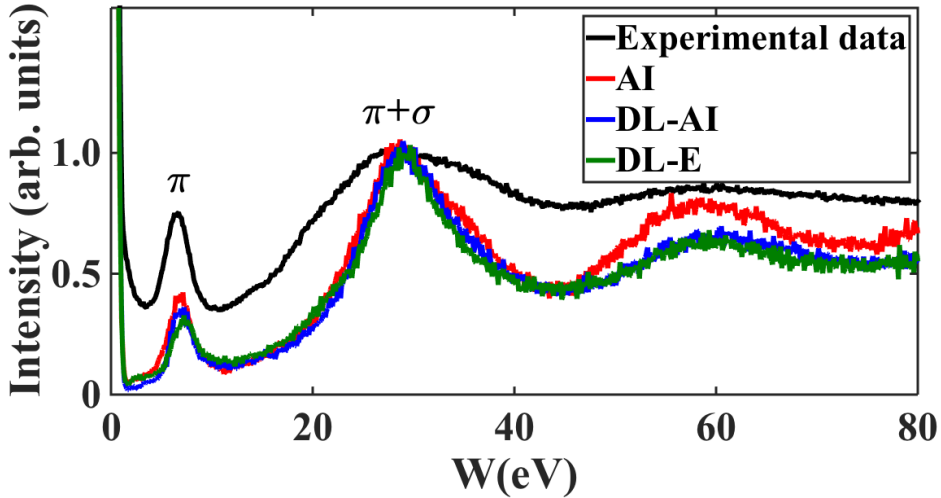


FIGURE 2.11: REEL spectra of graphite: experimental data are reported in black, while simulations using the 3 different models are sketched in red (AI), blue (DL-AI) and green (DL-E). Electron beam kinetic energy is 1000 eV. Data are normalized with respect to the $\pi + \sigma$ plasmon peak.

free electrons; in the case of graphite the electrons populating the π bands are delocalized and they behave as almost-free electrons. For this reason, the π plasmon peak is prominent in all three spectra. However we conclude that in the case of semi-metal such as graphite RPA works better and Drude-Lorentz simulations reproduce results similar to first principles approaches.

REEL experimental spectra and MC simulated spectra obtained for graphite using the full AI method are compared in Fig. (2.12) for different kinetic energies of the primary beam. The agreement between our MC and experimental data improves with increasing kinetic energy, as for diamond, in Fig. (2.10).

2.6.3 Graphite energy-loss spectra taking into account a model of anisotropy crystal directions

A further step for graphite was done by considering expression (2.22) as composed by two independent components: one along the plane direction, as previously done, and one orthogonal to the plane. In this way one can be able to treat the anisotropic structure of graphite.

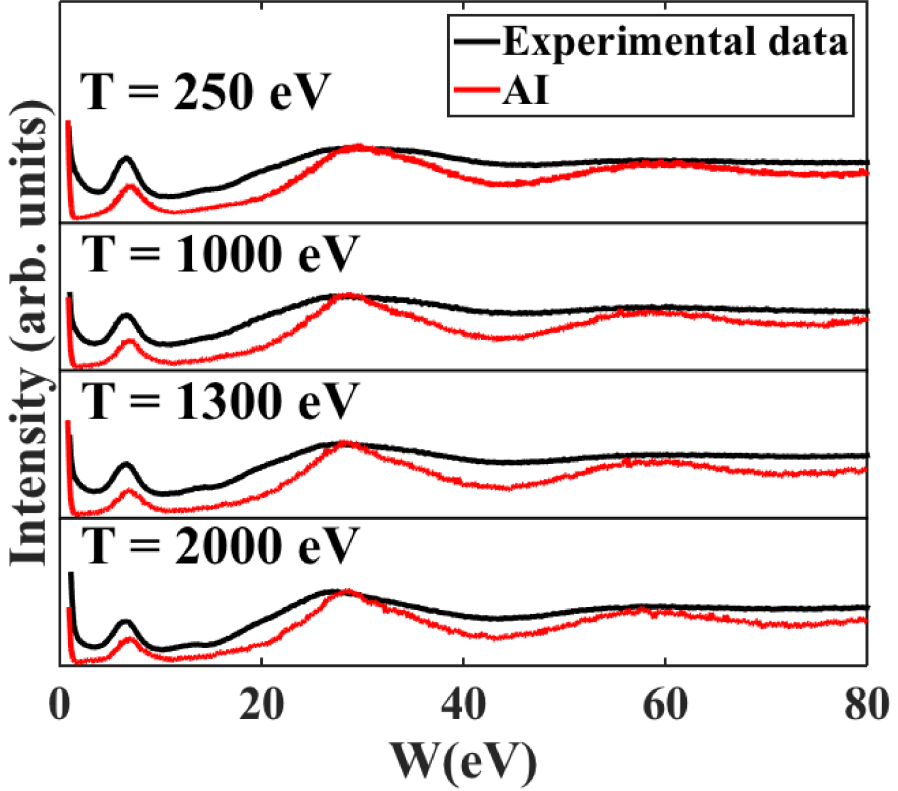


FIGURE 2.12: REEL spectra of graphite obtained by calculating the ELF with the full AI approach (red line) at different momentum transfer compared to experimental data (black line) at different primary electron beam kinetic energy T . Data are normalized with respect to the $\pi + \sigma$ plasmon peak.

The total IMFP λ_{inel} and energy loss W were determined by linearly combining at each inelastic interaction the corresponding values along the two possible orthogonal directions of the transferred momentum \mathbf{q} as follows:

$$\lambda_{inel} = f \cos^2 \theta \lambda_{||} + [(1 - f) + f \sin^2 \theta] \lambda_{\perp} \quad (2.23)$$

$$W = f \cos^2 \theta W_{||} + [(1 - f) + f \sin^2 \theta] W_{\perp} \quad (2.24)$$

where f is an *anisotropy parameter* in the range $[0,1]$, and θ is the angle between \mathbf{c} and \mathbf{q} . The f parameter has been introduced in this anisotropic model of the inelastic observables to favour the electron motion in the planar direction, since HOPG shows a higher conductivity along the plane ($\mathbf{q} \perp \mathbf{c}$). The value of f is determined to obtain the best agreement between theoretical and experimental spectra and as can be seen from Fig. (2.13), we choose a value $f = 0.6$ that give us the best accordance with experimental data.

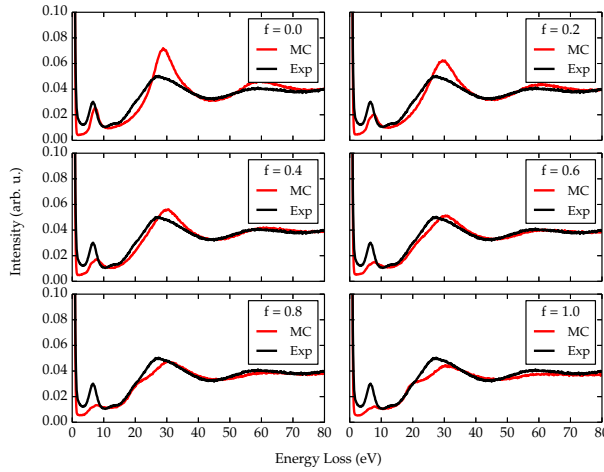


FIGURE 2.13: REELS of HOPG for different values of the f parameter (red lines). The kinetic energy of the primary beam is set to 1500 eV. MC calculations are compared with our experimental data (black lines). The results are normalized at a common area of the elastic peak.

The higher the value of f , the larger is the contribution of intra-planar excitations ($\mathbf{q} \parallel \mathbf{c}$) to inelastic interactions. This effect can be noticed in the spectra of Fig. (2.13) by the rise of a shoulder at an energy loss of 20 eV, which corresponds to an oscillation in the ELF along the $\mathbf{q} \parallel \mathbf{c}$ direction. This means physically that by considering e.g. a scattering angle $\theta = 0$ (that is, orthogonal to the graphite layers), the energy loss embeds 60% of collisions with a transferred momentum along the $\mathbf{q} \parallel \mathbf{c}$ direction, while 40% of the spectrum is made by collisions along the $\mathbf{q} \perp \mathbf{c}$ (in-plane) direction (see Eqs. (2.23) and (2.24)). Of course, the directional change of the electrons inelastically scattered by the target nuclei is taken into account, for fixed f , by the scattering angle θ , which is modified by the interactions at each MC step. This anisotropic model is consistent with the higher tendency of the electrons to move along the graphite planes rather than across the planes.

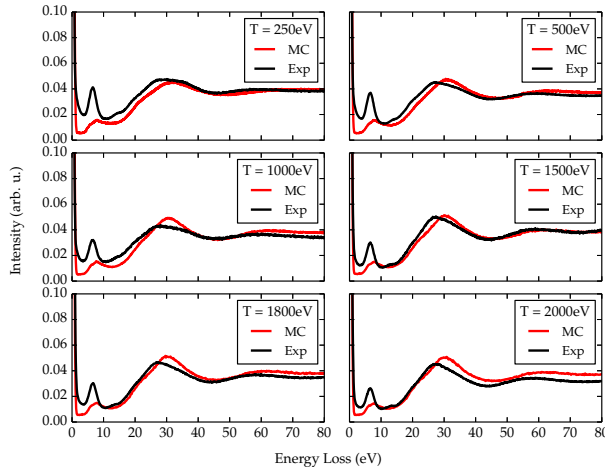


FIGURE 2.14: REELs of HOPG for several primary beam kinetic energies. Red lines show simulated spectra, while black curves report our experimental data. The results are normalized at a common area of the elastic peak.

As in the previous section, MC simulations were performed at several primary beam kinetic energies and compared with the experimental data (normalized at a common area of the elastic peak) in Fig. (2.14). We notice that the agreement between calculated and experimental data is rather good and becomes progressively better for increasing kinetic energies. This is due to the fact that experimental spectra report also the contribution of surface plasmons, which is neglected in the MC calculations and whose relative importance diminishes with respect to bulk plasmons at higher values of the primary beam kinetic energy. It is worth noting that the normalization of the data at a common area of the elastic peak keeps the correct intensity ratios between the two main plasmon peaks.

2.7 Conclusions

In this work, we calculated the dielectric properties of diamond and graphite, in particular the dielectric response and the energy-loss functions, using different approaches, from semiclassical Drude–Lorentz to time-dependent density functional theory. We compare our computer simulations with REEL spectra recorded at several energies. The major result of this work is to point out that an accurate treatment of the electron–electron correlations beyond the random phase approximation of the

homogeneous Fermi gas increases the overall accuracy of the model and provides a better agreement with measurements of back-scattered electrons. This issue is particularly important in materials with highly inhomogeneous charge densities, such as semiconductors and insulators, out of the optical region where collective plasmon excitations mix with single particle-hole excitations. Semi-classical models, based on the Drude-Lorentz extension to finite momentum transfer, are generally less accurate in reproducing these quantum effects. Nevertheless, this finding turns out to be correct also for semimetals, such as graphite, even though in this case the accuracy of the free-electron model (as the RPA) with respect to the energy-loss spectral observables does not differ significantly from the *ab initio* model. Thus, the advantage of using a full *ab initio* description of the electron scattering within the solid, particularly at low energy (< 100 eV) where the classical Monte Carlo approach of the present work is not rigorously applicable, clearly emerges from our computational analysis. Furthermore, we notice that the approach used for including a dependence of the dielectric properties on the target anisotropy clearly improves the agreement between simulated and experimental REEL spectra. Finally, further developments of this work will be sought for the inclusion of the electron-phonon interaction, which is relevant at low energies, for the treatment of the surface plasmons and anisotropy effects in 2D carbon materials. Also, the performance of the semi-empirical optical data model could be improved by adding exchange-correlation effects [42, 43].

Bibliography

- [1] C. Kittel, *Introduction to Solid State Physics*, Wiley, 2004.
URL <https://books.google.it/books?id=kym4QgAACAAJ>
- [2] <http://elk.sourceforge.net/>.
- [3] D. J Singh, L. Nordström, *Planewaves, Pseudopotentials and the LAPW Method*, Second Edition, 2005. doi:10.1007/978-0-387-29684-5.
- [4] P. Hohenberg, W. Kohn, Inhomogeneous electron gas, *Phys. Rev.* 136 (1964) B864–B871. doi:10.1103/PhysRev.136.B864.
URL <https://link.aps.org/doi/10.1103/PhysRev.136.B864>
- [5] W. Kohn, L. J. Sham, Self-consistent equations including exchange and correlation effects, *Phys. Rev.* 140 (1965) A1133–A1138. doi:10.1103/PhysRev.140.A1133.
URL <https://link.aps.org/doi/10.1103/PhysRev.140.A1133>
- [6] J. Harl, *The linear response function in density functional theory: optical spectra and improved description of the electron correlation*, Ph.D. thesis, University of Vienna (2008).

- [7] J. P. Perdew, K. Burke, M. Ernzerhof, Generalized gradient approximation made simple, *Phys. Rev. Lett.* 77 (1996) 3865–3868. doi:10.1103/PhysRevLett.77.3865.
URL <https://link.aps.org/doi/10.1103/PhysRevLett.77.3865>
- [8] M. A. Marques, M. J. Oliveira, T. Burnus, Libxc: A library of exchange and correlation functionals for density functional theory, *Computer Physics Communications* 183 (10) (2012) 2272 – 2281. doi:<https://doi.org/10.1016/j.cpc.2012.05.007>.
URL <http://www.sciencedirect.com/science/article/pii/S0010465512001750>
- [9] Y. Li, A. Chernikov, X. Zhang, A. Rigosi, H. M. Hill, A. M. van der Zande, D. A. Chenet, E.-M. Shih, J. Hone, T. F. Heinz, Measurement of the optical dielectric function of monolayer transition-metal dichalcogenides: MoS₂, MoSe₂, WS₂, and WSe₂, *Phys. Rev. B* 90 (2014) 205422. doi:10.1103/PhysRevB.90.205422.
URL <http://link.aps.org/doi/10.1103/PhysRevB.90.205422>
- [10] J. Daniels, C. v. Festenberg, H. Raether, K. Zeppenfeld, Optical constants of solids by electron spectroscopy, in: *Springer Tracts in Modern Physics, Volume 54*, Springer, 1970, pp. 77–135.
- [11] H. Raether, *Excitation of plasmons and interband transitions by electrons*, Vol. 88, Springer, 1980.
- [12] S. Baroni, R. Resta, *Ab initio* calculation of the macroscopic dielectric constant in silicon, *Phys. Rev. B* 33 (1986) 7017–7021. doi:10.1103/PhysRevB.33.7017.
URL <http://link.aps.org/doi/10.1103/PhysRevB.33.7017>
- [13] M. Dapor, G. Garberoglio, L. Calliari, Energy loss of electrons impinging upon glassy carbon, amorphous carbon, and diamond: Comparison between two different dispersion laws, *Nuclear Instruments and Methods in Physics Research Section B: Beam Interactions with Materials and Atoms* 352 (2015) 181 – 185. doi:<http://dx.doi.org/10.1016/j.nimb.2014.11.115>.
URL <http://www.sciencedirect.com/science/article/pii/S0168583X14010246>
- [14] M. Dapor, L. Calliari, M. Filippi, Computational and experimental study of π and $\pi + \sigma$ plasmon loss spectra for low energy (< 1000 eV) electrons impinging on highly oriented pyrolytic graphite (HOPG), *Nuclear Instruments and Methods in Physics Research Section B: Beam Interactions with Materials and Atoms* 255 (1) (2007) 276 – 280. doi:<http://dx.doi.org/10.1016/j.nimb.2006.11.029>.
URL <http://www.sciencedirect.com/science/article/pii/S0168583X06011244>

- [15] E. Runge, E. K. U. Gross, Density-functional theory for time-dependent systems, *Phys. Rev. Lett.* 52 (1984) 997–1000. doi:10.1103/PhysRevLett.52.997.
URL <http://link.aps.org/doi/10.1103/PhysRevLett.52.997>
- [16] C. A. Ullrich, *Time-Dependent Density Functional Theory: Concepts and Applications*, Oxford Graduate Texts, 2012.
- [17] H. T. Nguyen-Truong, Low-energy electron inelastic mean free path in materials, *Applied Physics Letters* 108 (17) (2016) 172901.
- [18] C. Chantler, J. Bourke, Electron inelastic mean free path theory and density functional theory resolving discrepancies for low-energy electrons in copper, *The Journal of Physical Chemistry A* 118 (5) (2014) 909–914.
- [19] A. Sorini, J. Kas, J. Rehr, M. Prange, Z. Levine, Ab initio calculations of electron inelastic mean free paths and stopping powers, *Physical Review B* 74 (16) (2006) 165111.
- [20] R. Garcia-Molina, I. Abril, I. Kyriakou, D. Emfietzoglou, Inelastic scattering and energy loss of swift electron beams in biologically relevant materials, *Surface and Interface Analysis* 49 (1) (2017) 11–17.
- [21] S. L. Adler, Quantum theory of the dielectric constant in real solids, *Phys. Rev.* 126 (1962) 413–420. doi:10.1103/PhysRev.126.413.
URL <http://link.aps.org/doi/10.1103/PhysRev.126.413>
- [22] N. Wisser, Dielectric constant with local field effects included, *Phys. Rev.* 129 (1963) 62–69. doi:10.1103/PhysRev.129.62.
URL <http://link.aps.org/doi/10.1103/PhysRev.129.62>
- [23] R. H. Ritchie, Plasma losses by fast electrons in thin films, *Phys. Rev.* 106 (1957) 874–881. doi:10.1103/PhysRev.106.874.
URL <http://link.aps.org/doi/10.1103/PhysRev.106.874>
- [24] H. Nikjoo, S. Uehara, D. Emfietzoglou, *Interaction of radiation with matter*, CRC Press, 2012.
- [25] H. Nikjoo, D. Emfietzoglou, T. Liamsuwan, R. Taleei, D. Liljequist, S. Uehara, Radiation track, dna damage and response—a review, *Reports on Progress in Physics* 79 (11) (2016) 116601.
- [26] M. Dapor, Energy loss of fast electrons impinging upon polymethylmethacrylate, *Nuclear Instruments and Methods in Physics Research Section B: Beam Interactions with Materials and Atoms* 352 (2015) 190 – 194. doi:<http://dx.doi.org/10.1016/j.nimb.2014.11.101>.
URL <http://www.sciencedirect.com/science/article/pii/S0168583X14010027>

- [27] F. Yubero, S. Tougaard, Model for quantitative analysis of reflection-electron-energy-loss spectra, *Phys. Rev. B* 46 (1992) 2486–2497. doi:10.1103/PhysRevB.46.2486.
URL <http://link.aps.org/doi/10.1103/PhysRevB.46.2486>
- [28] F. Sottile, Response functions of semiconductors and insulators: from the Bethe – Salpeter equation to time-dependent density functional theory, Ph.D. thesis, Ecole Polytechnique (2003).
- [29] S. Sharma, J. Dewhurst, A. Sanna, E. Gross, Bootstrap approximation for the exchange-correlation kernel of time-dependent density-functional theory, *Physical review letters* 107 (18) (2011) 186401.
- [30] S. Waidmann, M. Knupfer, B. Arnold, J. Fink, A. Fleszar, W. Hanke, Local-field effects and anisotropic plasmon dispersion in diamond, *Physical Review B* 61 (15).
- [31] J. Harl, The linear response function in density functional theory: Optical spectra and improved description of the electron correlation, Ph.D. thesis, Universitat Wien (2008).
- [32] J. P. Perdew, K. Burke, M. Ernzerhof, Generalized gradient approximation made simple, *Physical review letters* 77 (18) (1996) 3865.
- [33] J. P. Perdew, Y. Wang, Accurate and simple analytic representation of the electron-gas correlation energy, *Phys. Rev. B* 45 (1992) 13244–13249. doi:10.1103/PhysRevB.45.13244.
URL <http://link.aps.org/doi/10.1103/PhysRevB.45.13244>
- [34] M. Dapor, *Electron-Beam Interactions with Solids: Application of the Monte Carlo Method to Electron Scattering Problems*, Springer Tracts in Modern Physics, Springer Berlin Heidelberg, 2003.
URL <https://books.google.it/books?id=h71sCQAAQBAJ>
- [35] S. Taioli, S. Simonucci, M. Dapor, Surprises: when ab initio meets statistics in extended systems, *Computational Science & Discovery* 2 (1) (2009) 015002.
URL <http://stacks.iop.org/1749-4699/2/i=1/a=015002>
- [36] S. Taioli, S. Simonucci, L. Calliari, M. Filippi, M. Dapor, Mixed ab initio quantum mechanical and MonteCarlo calculations of secondary emission from SiO₂ nanoclusters, *Physical Review B* 79 (8) (2009) 085432.
- [37] E. Shiles, T. Sasaki, M. Inokuti, D. Y. Smith, Self-consistency and sum-rule tests in the Kramers – Kronig analysis of optical data: Applications to aluminum, *Phys. Rev. B* 22 (1980) 1612–1628. doi:10.1103/PhysRevB.22.1612.
URL <http://link.aps.org/doi/10.1103/PhysRevB.22.1612>

- [38] I. Abril, R. Garcia-Molina, C. D. Denton, F. J. Pérez-Pérez, N. R. Arista, Dielectric description of wakes and stopping powers in solids, *Physical Review A* 58 (1) (1998) 357.
- [39] R. Garcia-Molina, I. Abril, C. D. Denton, S. Heredia-Avalos, Allotropic effects on the energy loss of swift H^+ and He^+ ion beams through thin foils, *Nuclear Instruments and Methods in Physics Research Section B: Beam Interactions with Materials and Atoms* 249 (1 - 2) (2006) 6 - 12. doi:<http://dx.doi.org/10.1016/j.nimb.2006.03.011>.
URL <http://www.sciencedirect.com/science/article/pii/S0168583X06002473>
- [40] S. Tanuma, C. J. Powell, D. R. Penn, Calculations of electron inelastic mean free paths. IX. Data for 41 elemental solids over the 50 eV to 30 keV range, *Surface and Interface Analysis* 43 (3) (2011) 689–713. doi:10.1002/sia.3522.
URL <http://dx.doi.org/10.1002/sia.3522>
- [41] H. Shinotsuka, S. Tanuma, C. Powell, D. Penn, Calculations of electron stopping powers for 41 elemental solids over the 50 eV to 30 keV range with the full Penn algorithm, *Nuclear Instruments and Methods in Physics Research Section B: Beam Interactions with Materials and Atoms* 270 (2012) 75 - 92. doi:<http://dx.doi.org/10.1016/j.nimb.2011.09.016>.
URL <http://www.sciencedirect.com/science/article/pii/S0168583X11008809>
- [42] D. Emfietzoglou, I. Kyriakou, R. Garcia-Molina, I. Abril, Inelastic mean free path of low-energy electrons in condensed media: beyond the standard models, *Surface and Interface Analysis* 49 (2017) 4 - 10.
- [43] D. Emfietzoglou, I. Kyriakou, R. Garcia-Molina, I. Abril, The effect of static many-body local-field corrections to inelastic electron scattering in condensed media, *Journal of Applied Physics* 114 (14) (2013) 144907.

Chapter 3

Graphene allotropes with lower densities

In this chapter we discuss an approach to produce novel two-dimensional carbon-based materials using graphene topology as a texture, some of which are studied for the first time to the best of our knowledge. We model the structures using periodic simulation supercells as well as we make use of DFT to characterise their electronic (band structures and DOS), mechanical (stress-strain characteristics and relevant elastic observables) and dynamical stability properties. Nevertheless, here we use the pseudopotential approach to deal with the ion-electron interaction implemented in [1].

3.1 Aim of the work

The possibility to introduce new interesting features in bi-dimensional carbon-based materials without chemical functionalization, while keeping the desirable properties of graphene, such as its planar periodic structure and the sp^2 bonding network, might be very convenient to the existing technology. In this regard, one of the most striking properties of graphene is its Young's modulus to density ratio, probably the highest achieved so far. Unfortunately, investigations on this topic have been rarely pursued except for some notable exceptions [2, 3, 4, 5].

In this work we propose first a method based on the augmentation of regular and semi-regular tessellations of the plane with three-connected vertices. We show in particular the application of this approach for finding novel energetically stable sp^2 -bonded carbon-based structures under the locally jammed packing condition, aiming to find planar geometries with density lower than graphene. Our ultimate goal is to possibly decrease the surface density up to the least dense form of carbon allotrope

that could ever be synthesized, while displaying almost unchanged specific mechanical characteristics with respect to graphene. Indeed, one of the possible routes to increase the specific modulus with respect to graphene can be achieved via reducing the surface density. Increasing the specific modulus by decreasing the mass density is a typical request whereby the minimum structural weight can be achieved. This challenge has far-reaching consequences in a variety of applications, most notably in aerospace technologies where weight saving is a route to cost reduction. Furthermore we show that this method can be extended to a larger class of planar tessellations, such as the Cairo tiling. Using Density Functional Theory (DFT), the stability of these parent and augmented carbon structures is probed by calculating the phonon dispersions, while their response to external deformation and electromagnetic fields is characterized by assessing the stress–strain curves, including their specific mechanical properties, and the electronic band structures.

Our analysis shows the capability of this approach to design novel lightweight strong two-dimensional carbon allotropes, possibly extendable to three-dimensional architectures, and we find that the mechanical rigidity of graphene is very much depleted by decreasing the density, while other specific mechanical characteristics, such as the strength and toughness, can be even bigger than graphene.

3.2 Methods and computational details

3.2.1 Augmentation method for lowering the structure density

The structure of graphene-like materials corresponding to the three-coordinated regular and semi-regular tessellations can be represented by the packing of congruent discs touching each other exactly in three points. A two-dimensional packing can be achieved by a collection of congruent discs in the plane under the following constraints:

- No discs overlap
- Each disc is in contact with at least another disc
- For any choice of two discs in the packing there is always a path connecting them through mutual contacts.

In our approach to augmentation we impose three further constraints to restrict the possible structural search. These are the three-coordination of atomic centers, the maximum angle between two bonds, which must be below π rad, and the periodicity in the plane. Indeed, angle strain in sp^2 carbon allotropes increases noticeably when far from the equilibrium configuration equal to $2\pi/3$ rad. The angle choice lower than π rad corresponds to a specific condition for packing, called *local stability* or *locally jammed packing*. For locally stable disc packing, contacts between circles should

lie not all on the same semicircle [6]. With such a constraint in place, one might wonder whether packings of arbitrarily low density exist or, in case they do not, what the least dense arrangement of discs in the plane would be. It is an interesting question on its own, given that the question addressing the opposite problem – that of finding the densest arrangement of discs in the plane – received much attention for a long time [7, 8] and found a formal answer only in the last century [9]. In this regard, it is worth noticing that if the packing is allowed to be non-periodic, then discs can indeed be packed into locally stable configurations with arbitrarily low density [10].

To decrease the structure density of three-coordinated regular and semi-regular nets, our method proceeds first by substituting every disc of the parent structure with three smaller congruent discs inscribed in the former whose centers are arranged in an equilateral triangle, a process called augmentation when referred to nets [11]. The inscribed discs, representing the daughter geometry, are designed so that they touch each other to respect the locally jamming condition.

In the equivalent description, in which we place a carbon atom at the center of each disc, a daughter net emerges which corresponds to design equilateral triangles around every vertex of the parent net. The utility of the latter representation is due to the fact that can be generalized to the case of non-regular polygons also containing n -coordinated vertices, where the daughter net is created via augmentation by regular n -polygons. This extension consists in particular of a first step in which each n -coordinated node is augmented by a polygon with the same number of vertices, resulting in a three-coordinated net, followed by a second step in which the three-coordinated net is further augmented by triangles only. This procedure stops after reaching triangular nodes, as a further augmentation would fail the local jamming conditions by producing angles equal to π rad. We notice that the class of possible structures that can be augmented is in principle infinite, nevertheless the final density is likely to present a lower bound strictly related to the initial parent structure. We will show an application of this generalized tessellation which goes beyond regular and semi-regular polygons to the Cairo pentagonal tiling in which two vertices of the unit cell are four-coordinated.

3.2.2 Structure optimization

The optimization of the atomic positions, electronic and phonon band structure simulations, as well as the assessment of the mechanical properties of the proposed architectures were performed within the DFT framework using the QUANTUM ESPRESSO (QE) suite [1]. QE is a plane-wave code based on the pseudopotential approach to deal with the interaction between valence electrons and lattice ions. Optimization of the atomic configurations was carried out by using Broyden–Fletcher–Goldfarb–Shannon (BFGS) algorithm. The simulation cells in the orthogonal direction to the plane of the structures was set to 20 Å, in order to avoid spurious interactions among

periodic images. The optimized configurations of all the structures investigated in this work can be found in the electronic supplementary material.

3.2.3 Phonon band structure simulations

To assess the stability of the parent and daughter structures we computed the phonon bands using the *ph.x* utility of QE. We used the LDA (as advised in phonon dispersion simulations [1]) ultrasoft pseudopotential *C.pz-rrkjus.UPF*, with a cut-off of 30 Ry for wavefunctions and 240 Ry for the density, respectively. These cut-off values were set-up after achieving a well-converged phonon band structure of graphene in comparison to experiments and previous simulations. The *k*-point grids used to carry out phonon calculations depend on the simulation cell size and were chosen so to achieve converged DFT values below chemical accuracy (< 0.01 eV for the total energy and $< 10^{-3}$ Ry/Å for the interatomic forces). Thus, depending on the simulation cell we performed calculations on $2 \times 2 \times 1$ up to $16 \times 16 \times 1$ *k*-point grids for structural optimization, while increasing the *k*-point mesh to $48 \times 48 \times 1$ for the calculation of the band structures. Convergence of the integrals over the Brillouin zone was improved by smearing the occupancy with a 0.136 eV width Gaussian function. Simulation cells were carefully relaxed to achieve the minimum-energy configurations with respect to this pseudopotential. The convergence threshold for the self-consistent electronic structure simulations was set to 10^{-14} Ry and to 10^{-17} Ry for the phonon calculations. These small values of the thresholds were necessary to avoid the appearance of spurious imaginary frequencies, not due to the structural arrangement.

3.2.4 Electronic band structure and DOS

To carry out DFT electronic band structure simulations we used a norm conserving PBE pseudopotential (*C.pbe-mt_gipaw.UPF*) and an energy cut-off for the wavefunctions equal to 100 Ry. This large value of the plane-wave cut-off is due to obtaining converged values of the stress tensor, an observable notoriously more difficult to converge with respect to the total energy. The *k*-point grids used to calculate observables in the momentum space are the same than those used in phonon band structure calculations.

3.2.5 Mechanical properties

The mechanical properties were assessed by using the same parameters of the electronic band structure simulations (see section 3.2.4). For carrying out the calculation of the mechanical properties in linear regime we used 0.001-spaced points up to 0.01 strain and further 0.005-spaced points up to 0.05 strain. To deal with the elastic deformations we used supercells containing two unit cells for the materials with trigonal symmetry, i.e. the graphene and the flakene families. The C_{11} coefficient in

these cases is related to the strain along the zig-zag direction. Upon deformation, the atomic positions within the supercell were relaxed until interatomic forces were smaller than 10^{-3} Ry/Å. In this regard, we stress that in our ab-initio simulations we assess thus the “*true stress*”, so the simulation supercell is allowed to change in the direction orthogonal to the loading to obtain atomic forces below 0.5 kbar, equivalent to $0.5 \times 20/3.35 = 3$ kbar. In fact, the calculation of the stress in the bi-dimensional material relies on the choice of a conventional thickness, which was set to 3.35 Å for the graphene monolayer, while 20 Å is the dimension of our simulation cell.

3.3 Results and discussion

3.3.1 Parent and augmented geometries with low density

In this section we discuss the application of our augmentation approach under the locally-jammed constraints to generate novel sp^2 carbon-based architectures. We start from an initial parent topology and proceed to generate daughter architectures derived by lowering the packing of congruent discs, whose arrangement can be alternatively used to represent regular and semi-regular bi-dimensional crystal systems, under the condition of local stability.

Graphene and graphene daughter.

Consider the packing of discs associated with the structure of graphene. This arrangement has density of $\pi/(3\sqrt{3}) \sim 0.6046$, as shown in the middle-left panel of figure (3.1a), and defines the structural net of graphene reproduced in the left hand side of figure (3.1b). Now replacing each disc with three smaller discs (reducing thus the disc radius by a factor $\frac{1}{1+2/\sqrt{3}}$ with respect to the radius of graphene discs) leads to a less dense packing $\pi(7\sqrt{3}) - 12 \sim 0.390675$, as shown in the middle-right panel of figure (3.1a). The resulting structure, which we name “*graphene daughter*” (gr11 in [12]), corresponds to a semi-regular tessellation and is reproduced in the right hand side of figure (3.1b). Unfortunately, the substitution cannot be pursued any further as contacts between circles on the half-hemicircle would occur and spoil the local stability condition. This applies to any packing, whose associated net (or tiling) contains triangles.

Tilene parent and tilene.

By considering semi-regular tiling with polygons having four and eight sides, in the middle-left panel of figure (3.1c) we show what is probably the simplest structure after graphene, that is the packing associated with the well known square-octagon tiling. This defines a net of carbon atoms that we label “*tilene parent*” (octagraphene in

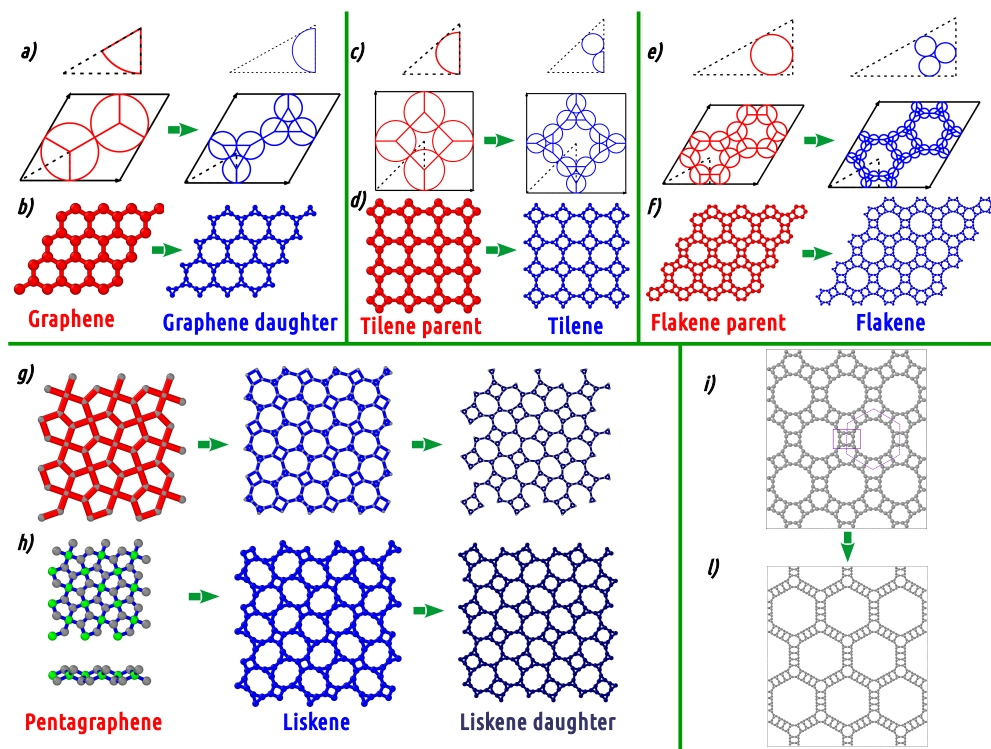


FIGURE 3.1: First row: in the upper panel parent (left, red color) and daughter (right, blue color) disc packing in the unit cells of a) graphene, c) tilene, and e) flakene. The lines internal to the discs connect the nearest neighbor discs. Bottom panel of the first row: 4 × 4 supercells of parent (left) and daughter (right) structures of b) graphene, d) tilene, and f) flakene. Second row: g) from left to right: pentagraphene structure; augmentation of the Cairo pentagonal tiling: liskene; further augmentation of the liskene geometry: liskene daughter. h) from left to right: top and side view of a 3 × 3 pentagraphene supercell, where the sp^3 -hybridized carbon atoms are reported in green color, while in grey we find the sp^2 -hybridized carbon centers; 3 × 3 supercell of liskene and liskene daughter after performing DFT minimization. i) By relaxing the locally jammed packing constraint, the flakene structure can be made progressively less dense by elongating the hexagonal super-ring side highlighted in the picture. j) The low density structure obtained from flakene by doubling the hexagonal super-ring side length.

[12]), which is reported in the left hand side of figure (3.1d). Its packing factor is $\pi(3 - 2\sqrt{2}) \sim 0.539012$, which is lower than that of graphene. Its augmentation, carried out under the previously described principles, leads to an even rarer packing, as shown in the middle-right panel of figure (3.1c), where the packing factor is $3\pi/(2 + \sqrt{2} + \sqrt{3})^2 \sim 0.355866$. The resulting structure, reported in the right hand side of figure (3.1d), is called within this paper “*tilene*”.

Flakene parent and flakene.

The semi-regular tiling of the plane by regular polygons with the largest rings is the truncated trihexagonal tiling reported in the middle-left panel of figure (3.1e) for which the packing factor before the geometry optimization is $\pi(2/\sqrt{3} - 1) \sim 0.486006$. The resulting geometry is called “*flakene parent*” (C_{64} graphenylene in [12, 13, 14]) and is reported in the left hand side of figure (3.1f). Its augmentation, shown in the middle-right panel of figure (3.1e), shows a tiling containing 24-sided polygons whose density is $3\sqrt{3}\pi/(20 + 3\sqrt{3} + 6\sqrt{7} + 2\sqrt{21}) \sim 0.324951$. Although topologically equivalent, this packing differs from a previously reported example [11] as its density is appreciably lower. The resulting structure, obtained by placing carbon atoms at the disc centers, is reported in the right hand side of figure (3.1f) and we call it “*flakene*”. It can be shown that it is one of the sp^2 structures with lowest density ever studied which agree to the locally-jammed packing and periodic conditions.

Beyond the regular and semi-regular tessellations: the Cairo pentagonal tiling. Liskene and liskene daughter.

Other carbon structures can be designed by using a tiling conceptually different from what we have seen so far. In particular, one may think to modify the carbon three-coordination, and to allow also four-coordinated vertices. The Cairo pentagonal tiling is known to be the planar projection of the pentagraphene structure [15] and it cannot be packed using congruent discs as the previously proposed structures. In this arrangement not all carbon atoms are three-coordinated and the resulting structure is not planar. The unit cell of pentagraphene, whose 3×3 periodic arrangement is reported in figure (3.1g), is made by 4 three-coordinated and 2 four-coordinated vertices, characterized thus by sp^2 - sp^3 and sp^2 - sp^2 hybridization, respectively. This diversity of coordination leads the system to develop into the third dimension. This reflects the fact that one cannot tile the plane by regular pentagons. Top and side views of the calculation supercell used in our simulation are reported in the left hand side of figure (3.1h). To find the daughter structure, we apply our augmentation method also to the Cairo pentagonal tiling, characterizing the pentagraphene cell. In this way, we obtain a planar three-coordinated structure that we name “*liskene*”, which is shown in the central panel of figure (3.1g). While we notice that this is a different case study with respect to the other structures, we find that the daughter architecture is still a

three-coordinated system with a density lower than the parent. In the central panel of figure (3.1h) we show the DFT optimized geometry of this tiling. Furthermore, by further augmenting the vertices not belonging to the triangular polygons of liskene, we obtain the daughter architecture (see the right panel of figure (3.1g)) which represents the maximal limit of the planar packing of pentagraphene. Finally, in the right panel of figure (3.1h) we report the DFT-optimized structure.

Relaxing the locally jammed packing constraint.

By relaxing the condition of having all the angles between two carbon bonds strictly less than π , the flakene architecture can be used as a basis for building up structures with arbitrary low density. This can be achieved by progressively elongating the sides of the hexagonal super-ring highlighted in figure (3.1i), at fixed width. In particular, a sketch of the structure derived by doubling the hexagonal super-ring sides is reported in figure (3.1l). Concerning stability, by increasing the length of the hexagonal sides to achieve an arbitrarily low density the energy-per-atom is 1.372 eV/atom higher than graphene, which can be assumed to be the asymptotic value for area density going to zero. Thus, while here we stress the fact that this work focus on all- sp^2 carbon-based geometries with low density which satisfy the locally jammed packing condition, nevertheless by relaxing this constraint one can achieve progressively low density.

3.3.2 Structural optimization

Prior carrying out the mechanical and electronic characterization of these novel carbon nets, we perform the structural optimization (details on the DFT parameters were given in section 3.2). In the second and third columns of Table 3.1 we report the energy per atom and the cohesive energies obtained upon optimization of the atomic positions within the cell.

The cohesive energy of graphene (7.74 eV) well agrees with the experimental value of 7.6 eV [16], and with previous DFT simulations [17] reporting a value of 7.828 eV. We notice that graphene is still the most energetically stable allotrope. In general, with the notable exception of pentagraphene, we observe that lowering the densities of the parent structures by using the previously introduced augmentation method results in daughter architectures characterized by lesser energetic stability and lower intra-molecular bond strengths. We rationalize the different finding in the case of pentagraphene, for which the cohesive energy increases from parent to daughter, by noticing that the augmentation starts from a non-planar $sp^2 - sp^3$ net and ends up into a purely planar sp^2 net. This atomic arrangement represents thus a favourable solution from both the energetic and density points of view.

For the flakene parent we find almost the same energy difference (0.6395 eV vs. 0.64 eV) with respect to graphene (see third column of table 3.1) as in [18], where

TABLE 3.1: First column: structure type. Second column: surface density. Third and fourth columns report the total energy per atom with respect to graphene and the cohesive energy per atom obtained upon structural optimization, respectively. With the exception of pentagraphene, all structures are planar and each carbon atom is three-coordinated. In the table the following abbreviations were used: p.=parent, d.=daughter, dir.=direct gap, indir.=indirect gap.

Structure	Density (atoms/Å ²)	Energy ([eV]/atom)	Cohesive energy ([eV]/atom)	Type	Bandgap [eV]
Graphene	0.379	0	7.7404	Semi-met.	0 (dir.)
Graphene d.	0.256	0.9882	6.7523	Metal	-
Tilene p.	0.336	0.5186	7.2219	Metal	-
Tilene	0.233	1.0765	6.6640	Metal	-
Flakene p.	0.301	0.6395	7.1009	Semi-met.	0.043 (dir.)
Flakene	0.212	1.1071	6.6334	Metal	-
Pentagraphene	0.452	0.9044	6.8361	Semicond	2.23 (ind.)
Liskene	0.297	0.7789	6.9615	Semicond	0.36 (ind.)
Liskene d.	0.247	1.0506	6.6897	Semicond	0.46 (ind.)

this structure is labelled “graphenylene”. Also for the tilene parent we calculate an energy difference with respect to graphene equal to 0.5186 eV, which is very similar to the value of 0.53 eV reported in [2], where the structure was named T-graphene. Finally, in the case of pentagraphene we find an energy-per-atom difference of 0.904 eV, which is very much comparable to the value of about 0.9 eV reported in [15].

While we notice that the loss of stability is not significant, as the total energy difference per atom between the less stable material (flakene) and graphene is of the order of 1%, the density is almost two times lower than that one of graphene (see the second column of table 3.1).

3.3.3 Phonon band structures

To test the dynamical stability of the novel structures proposed in this work we computed the phonon dispersion curves. The phonon band structures, calculated with the parameters described in section 2.3, are reported in figure (3.2) for the parent and the daughter structures, respectively. We stress that we could not find the presence of imaginary frequencies, which means that the structures are dynamically stable. Furthermore, we notice the emergence of a phononic gap in the daughter architectures above 800 cm⁻¹, which is not present in the parent structures.

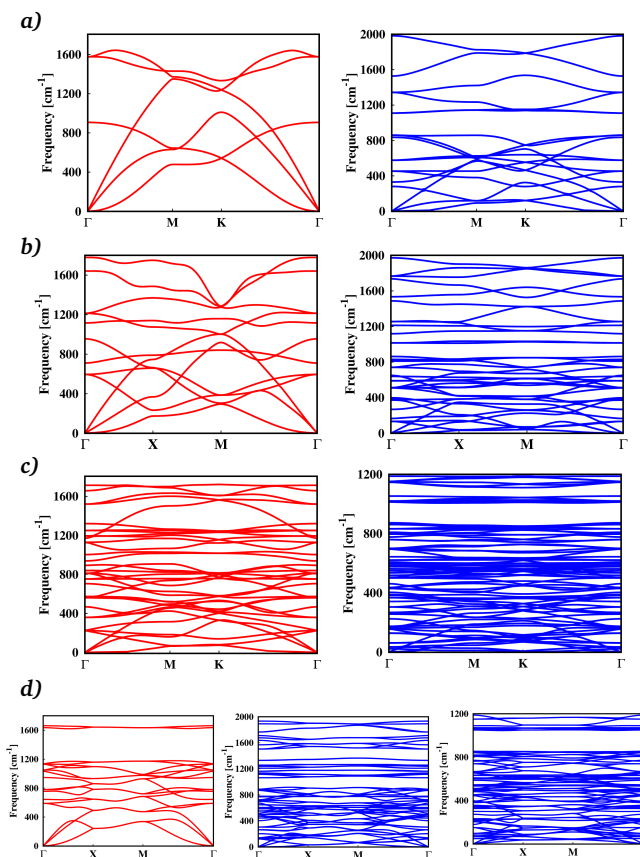


FIGURE 3.2: Phonon band structures of the parent (left panel, red lines) and daughter (right panel, blue lines) architectures of a) graphene, b) tilene, c) flakene, and d) pentagraphene.

3.3.4 Electronic properties

In this section we report the band structures and relevant DOSs for the eight structural arrangements investigated in this work.

We begin with the well known electronic band structure of graphene reported in the upper left panel of figure (3.3a) alongside the DOS (red filled curve in the lower panel of figure (3.3a)), which we reproduce to test our choice of the DFT parameters. The agreement with previous simulations [19] is excellent so we can move to the assessment of the electronic structure of the other systems.

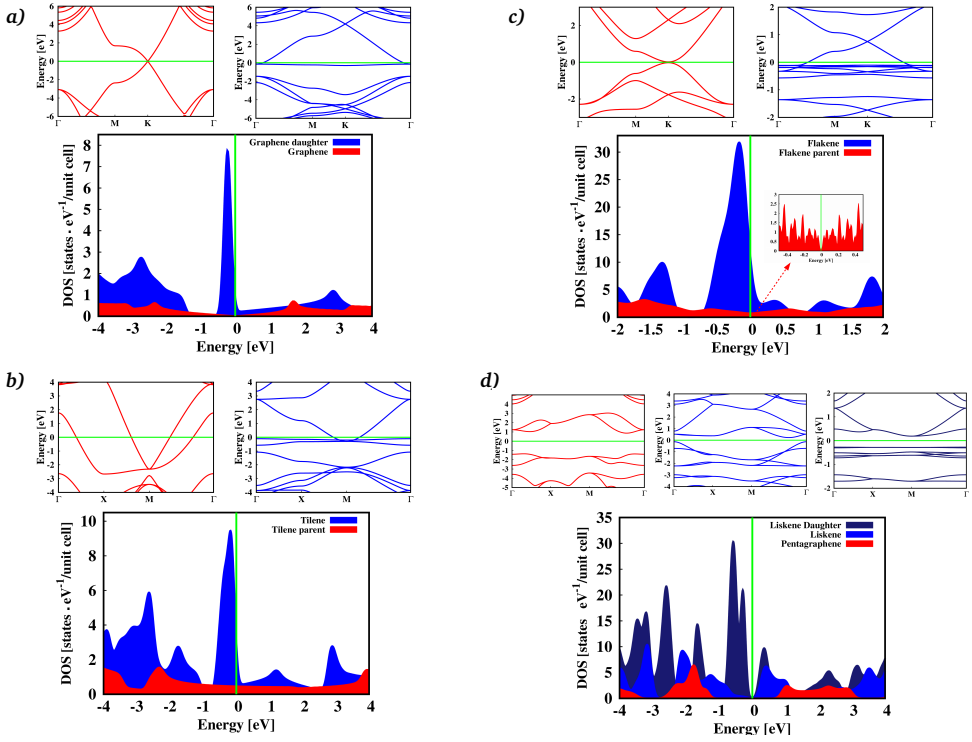


FIGURE 3.3: Upper panels: band structure of the parent (left, red lines) and daughter (right, blue lines) architectures of a) graphene, b) tilene, c) flakene, and d) pentagraphene. Lower panels: relevant DOS of the parent (red filled area) and daughter (blue filled area) structures. Fermi level is shifted to zero and reported as an horizontal (vertical) green line in the band structure (DOS).

In the right panel of figure (3.3a) we report the bands of the graphene daughter. We observe that graphene loses its semi-metal characteristics and acquires a striking metallic behaviour with a loss of the typical graphene features near the Fermi energy (valence and conduction bands do not touch in Dirac points as well as the dispersion around the Γ -point is not linear). This is due to the appearance of a narrow band close to the Fermi level (reported as an horizontal (vertical) green line in the band structure (DOS)), a feature that appears also in tilene and flakene, as can be seen in the upper right panels of figures (3.3b) and (3.3c). This is of course reflected into the DOS, characterized by a narrow peak close to the Fermi energy, as shown in the blue filled curves reported in the lower panels of figure (3.3a), (3.3b), and (3.3c).

Tilene parent and flakene parent electronic band structures (see upper left panels

TABLE 3.2: Elastic constants (C_{11} , C_{12} , C_{44}), area Young's modulus (E_A), Young's modulus (E), Poisson's ratio (ν) and area specific Young's modulus (E_A/ρ_A) of the parent and daughter carbon structures. To evaluate the accuracy of our simulations, we report a comparison with data in the literature where available. In the table the following abbreviations were used: p.=parent, d.=daughter.

	C_{11} (N/m)	C_{12} (N/m)	C_{44} (N/m)	E_A (N/m)	E (TPa)	ν	E_A/ρ_A (10^{-3} Nm kg $^{-1}$)
Graphene	348	53.8	-	340	1.14	0.154	1.79
[12]	358	60	-	349		0.17	
Graphene d.	149	94.0	-	89.6	0.30	0.631	0.70
[12]	152	98	-	92.6		0.64	
Tilene p.	294	44.1	48.3	288	0.96	0.150	1.70
[20]	296	46	49	306		0.13	
Tilene	124	75.5	11.3	78.6	0.26	0.607	0.67
Flakene p.	220	57.7	-	205	0.69	0.263	1.36
[12]	227	61	-	210		0.27	
Flakene	87.0	64.9	-	38.6	0.13	0.746	0.36
Liskene	187	94.8	52.0	138	0.46	0.508	0.93
Liskene d.	127	65.6	19.4	93.1	0.31	0.517	0.75

in figures (3.3b) and (3.3c), respectively) are not dramatically changed by augmentation, as the daughter structures stay metallic (see lower panel in figure (3.3b) for tilene daughter) or increase their metallic character (see lower panel of figure (3.3c) for flakene daughter).

At odds with the previous architectures, pentagraphene band structure (see upper left panel of figure (3.3d)), which has the typical characteristics of a semiconductor (in agreement with previous DFT calculations [15]), is heavily affected by augmentation, as the daughter structure (see upper right panel of figure (3.3d)) presents an almost semi-metallic behaviour characterized by a very narrow band gap. The relevant DOSs of pentagraphene (filled red curve of figure (3.3d)) and liskene (filled blue curve of figure (3.3d)) are typical of a semiconductor and semi-metal, respectively.

3.3.5 Elastic properties

To characterize the mechanical properties of the daughter architectures in comparison to the parent structures we carried out first the ab-initio simulations of the elastic stiffness tensor \mathbf{C} . The matrix \mathbf{C} provides in linear approximation the proportionality or elastic constants relating the stress and the strain, $\sigma = \varepsilon \mathbf{C}$ where ε is the six-component strain vector, and σ is the stress tensor. The stiffness tensor is in principle characterized by six independent terms in bi-dimensional materials, being $C_{ij} = C_{ji}$ for symmetry considerations. The elastic behaviour of orthotropic 2D materials can

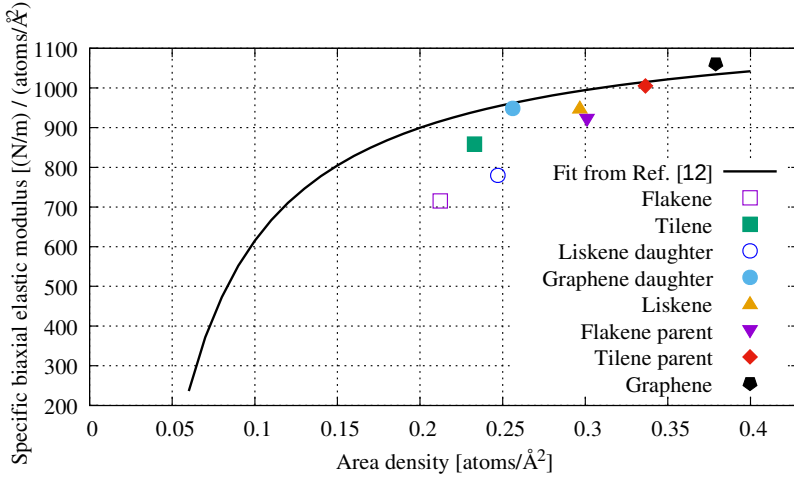


FIGURE 3.4: Specific biaxial elastic modulus versus area density. The black line shows the trend reported in [12] for carbon allotropes.

be described thus by four elastic constants C_{11} , C_{22} , C_{12} and C_{44} [21]. For the square lattice structures, such as tilene parent, tilene and liskene, the symmetry constraint sets $C_{11} = C_{22}$, so that one has only three independent elastic constants. Graphene, graphene daughter, flakene parent and flakene at variance show isotropic hexagonal symmetry, reducing the independent elastic constants to only two according to the relations $C_{11} = C_{22}$ and $2C_{44} = C_{11} - C_{12}$.

In harmonic approximation, the strain–energy density function F at 0 K can be expressed as

$$F = F_0 + \frac{1}{2}F^{(2)}\varepsilon^2 + o(\varepsilon^3) \quad (3.1)$$

where F_0 and $1/2F^{(2)}\varepsilon^2$ are the static energy of the system and the lattice vibrational contribution, respectively. In our simulations we neglect the thermal electronic contribution, which is expected to be low.

The elastic constants C_{ij} can be then expressed as follows:

$$C_{ij} = \frac{\partial^2 F}{\partial \varepsilon_i \partial \varepsilon_j} \quad (3.2)$$

The C_{ij} s can be derived by fitting the energy density of (3.1) with a second order polynomial in the imposed strain. In particular, on the one side for isotropic materials the fitting parameter $F^{(2)}$ can be identified with C_{11} for uniaxial deformation and with $2(C_{11} + C_{12})$ under hydrostatic deformation, respectively. On the other side,

in the case of orthotropic materials further calculations are needed in order to fully characterize the stiffness matrix. In this case, the elastic constants C_{11} , C_{22} can be identified as the fitting parameters of the total energy under uniaxial strain, while $F^{(2)}$ corresponds to $C_{11} + C_{22} + 2C_{12}$ or $4C_{44}$ in the case of hydrostatic deformation or shear deformation, respectively. From the knowledge of the elastic constants, the Young's modulus E , which measures material's stiffness, and the Poisson's ratio ν , which measures the material's tendency to expand in directions perpendicular to the direction of compression, can be computed as $E = (C_{11}^2 - C_{12}^2)/C_{11}$ and $\nu = C_{12}/C_{11}$, respectively.

In table (3.2) we report the elastic constants, Young's modulus and Poisson's ratio of all the 2D carbon allotropes studied in this work in comparison with the DFT values reported in the literature [12, 20], finding a remarkable agreement with previous calculations and experiments. We remind that, at variance with a stable, isotropic, linear elastic 3D material where the bounds on Poisson's ratio are $-1 < \nu < 1/2$, for 2D materials one has $-1 < \nu < 1$ [22]. Therefore, it is not surprising to obtain values of the Poisson's ratios higher than $1/2$ for our 2D architectures.

The Young's modulus of graphene obtained from our DFT simulations is in good agreement with the experimental value of 1 ± 0.1 TPa (assuming a graphene thickness equal to 0.335 nm), obtained by nanoindentation measurements on single-layer graphene [23]. The analysis of the Poisson's ratio of tilene, flakene and liskene shows that these materials are almost incompressible. More precisely, the Poisson's ratio of tilene (as of graphene daughter, flakene, and liskene) is higher than the limit of isotropic incompressible 3D materials (which is 0.5) while lower than the corresponding upper bound on Poisson's ratio for 2D materials (which is 1 [22]): this material presents a hyper-restriction correspondent to a decrease of the area under tension.

Tilene presents an area Young's modulus $E_A = 78.6$ N/m and a Poisson's ratio $\nu = 0.607$, which are similar to those of the graphene daughter. Flakene has an area Young's modulus $E_A = 38.6$ N/m and a Poisson's ratio $\nu = 0.746$. Generally, we notice that graphene has the highest Young's modulus, and that moving from parent to daughter structures the Young's modulus decreases and the Poisson's ratio consequently increases.

Moreover, one of the most significant observables to be computed for low density materials is of course the specific modulus, namely the Young's modulus divided by the mass density. Thus, we computed the Young's modulus per mass density $E_A/\rho_A = E/\rho$, where ρ_A is the density in units of Kg/m² and ρ the mass density in Kg/m³. The outcome of our simulations concerning this quantity are reported in the last column of table (3.2). We notice that graphene presents the biggest specific modulus among the materials studied here. At odds flakene, while displaying the lowest density among the investigated structures, shows a major drop in both the absolute and specific elastic moduli, which are from 8 to 5 times lower than graphene. Nevertheless, while we do not find a material outperforming the specific properties of graphene in this respect and, thus, we do observe that the augmentation is only

TABLE 3.3: Fracture strain (first column), strength (second column), strength $\times t$ (third column) and toughness $\times t$ (fourth column) of the parent and daughter planar structures alongside the specific strength and specific toughness (fifth and sixth columns). The conventional thickness of the graphenic materials is considered to be $t = 3.35 \text{ \AA}$. In the table the following abbreviations were used: p.=parent, d.=daughter.

	Loading direction	Fracture strain (%)	Strength (GPa)	Strength $\times t$ (N/m)	Toughness $\times t$ (J m^{-2})	Specific strength (MNm kg^{-1})	Specific toughness (MJ kg^{-1})
Graphene	x	> 35	112	37.5	> 9.83	49.7	> 13.0
	y	26-28	102	34.2	6.51	45.2	8.61
Graphene d.	x	18-20	29.3	9.81	0.83	19.2	1.62
	y	> 30	67.7	22.6	> 3.63	44.3	> 7.11
Tilene p.	x,y	24-26	99.6	33.4	5.55	49.7	8.27
	45°	32-34	79.1	26.5	5.68	39.5	8.47
Tilene	x,y	20-22	44.8	15.0	1.66	32.3	3.57
	45°	18-20	30.3	10.2	0.92	21.9	1.97
Flakene p.	x	22-24	66.7	22.3	3.37	37.2	5.61
	y	22-24	57.9	19.4	3.01	32.3	5.02
Flakene	x	12-14	23.6	7.92	0.49	18.7	1.16
	y	14-16	25.8	8.63	0.63	20.4	1.49
Liskene	x,y	18-20	63.2	21.2	2.19	35.8	3.70
	45°	14-16	43.8	14.7	1.27	24.7	2.14
Liskene d.	x,y	12-14	27.8	9.32	0.59	18.5	1.20
	45°	14-16	28.0	9.37	0.68	19.0	1.37

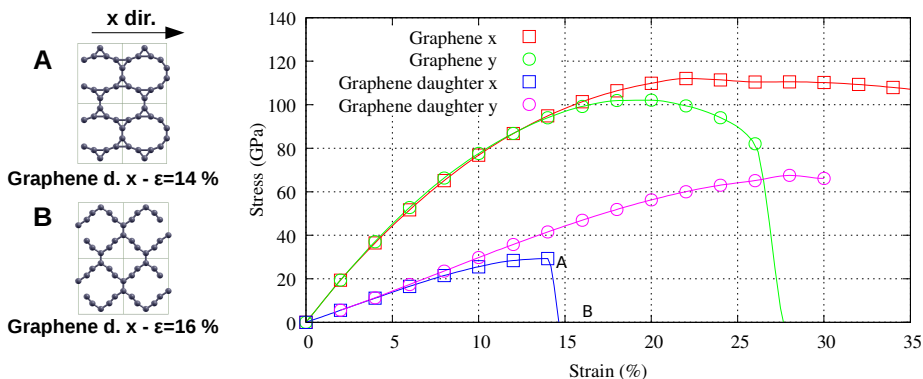


FIGURE 3.5: Stress–strain curves of graphene and graphene daughter along the x -direction (or zig-zag, represented by red and blue empty squares for the two architectures, respectively) and the y -direction (or armchair, represented by green and violet empty circles for the two architectures, respectively). The differently colored lines represent the best fits to the ab-initio data. On the left and right sides of the image we report the simulation cells of graphene daughter for different strain values and directions.

partially an advantageous route to follow in order to increase the specific modulus of graphene-like materials, the difference in the specific Young's modulus is less remarkable than for the absolute values, with the exception of flakene.

The drop of flakene Young's modulus suggests that there is a threshold to the decrease of the density of these carbon-based planar materials, below which this mechanical characteristic is significantly depleted. In order to get further insights on this issue, we report in figure (3.4) the specific modulus of our carbon allotropes versus area density. In particular, we plot the specific biaxial modulus ($E_{bi} = C_{11} + C_{22}$) versus the area density, fitting the data reported in [12] by the formula $E_{bi} = 1184.3 \times \rho_A - 56.88$ (N/m)/(atoms/Å²) (black curve in figure (3.4)). We notice that the specific biaxial modulus of the structures studied in this work can be found in close proximity to the model fit. These findings led us to the conclusion that the idea of decreasing the density, retaining the specific mechanical characteristics, can be pursued only to some extent at least as far as the Young's modulus is concerned.

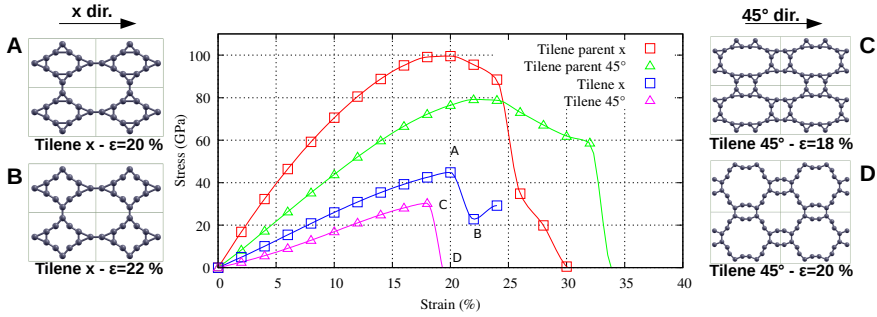


FIGURE 3.6: Stress–strain curves of tilene parent and tilene along the x -direction (red and blue empty squares for the two architectures, respectively) and the 45° -direction (green and violet empty triangles for the two architectures, respectively). The differently colored lines represent the best fits to the ab-initio data. On the left and right sides of the image we report the simulation cells of tilene for different strain values and directions.

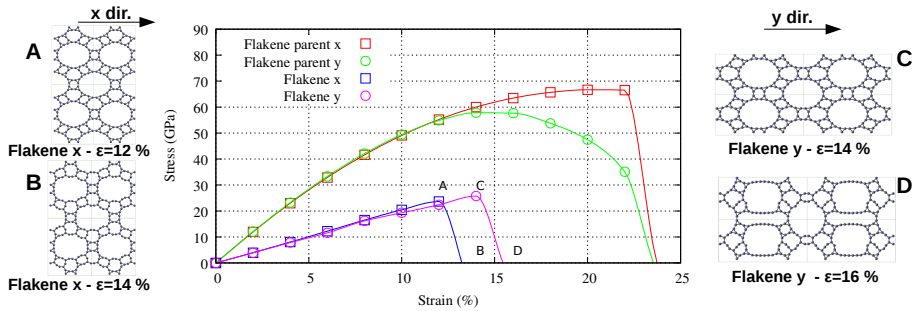


FIGURE 3.7: Stress–strain curves of flakene parent and flakene along the x -direction (red and blue empty squares for the two architectures, respectively) and the y -direction (green and violet empty circles for the two architectures, respectively). The differently colored lines represent the best fits to the ab-initio data. On the left and right sides of the image we report the simulation cells of flakene for different strain values and directions.

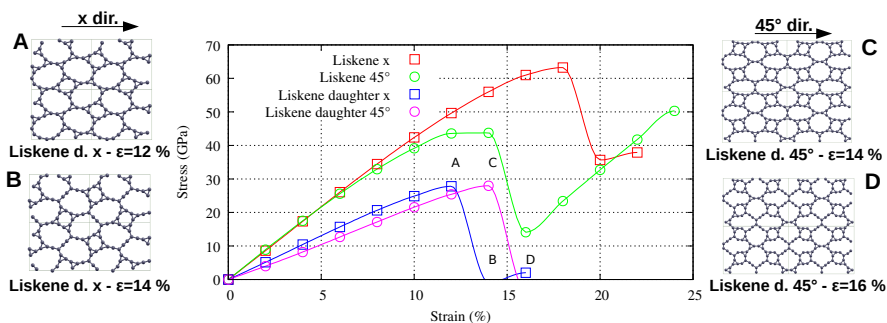


FIGURE 3.8: Stress–strain curves of liskene and liskene daughter along the x -direction (red and blue empty squares for the two architectures, respectively) and the 45° -direction (green and violet empty circles for the two architectures, respectively). The differently colored lines represent the best fits to the ab-initio data.

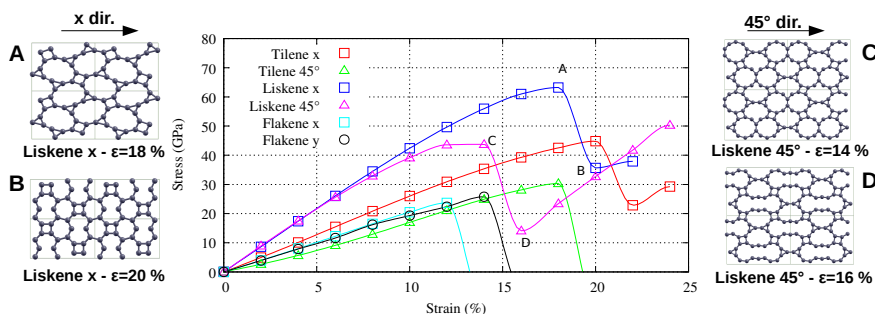


FIGURE 3.9: Comparison between the stress–strain curves of liskene, tilene, and flakene along the x -direction (blue, red and cyan empty squares for the three architectures, respectively), along the 45° -direction (violet and green triangles for liskene and tilene, respectively) and along the y -direction (black empty circles for the flakene architecture). The differently colored lines represent the best fits to the ab-initio data. On the left and right sides of the image we report the simulation cells of liskene for different strain values and directions.

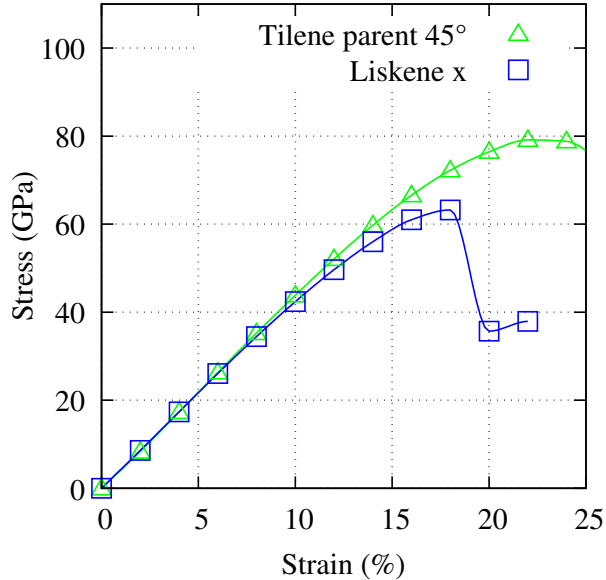


FIGURE 3.10: Comparison between the stress–strain curves of liskene (blue empty squares) and tilene (green empty triangles) parent along the x and 45° directions, respectively. The differently colored lines represent the best fits to the ab-initio data.

3.3.6 Stress–strain curves

To gain further insight on the dependence of the mechanical properties of our structures on the density, we carried out the first-principles simulations of the stress–strain curves from which several observables can be obtained, such as the fracture strain, the tensile strength and the toughness. DFT calculations of the true stress tensor in response to strain, from which one can develop constitutive equations to fit the ab-initio data, were performed on the unit cell of the materials. We remind that all structures were relaxed below 3 kbar in the direction orthogonal to loading, and we plot the stress obtained by using the relaxed surface (true stress as opposed to engineering stress).

In figure (3.5) we start from analysing the stress–strain curves of graphene and graphene daughter to benchmark our results against the extensive number of computational and theoretical studies carried out in this respect, along the Cartesian directions x, y , which represents the zig-zag and armchair directions of graphene (or,

better to say, of the zig-zag and armchair ribbon that can be obtained by cleaving along the x, y directions), respectively. The stress–strain characteristics under uniaxial tensile loading along the zigzag (x , empty red squares) and armchair (y , empty green circles) directions, reported in figure (3.5), show the known anisotropic response of graphene that results in nonlinear constitutive equations [24, 25]. The mechanical response of graphene to uniaxial tension is almost linear until about 10% strain for both the armchair and zigzag directions, with the curve slope progressively decreasing with increasing strain. Beyond that value the stress–strain curves deviate significantly from linearity, keeping the isotropic behaviour up to 15% strain, where the mechanical characteristics along the two loading directions fork. The anisotropy develops at rather moderate strain with the zig-zag stiffness dramatically decreasing with respect to the armchair direction. In figure (3.5) we sketch also the mechanical response to loading along the x (empty blue squares) and y (empty violet circles) directions of the graphene daughter. We notice that the absolute mechanical properties deplete significantly from graphene to its daughter in all respect, with a strong decrement in toughness and strengths (see also table (3.3), where we report the absolute mechanical characteristics of these structures along with those of the other novel 2D architectures proposed in this work, that is tilene, flakene and liskene). In this respect, we notice that the architecture of the graphene daughter is largely dominated by the presence of triangular shapes, at variance with graphene (see figure (3.1b)). This feature is shared also by tilene (see figure (3.1d)). This seems the major reason of the similar mechanical response to uniaxial strain along the x -direction between the graphene daughter (see violet empty circles in figure (3.5)) and tilene (see blue empty squares in figure (3.6) for a comparison). Along the y direction the mechanical response of graphene daughter is similar to graphene (see violet empty circles in figure (3.5)), showing a high fracture strain at lower stress than graphene.

Tilene parent and tilene (see figure (3.1d)) belong to the dihedral group of symmetries (D4) and, thus, in figure (3.6) we reproduced the stress–strain characteristics along the x (empty squares, a strain along the y direction would provide the same results) and the diagonal (45° , empty triangles) directions. Tilene parent displays a behavior under mechanical loading similar to graphene along the x -direction (empty red square in figure (3.6)) with comparable strength and proportional limit stress (see table (3.3)). However, in the diagonal direction (see empty green triangles in figure (3.6)) the presence of sp^2 -carbon squares reduces the absolute mechanical performances of the tilene parent, but with a significantly higher fracture point (see table (3.3)). Nevertheless, the stress–strain characteristics do not overlap along the two different directions. Tilene shows a mechanical response to uniaxial strain comparable to graphene daughter in both the x (blue empty squares of figure (3.6)) and diagonal directions (violet empty triangles of figure (3.6)), being its structure characterized by a similar occurrence of sp^2 triangles.

Furthermore, in figure (3.7) we report the stress–strain curves of flakene parent

and daughter along the orthogonal directions x (empty squares) and y (empty circles) as their lattices display hexagonal symmetry. The mechanical characteristics of flakene parent are similar to those of graphene, showing a split between x (empty red squares) and y (empty green circles) curves at about 13% strain, and an almost linear regime up to 10% strain. However, the values of the strength are 60% lower than in the case of graphene (see table (3.3)). Flakene daughter shows a behaviour comparable to graphene daughter, being characterized by a similar large presence of sp^2 -carbon triangular lattices, with lower absolute values of the strength (see table (3.3)).

We notice that the augmentation procedure to obtain the liskene daughter architecture from liskene concerns only the carbon atoms that belong to the square shapes. In figure (3.8) we report the stress–strain curves of liskene and liskene daughter along the orthogonal x -(empty squares) and 45° - directions (empty circles). Even in this case we find the general trend previously observed of a decrease of the fracture strain and tensile strength from the parent to the daughter structure.

In figure (3.9) we present the stress–strain characteristics along the x and y directions of our novel planar architecture named liskene, compared to tilene and flakene. As previously noticed, within the linear steep the uniaxial x (blue empty squares) and y (violet empty triangles) loading curves are overlapping, and at about 6% strain they fork and deviate progressively from linearity up to the fracture strain at about 14% and 18% strain, respectively. The values of liskene mechanical characteristics are slightly higher than the other proposed architectures (see table (3.3)). We notice that after the disruption of the first set of bonds at 14% and 17% strain along the x and y directions respectively (see the structures reported in the left and right hand sides of figure (3.9)), liskene stress–strain curves in both directions bounce into a second linear regime with different slope.

Finally, in figure (3.10) we notice that tilene parent (green line) and liskene (blue line) basically present comparable stress–strain curves up to 10% strain. We rationalize this by noting that for both structures the stress–strain characteristics are initially dominated by the deformation of sp^2 -carbon atom arranged in square forms. However, as the strain increases, the liskene stress–strain curve departs from that one of tilene parent. This is due to the fact that the former architecture undergoes the fracture of the bonds within the squares, and the stronger bounds of carbon triangles come into play.

As a final remark, we point out that the picture so far described concerning the absolute values slightly changes when we look at the specific properties reported in the last two columns of table (3.3). Indeed, the strength of our novel 2D structures is comparable to graphene, or even higher than the latter in the case of the tilene parent. Nevertheless, the trend of the specific toughness, which measures the ability of a material to absorb energy before fracture, is generally favourable to graphene with respect to the other structures.

3.4 Conclusions

To conclude, in this chapter we present a method for discovering all- sp^2 carbon allotropes belonging to the class of regular and semi-regular tilings, with the aim of decreasing the density of graphene without depleting its unique mechanical properties. Within this set of tessellations, our method proceeds by lowering the packing factors by increasing the number of congruent discs under the constraint of local stability. Moreover, we have shown how this approach can be also extended to deal with non-regular tilings by augmenting the Cairo pentagonal tessellation.

While all the daughter structures that we generate display lower stability and smaller cohesive energy than graphene, their density is considerably lower than graphene up to 45%. In particular, we argue that flakene represents the least dense possible structure among the families of all- sp^2 generated carbon allotropic forms starting from planar parent architectures under the local stability constraint. Nevertheless, we propose that novel geometries could be obtained by initiating the augmentation procedure from non-planar architectures, e.g. from pentagraphene. The relevant atomic arrangement derived from pentagraphene, which is named liskene, displays a high cohesive energy at a density lower than 22% with respect to graphene. In passing, we stress the point that all our sp^2 carbon structures are found dynamically stable, and do not present imaginary frequencies.

Nevertheless, by comparing the specific Young's modulus of these structures with graphene, we notice that there is a threshold below which is not possible to reduce further the density without a considerable depletion of this elastic property. In particular by lowering the density below that one of liskene results in a reduction of about 40% of the specific Young's modulus. This can be clearly seen in the case of flakene, which displays the lowest density among the proposed planar structures as well as the smallest absolute and specific Young's modulus. Thus, graphene presents one of the highest specific modulus ever found and the quest for finding a better replacement in mechanical engineering applications is still open. Based on these findings, we argue that the focus on the search for materials with high specific Young's modulus should proceed among the high-density carbon allotropes. However, the area density of graphene is close to the limit of maximal planar packing. Furthermore, the specific Young's modulus has an asymptotic limit for high density packing. We further note that the structures with atomic density in the range of 0.25 – 0.3 atoms/Å² have performances similar to that of graphene and a research focused in this range of densities could be profitable in finding high specific modulus materials. Thus, a hypothetical improvement of this quantity could be devised only by changing the paradigm of interaction, for example by enhancing electrostatic and/or van der Waals interactions.

Our analysis of the mechanical properties concerned also the stress–strain curves of these low-density materials. We find that while the absolute values of the mechanical characteristics, such as fracture strain, strength, and toughness, are generally lower than those of graphene with the exception of the tilene parent architecture,

nevertheless their specific counterparts can approach those of graphene and even surpass its specific strength for the case of tilene parent. In general, we notice that the mechanical properties deplete moving from parent to daughter architectures by lowering the packing factors. Thus, depending on the application, our structures could be used to replace graphene when weight decrease is an issue of paramount importance.

Finally, we assessed also the electronic properties of the novel structures generated by our augmentation algorithm and compared them with their relevant parent networks. We find that a change in the packing factor results in the appearance of a narrow band close to the Fermi level, a feature shared by all the parent-to-daughter augmented structures. This is particularly evident in the case of the liskene architecture, which is a semi-metal, despite the parent structure of pentagraphene is a semiconductor with a 2.3 eV band gap according to our DFT simulations.

Generally, we notice that the approach presented in this work could be extended also to design novel lightweight strong one-dimensional and three-dimensional carbon allotropes [26]. This is the case for example of carbon nanotubes, which are graphitic sheets rolled along given directions in the plane in hollow cylinders with walls made by hexagonal carbon rings. In this regard, our method can be straightforwardly applied also to 1D structures. Moreover, the very same method can be used also to augment 0D structures, such as fullerenes. Extensions to treat the three-dimensional case are on-going.

Bibliography

- [1] P. Giannozzi, S. Baroni, N. Bonini, M. Calandra, R. Car, C. Cavazzoni, D. Ceresoli, G. L. Chiarotti, M. Cococcioni, I. Dabo, A. D. Corso, S. de Gironcoli, S. Fabris, G. Fratesi, R. Gebauer, U. Gerstmann, C. Gougoussis, A. Kokalj, M. Lazzeri, L. Martin-Samos, N. Marzari, F. Mauri, R. Mazzarello, S. Paolini, A. Pasquarello, L. Paulatto, C. Sbraccia, S. Scandolo, G. Sclauzero, A. P. Seitsonen, A. Smogunov, P. Umari, R. M. Wentzcovitch, Quantum espresso: a modular and open-source software project for quantum simulations of materials, *Journal of Physics: Condensed Matter* 21 (39) (2009) 395502.
URL <http://stacks.iop.org/0953-8984/21/i=39/a=395502>
- [2] Y. Liu, G. Wang, Q. Huang, L. Guo, X. Chen, Structural and electronic properties of *t* graphene: A two-dimensional carbon allotrope with tetrarings, *Phys. Rev. Lett.* 108 (2012) 225505. doi:10.1103/PhysRevLett.108.225505.
URL <https://link.aps.org/doi/10.1103/PhysRevLett.108.225505>
- [3] L.-C. Xu, R.-Z. Wang, M.-S. Miao, X.-L. Wei, Y.-P. Chen, H. Yan, W.-M. Lau, L.-M. Liu, Y.-M. Ma, Two dimensional dirac carbon allotropes from graphene,

- Nanoscale 6 (2014) 1113–1118. doi:10.1039/C3NR04463G.
URL <http://dx.doi.org/10.1039/C3NR04463G>
- [4] H. Huang, W. Duan, Z. Liu, The existence/absence of dirac cones in graphynes, *New Journal of Physics* 15 (2) (2013) 023004.
URL <http://stacks.iop.org/1367-2630/15/i=2/a=023004>
- [5] S. Taioli, R. Gabbrielli, S. Simonucci, N. M. Pugno, A. Iorio, Lobachevsky crystallography made real through carbon pseudospheres, *Journal of Physics: Condensed Matter* 28 (13) (2016) 13LT01.
URL <http://stacks.iop.org/0953-8984/28/i=13/a=13LT01>
- [6] S. Torquato, F. H. Stillinger, Jammed hard-particle packings: From kepler to bernal and beyond, *Rev. Mod. Phys.* 82 (2010) 2633–2672. doi:10.1103/RevModPhys.82.2633.
URL <https://link.aps.org/doi/10.1103/RevModPhys.82.2633>
- [7] J. L. Lagrange, *Recherches d'arithmétique*, *Nouv. Mém. Acad. Roy. Soc. Belles Lettres* (1773) pp. 265–312.
- [8] A. Thue, Über die dichteste zusammenstellung von kongruenten kreisen in einer ebene, *Norske Vid. Selsk. Skr* (No. 1) (1910) 1 – 9.
- [9] L. F. Tóth, Über die dichteste kugellagerung, *Math* 48 (1943) 676.
- [10] K. Böröczky, Über stabile kreis und kugelsysteme, *Ann. Univ. Sci. Budapest Eötvös Sect. Math* (7) (1964) 79.
- [11] W. Fischer, E. Koch, Homogeneous sphere packings with triclinic symmetry, *Acta Crystallographica Section A* 58 (6) (2002) 509–513. doi:10.1107/S0108767302011443.
URL <https://doi.org/10.1107/S0108767302011443>
- [12] H. Sun, S. Mukherjee, M. Daly, A. Krishnan, M. H. Karigerasi, C. V. Singh, New insights into the structure-nonlinear mechanical property relations for graphene allotropes, *Carbon* 110 (2016) 443 – 457. doi:<https://doi.org/10.1016/j.carbon.2016.09.018>.
URL <http://www.sciencedirect.com/science/article/pii/S0008622316307692>
- [13] G. Brunetto, P. A. S. Autreto, L. D. Machado, B. I. Santos, R. P. B. dos Santos, D. S. Galvao, Nonzero gap two-dimensional carbon allotrope from porous graphene, *The Journal of Physical Chemistry C* 116 (23) (2012) 12810–12813. arXiv:<https://doi.org/10.1021/jp211300n>, doi:10.1021/jp211300n.
URL <https://doi.org/10.1021/jp211300n>

- [14] E. Perim, R. Paupitz, P. A. S. Autreto, D. S. Galvao, Inorganic graphenylene: A porous two-dimensional material with tunable band gap, *The Journal of Physical Chemistry C* 118 (41) (2014) 23670–23674. arXiv:<https://doi.org/10.1021/jp502119y>, doi:10.1021/jp502119y.
URL <https://doi.org/10.1021/jp502119y>
- [15] S. Zhang, J. Zhou, Q. Wang, X. Chen, Y. Kawazoe, P. Jena, Penta-graphene: A new carbon allotrope, *Proceedings of the National Academy of Sciences* 112 (8) (2015) 2372–2377. arXiv:<http://www.pnas.org/content/112/8/2372.full.pdf>, doi:10.1073/pnas.1416591112.
URL <http://www.pnas.org/content/112/8/2372>
- [16] Y. J. Dappe, R. Oszwaldowski, P. Pou, J. Ortega, R. Pérez, F. Flores, Local-orbital occupancy formulation of density functional theory: Application to si, c, and graphene, *Phys. Rev. B* 73 (2006) 235124. doi:10.1103/PhysRevB.73.235124.
URL <https://link.aps.org/doi/10.1103/PhysRevB.73.235124>
- [17] I. A. Pasti, A. Jovanovic, A. S. Dobrota, S. V. Mentus, B. Johansson, N. V. Skorodumova, Atomic adsorption on pristine graphene along the periodic table of elements – from pbe to non-local functionals, *Applied Surface Science* 436 (2018) 433 – 440. doi:<https://doi.org/10.1016/j.apsusc.2017.12.046>.
URL <http://www.sciencedirect.com/science/article/pii/S0169433217336334>
- [18] Q. Song, B. Wang, K. Deng, X. Feng, M. Wagner, J. D. Gale, K. Müllen, L. Zhi, Graphenylene, a unique two-dimensional carbon network with nondelocalized cyclohexatriene units, *J. Mater. Chem. C* 1 (2013) 38 – 41. doi:10.1039/C2TC00006G.
URL <http://dx.doi.org/10.1039/C2TC00006G>
- [19] A. H. Castro Neto, F. Guinea, N. M. R. Peres, K. S. Novoselov, A. K. Geim, The electronic properties of graphene, *Rev. Mod. Phys.* 81 (2009) 109–162. doi:10.1103/RevModPhys.81.109.
URL <https://link.aps.org/doi/10.1103/RevModPhys.81.109>
- [20] X.-L. Sheng, H.-J. Cui, F. Ye, Q.-B. Yan, Q.-R. Zheng, G. Su, Octagraphene as a versatile carbon atomic sheet for novel nanotubes, unconventional fullerenes, and hydrogen storage, *Journal of Applied Physics* 112 (7) (2012) 074315. arXiv:<https://doi.org/10.1063/1.4757410>, doi:10.1063/1.4757410.
URL <https://doi.org/10.1063/1.4757410>
- [21] H. Huntington, *The elastic constants of crystals*, Vol. 7 of *Solid State Physics*, Academic Press, 1958, pp. 213 – 351. doi:[https://doi.org/10.1016/S0081-1947\(08\)60553-6](https://doi.org/10.1016/S0081-1947(08)60553-6).

- URL <http://www.sciencedirect.com/science/article/pii/S0081194708605536>
- [22] F. Thorpe, I. Jasiuk, New results in the theory of elasticity for two-dimensional composites, *Proceedings of the Royal Society of London A: Mathematical, Physical and Engineering Sciences* 438 (1904) (1992) 531–544. arXiv:<http://rspa.royalsocietypublishing.org/content/438/1904/531.full.pdf>, doi:10.1098/rspa.1992.0124.
URL <http://rspa.royalsocietypublishing.org/content/438/1904/531>
- [23] C. Lee, X. Wei, J. W. Kysar, J. Hone, Measurement of the elastic properties and intrinsic strength of monolayer graphene, *Science* 321 (5887) (2008) 385–388. arXiv:<http://science.sciencemag.org/content/321/5887/385.full.pdf>, doi:10.1126/science.1157996.
URL <http://science.sciencemag.org/content/321/5887/385>
- [24] M. Xu, J. T. Paci, J. Oswald, T. Belytschko, A constitutive equation for graphene based on density functional theory, *International Journal of Solids and Structures* 49 (18) (2012) 2582 – 2589. doi:<https://doi.org/10.1016/j.ijsolstr.2012.05.019>.
URL <http://www.sciencedirect.com/science/article/pii/S0020768312002296>
- [25] B. Hajgato, S. Gryyel, Y. Dauphin, J.-M. Blairon, H. E. Miltner, G. Van Lier, F. De Proft, P. Geerlings, Theoretical investigation of the intrinsic mechanical properties of single- and double-layer graphene, *The Journal of Physical Chemistry C* 116 (42) (2012) 22608–22618. arXiv:<https://doi.org/10.1021/jp307469u>, doi:10.1021/jp307469u.
URL <https://doi.org/10.1021/jp307469u>
- [26] Z. Qin, G. S. Jung, M. J. Kang, M. J. Buehler, The mechanics and design of a lightweight three-dimensional graphene assembly, *Science Advances* 3:e16015361 (1) (2017) 1–8. arXiv:<http://advances.sciencemag.org/content/3/1/e1601536.full.pdf>, doi:10.1126/sciadv.1601536.
URL <http://advances.sciencemag.org/content/3/1/e1601536>

Chapter 4

A theoretical model of SiC/SiO_x core/shell nanowire

In this chapter we propose a realistic model of SiC/SiO_x core/shell nanowire (NW) using a combined first-principles and experimental approach. In particular, we present a multiscale method, including molecular dynamics [1], density functional tight-binding [2] and density functional [3] simulations, for creating this novel NW structure, which was eventually synthesised by a low-cost carbothermal method. Moreover, we present ab-initio calculations, using both DFTB and DFT simulations, of the electronic structure of hydrogenated SiC and SiC/SiO_x core/shell NWs, studying the modification induced by several different substitutional defects and impurities into both the surface and the interfacial region between the SiC core and the SiO_x shell. The NW chemical-physical analysis is accomplished by recording and simulating X-ray absorption near-edge spectra. In this case the number of atoms in the unit cell is significantly bigger than those in the systems discussed in the previous chapters, due to the lower level of periodicity only along the tube axis.

We notice that in this one and in the next chapter the DOS that will be reported are given in arbitrary units, as we are interested only to the shapes and to the relative contributions to the TDOS (by different orbitals in the case of PDOS and by different atoms in the case of LDOS).

4.1 State of the art and aim of the work

The synthesis of 1D SiC structures has attracted great interest due to the possibility of combining the material unique physical/chemical characteristics with low dimensionality [4, 5, 6]. The carbide mechanical properties are enhanced in NWs, showing super-plasticity at low temperature [7] and higher strength so that they can be used

for toughening composites materials [8]. Furthermore, SiC nanowires show efficient electromagnetic wave absorption, [9, 10] and their electronic properties have been exploited to realize field effect transistors [11] and efficient field emission sources [12]. One common feature of Si-based NWs, regardless of the growth technique, is the presence of an amorphous silicon oxide (SiO_x) external layer coating the nanostructure [6]. By tuning the oxide layer thickness with respect to the SiC NW diameter in a core/shell architecture [13, 14, 15] one can modify both the electron emission [16, 17] and the optical [14, 18, 19] properties of these systems. In addition, the SiO_x layer offers facile strategies to anchor organic molecules on the NWs' surface by chemical methods, paving the way for applications of functionalized SiC/SiO_x core/shell NWs in several fields, such as protective coatings, [20] biosensing [21] or as hybrid nanosystems for biomedical applications [22].

In this regard, it has been shown that SiC/SiO_x core/shell NWs coated with light-absorbing organic molecules (so-called photosensitizers) can be efficiently applied in anti-cancer therapy using X-ray excitation [22], since the energy absorbed by the X-ray excited inorganic NWs can be efficiently transferred to the photosensitizer that generates highly reactive oxygen species, which in turn have cytotoxic effects [23].

To exploit the intriguing and remarkable features offered by SiC/SiO_x core/shell architectures, one must characterize accurately their chemical-physical properties, in particular by investigating both the SiO_x outer shell and the SiC/SiO_x buried interface, typically populated by defects, e.g. carbonaceous contaminants, oxycarbides related to the carbide oxidation process [24], and oxide impurities that can dramatically modify and deteriorate the electrical properties of electronic and optoelectronic devices [25, 26]. In this respect, a variety of experimental techniques have been routinely used to determine structural and also chemical properties of the SiC/SiO₂ interface, such as transmission electron microscopy (TEM) [27], photoemission electron spectroscopy (PES) [28, 29, 30] and X-ray absorption near-edge spectroscopy (XANES) [31, 32]. The latter, in particular, revealed to be a powerful tool for investigating nanostructured materials and inner interfaces [33, 34]. However, state-of-the-art computational investigations are limited to the crystalline phases of SiC nanowires [35, 36, 37, 38, 39], while the SiC/SiO_x interface is modeled only in the case of geometries as slabs or nanodots [40, 41]. Furthermore, these models are not enough accurate and realistic for shedding light on the many electronic and structural information enclosed in XANES spectra, and to explain the absorption peak lineshape of several transitions arising from these structures. In order to obtain a reliable picture for linking structural features to absorption peaks, a full atomistic model of SiC/SiO_x core/shell NWs, including adventitious carbon, defects and contaminants still must be developed.

In this work, we thus analyse first the structural arrangements and composition of SiC/SiO_x core/shell NWs using multiscale modeling; second, we investigate the electronic and optical properties of these nanostructures characterized by various defects and impurities by comparing ab-initio simulations of absorption spectra (XANES)

with recorded experimental data on in-house grown NWs to characterize these systems and eventually validate our computational model. This analysis led us to devise a realistic model of SiC/SiO_x core/shell NWs that includes the interface region between the two different materials, that is the amorphous SiO_x shell and the SiC core nanowire. The synergic use of computational and experimental tools delivers a comprehensive and more accurate chemical-physical description of SiC/SiO_x core/shell NWs, paving the way towards their use in power electronics, nanomedicine, and many other applications requiring high endurance.

4.2 Experimental details

The SiC/SiO_x core/shell NWs were grown via a bottom-up carbothermal method, based on the reaction between carbon monoxide and the native oxide on (001) Si substrates, using iron oxide as a catalyst [18, 13]. The core/shell structure of a single NW with diameter of ~ 60 nm is represented in Fig. (4.7a), reporting the TEM axial and cross-sectional views. As a reference for the SiC/SiO_x interface (SiC core NWs without shell), the SiO_x was fully removed from the as-grown NWs by etching the substrates in hydrofluoric acid (HF) (1 : 3) aqueous solution for an extended period of 60 min. NWs without SiC core (denoted as SiO_x NWs) were grown by omitting the carbon monoxide precursor and are used as a reference for SiO₂.

Synchrotron measurements were performed at the BEAR beamline (BL8.1L) of the ELETTRA synchrotron facility (Italy) and at the Spherical Grating Monochromator (SGM) beamline of the Canadian Light Source, University of Saskatchewan (Canada). The BEAR beamline provides a photon energy range of 3 – 1600 eV with a resolution of $E / \Delta E \sim 3000$ and an incident photon flux (i.f.) of $\sim 1 \times 10^9$ photons/s for C K-edge studies, whereas the SGM beamline provides a photon energy range of 250 – 2000 eV with the resolution of $E/\Delta E \sim 5000$ for Si K-edge (i.f. $\sim 1 \times 10^{11}$ photons/s) and O K-edge (i.f. $\sim 1 \times 10^{12}$ photons/s) measurements. XANES spectra were collected from all three types of NWs, i.e., as-grown SiC/SiO_x core/shell, SiO_x and HF-etched SiC NW ensembles that were maintained on the planar substrates.

The spectra were collected in total electron yield (TEY) mode (i.e., drain current mode) in the energy range 270 – 320 eV, 510 – 570 eV and 1830 – 1880 eV corresponding to the C, O and Si K-edge, respectively. XANES data were normalized to the corresponding spectrum acquired on a photodiode at the end of the beamline. The energy scale of each single spectrum was re-calibrated taking into account the energy fluctuations of characteristic absorption features measured on the refocusing mirror and Au mesh, respectively.

4.3 Computational details

4.3.1 Modeling of SiC and SiC/SiO_x core/shell NWs

The steps performed to obtain a fully realistic model of SiC/SiO_x core/shell NWs, similar to the typical structure shown in Fig. (4.7a), are the following: generation of the pristine SiC NW core, passivation of the SiC NW surface with different chemical elements, and creation of the SiO_x outer shell by embedding the SiC core.

These three steps are described one by one in the following sections.

Structure of the SiC core

The SiC nanowires (NWs) were obtained by cleaving a cylinder out of a 3C-SiC supercell along the [111] direction, which represents the growth axis in our synthesis process. In particular, using a cubic cell with lattice parameter $a = 4.348 \text{ \AA}$ for the 3C-SiC crystal structure, one obtains a simulation supercell for the NW with an axial periodicity of $a\sqrt{3} = 7.5309 \text{ \AA}$. The z direction identifies the cylindrical symmetry axis of the NW (the cylindrical symmetry is removed by molecular adsorption). The size of the calculation supercell was chosen equal to 50 \AA in the transverse direction, that is large enough to avoid spurious interactions between periodic images, even in the case of the NWs with the largest diameter (26 \AA). Pristine SiC NWs are forcefully characterized by the presence of contaminants at the surface. The latter dramatically modify the electronic and optical properties of these nanosystems [42, 43]. In the following section we thus thoroughly assess these effects.

Surface passivation of the SiC core

Surface-related states have a large impact in systems at nanoscale and appear usually as intra-gap states [37]. In particular, the terminations of the dangling bonds present on the SiC NW surface can affect dramatically the electronic structure and, thus, must be carefully investigated.

To perform the analysis of possible surface contaminants, we have saturated the dangling bonds of C and Si superficial atomic centers by using different atomic species and chemical compounds, notably $-H$ atoms and hydroxyl groups ($-OH$). Indeed, oxidized OH-SiC NWs can help our understanding of the SiC core/SiO_x shell interface in the HF-etched SiC NW samples, which consists of a thin layer of silicon oxycarbides [18].

The optimized configurations of these saturated NWs were obtained by using the Self-Consistent Charge Density Functional Tight Binding (SCC-DFTB) approach, implemented in the DFTB+ code suite [2]. To perform the DFTB structural and electronic relaxations we used the Slater-Koster parameter set *matsci-0-3* [44] and we included the d -orbitals in the local basis set of the silicon atoms, which are essential to achieve accurate band gap and band structure. Electronic structure simulations were carried

Radius (nm)	Band Gap (eV)	
	$-H$ sat.	$-OH$ sat.
0.6	3.30	2.55
0.9	2.79	2.10
1.3	2.52	2.05

TABLE 4.1: Band gap of the SiC core NW terminated with $-H$ atoms or $-OH$ radicals as computed by DFTB.

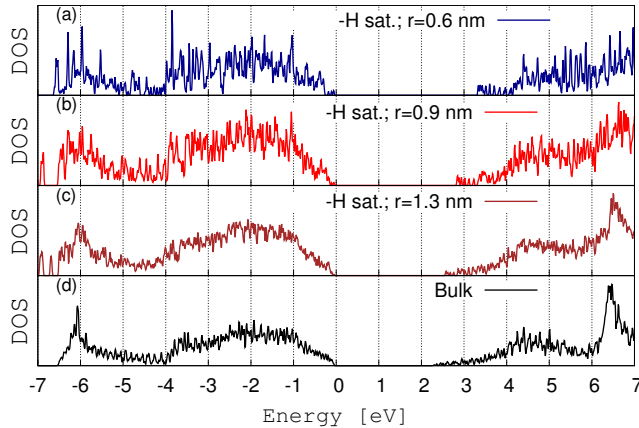


FIGURE 4.1: Total DOS of the three different diameter (d) SiC core NWs saturated by $-H$ atoms: a) $d=1.2$ nm; b) $d=1.8$ nm; c) $d=2.6$ nm; d) bulk system

out in the unit cell using a $1 \times 1 \times 4$ k -point grid sampling. Forces among all atoms within the supercell are relaxed below 0.05 eV/Å.

In agreement with previous ab-initio studies [37], we find that the $-OH$ termination is stable at the surface of the NW. This configuration is more stable than that one with unsaturated oxygen atoms; moreover, $-OH$ impurities are preferentially anchored to the Si atom at the surface, presenting formation energies of 1.76 and 3.82 eV for the C–OH and Si–OH configuration, respectively [37].

In the case of $-H$ passivation the band gap decreases by increasing the size of the radius, and tends asymptotically to the bulk value, which from our calculations is 2.3 eV (experimentally the band-gap of crystalline 3C-SiC is 2.36 eV [45]). Results of Density of States, by which we deduce the band gap, for $-H$ passivation with Fermi level set to 0 eV are reported to Fig. (4.1).

We notice that the band gap for a 1.2 nm diameter NW is 3.3 eV (see Tab. (4.1)).

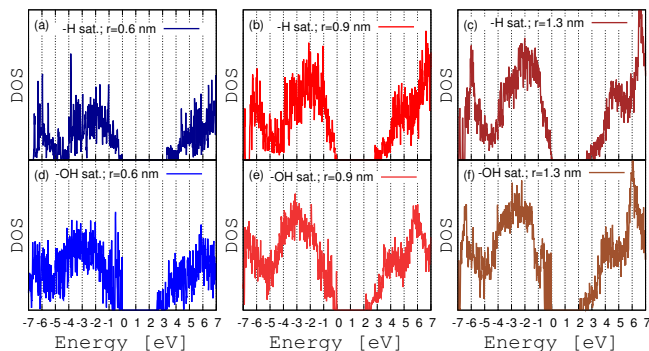


FIGURE 4.2: Comparison of the total DOS between $d=1.2$ nm (a,d), $d=1.8$ nm (b,e), and $d=2.6$ nm (c,f) SiC core NWs, saturated by H atoms (a,b,c) and by $-OH$ groups (d,e,f).

This value is rather different from the one obtained by using the full density functional (DFT) approach, which is 2.7 eV, in agreement with previous DFT simulations [37, 38]. Nevertheless, this difference is consistent with the value of the 3C-SiC Γ point energy gap (which is larger than the fundamental band gap) found to be 1.41 eV from full DFT calculations. DFTB band-gap (2.3 eV), possibly because of the Slater-Koster parametrization, is very much close to the measured band gap (2.36 eV) with respect to that obtained by DFT. These findings make us confident that DFTB can be safely used to describe the chemical-physics of the SiC NWs. By passivating the superficial dangling bonds of the SiC NW with $-OH$ we find a similar behaviour of the band gap, monotonically and asymptotically decreasing with the increasing diameter (see Tab. (4.1) and Fig. (4.2)).

The major finding of our electronic band structure simulations, in Fig. (4.3) is that both H-SiC and OH-SiC NWs turn into a direct band-gap semiconductor, with the minimum distance between the valence band maximum (VBM) and the conduction band minimum (CBM) at the Γ point. This change is basically due to electron quantum confinement obtained by reducing the system dimensionality from 3D to 1D.

Nevertheless, the band-gap calculated for the two terminations is rather different at the same radius (see Tab. (4.1)), that is consistently lower in the case of $-OH$ termination.

This difference can be rationalized in terms of both chemical termination and quantum confinement. Indeed, these two effects compete with each other and affect the electronic behaviour of the nanosystem. Quantum confinement tends to increase the band gap and largely influences systems mostly at the nanoscale, as asymptotically the band gap must match the bulk value of 3C-SiC almost independently of the surface termination. At small radius, we find that the Mulliken charge distribution of the atoms close to the surface is rather homogeneous in the case of $-H$ termination,

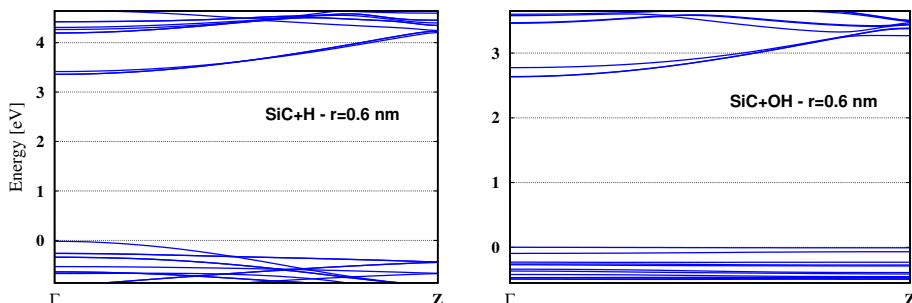


FIGURE 4.3: Band structure of SiC core NWs with diameter equal to 1.2 nm for $-H$ (left) and $-OH$ (right) terminations.

while using $-OH$ passivation the superficial atoms are partially deprived of their charge due to the high electronegativity of oxygen atoms. Thus, surface states are more likely to appear and to affect more significantly the $-OH$ terminated SiC NW, reducing the band gap with respect to the $-H$ passivated NW. Furthermore, we find that the band gap of the oxidized OH-SiC NWs is free from defective states and that the OH-SiC NWs are non-magnetic systems.

To reinforce our conclusions on the effects induced by different passivations of the NW surface, drawn on the basis of the Mulliken charge population analysis, we notice that also the calculation of the HOMO and LUMO probability densities (square modulus of the wavefunctions) of the H-SiC and OH-SiC NWs may shed some light on the chemical-physical modifications leading to the measured XANES spectral line shape. Thus in Figs. (4.4) and (4.5) we plot the VBM and CBM real-space probability densities for the smallest radius NW. In particular, we notice that in the case of $-H$ terminated NWs both the VBM (left hand side of Fig. (4.4)) and the CBM (left hand side of Fig. (4.5)) are localized in the core of the NW, while in the case of $-OH$ termination the VBM (left hand side of Fig. (4.4)) is localized on the oxygen atoms and the CBM (right hand side of Fig. (4.5)) remains mostly core-localized. This different spatial distribution of the CBM and VBM can be attributed to the strong electronegativity of the oxygen atomic species.

In the following simulations we decided to use the 0.6 nm radius SiC NW, due to the high computational cost for treating larger wires. Furthermore, due to the fact that XANES is a probe of the local environment, we expect that this model system is sufficient to reproduce accurately XANES experimental data.

SiC/SiO_x core/shell nanowire

The amorphous SiO_x outer shell was built above the 0.6 nm radius SiC core by using molecular dynamics (MD) with reactive potentials (ReaxFF [46]). In particular, the

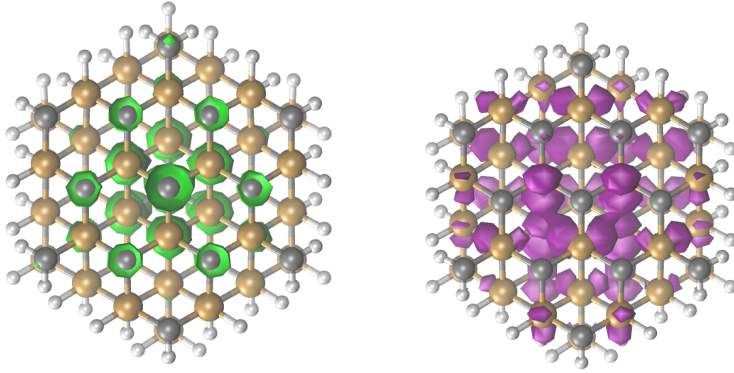


FIGURE 4.4: Left) Square modulus of the wave function of the VBM. Right) Square modulus of the CBM wave function. The plots are both referred to the 1.2 nm diameter –H-terminated SiC NW.

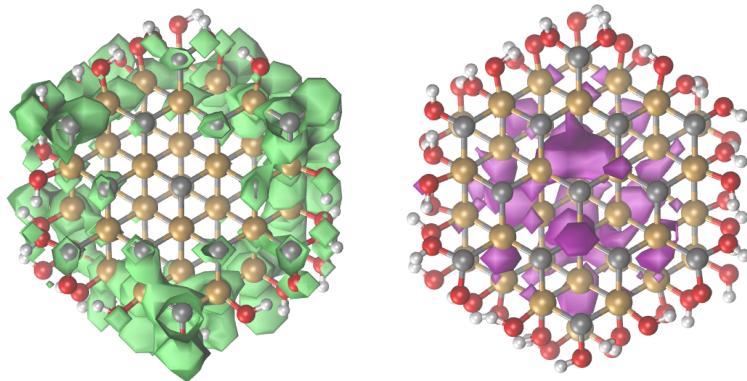


FIGURE 4.5: Left) Square modulus of the wave function of the VBM. Right) Square modulus of the CBM wave function. The plots are both referred to the 1.2 nm diameter –OH terminated SiC NW.

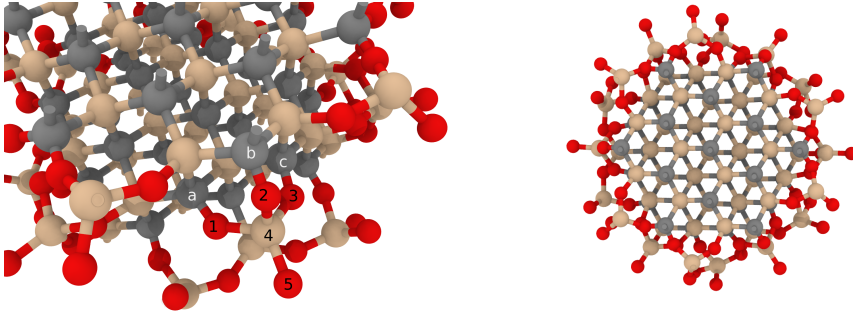


FIGURE 4.6: Interfacial bond density reduction procedure. Left panel: our strategy to reduce progressively the number of SiC core surface bonds to that of silica shell can be divided into three steps. First, we saturate all the surface dangling bonds (for example those of atoms indicated by a and c) by oxygen atoms (labeled 1,2,3). Second, a silicon atom (labeled 4) was placed in the proximity of these oxygen atoms in such a way to be three-coordinated. Finally, a further oxygen atom (labeled 5) was bound to silicon. Right panel: a transverse view of the NW core showing the bonds at interface.

parametrization of the forces has been chosen [47] to reproduce SiO_x and SiC structures at different stoichiometry. To perform these simulations we used the LAMMPS code [1].

The interface between SiC and SiO_x was created by saturating the C and Si dangling bonds protruding from the surface of the SiC NW core with oxygen atoms, and by adding Si–O groups in order to have Si tetrahedrally coordinated with oxygen atoms, as shown in Fig. (4.6).

In this way the number of bonds at the interface is decreased by a factor 2.3 to better match the density of stoichiometric SiO_2 . As a further step, the silica outer shell was created on the top of the interfacial region by using molecular dynamics. This procedure was accomplished by defining a 3 nm side periodic tetragonal cell surrounding the SiC core and the interface. Moreover, silicon and oxygen atoms were added to the simulation cell in 1:2 stoichiometric ratio to reach a density of 2.20 g/cm^3 . SiC and interfacial atomic regions were clamped down while annealing the outer SiO_x shell at 4000 K for 100 ps. Subsequently the temperature was decreased to 10.0 K in 100 ps (using 1 fs timesteps). In the last step of our procedure both the SiC core and the interfacial regions were released and the NW structure was further optimized by DFTB to reach forces among atoms below 0.05 eV/\AA .

Finally, the SiC/ SiO_x NW was obtained by deleting all the atoms that are distant from the wire symmetry axis more than the desired radius. Dangling bonds at the shell

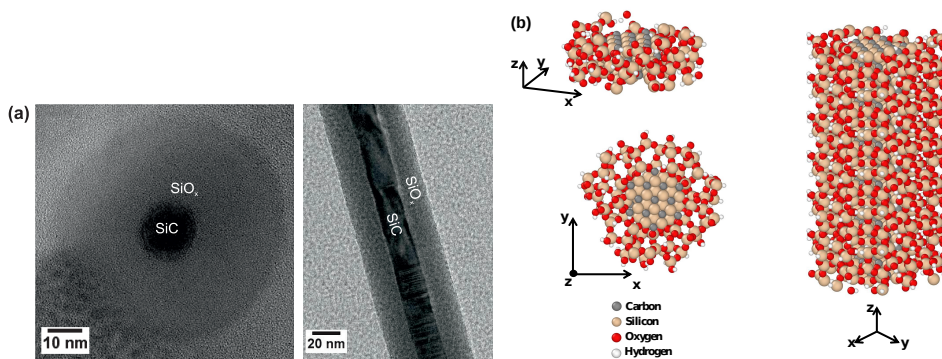


FIGURE 4.7: (a) TEM images adapted from Refs. [48, 18] of a SiC/SiO_x core/shell NW in axial view (left panel) and cross-sectional view (right panel). b) Computational model of a single SiC/SiO_x core/shell NW; left panel shows the NW unit cell side view (upper part) and top view (lower panel); right panel shows a side view of the NW supercell obtained by periodically repeating the unit cell along the rotational symmetry axis direction.

surface and some other possibly left within the NW, were passivated by hydrogen atoms.

The final structure of the model SiC/SiO_x core/shell NW, reported in Fig. (4.7b), has been further characterized with respect to bond lengths and relative angle distributions.

Characterization of bond lengths and angles of the SiC/SiO_x core/shell NW model

Geometry characterization of the SiC/SiO_x core/shell NW model was achieved by computing the following quantities:

1. the bond length of Si-O bonds (SiC core keeps its crystalline structure)
2. the bond angles forming O-Si-O atoms

In the left hand side of Fig. (4.8) we plot the distribution of a given radial distance between Si and O atoms; on the right hand side the O-Si-O angles in the same sample. The peaks compare well with those of silica [49, 50, 51].

4.3.2 Electronic structure simulations of the SiC/SiO_x core/shell nanowire

The SiC/SiO_x core/shell NW model has been characterized by computing the electronic band structure and the DOS using SCC-DFTB. In Fig. (4.9a) we report both the

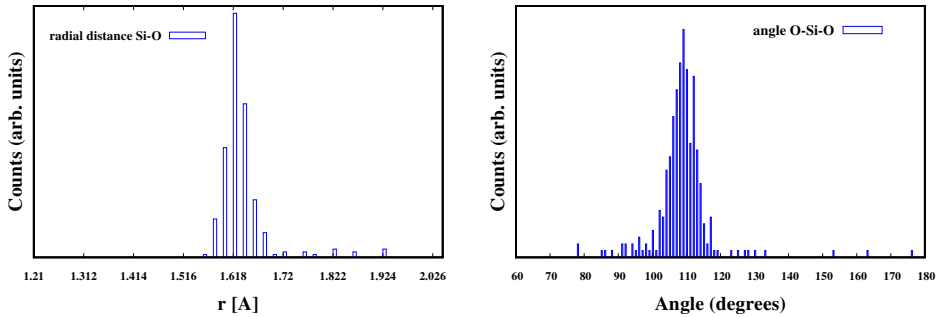


FIGURE 4.8: Characterization of SiO_x sample: on the left hand side we plot the distribution of a given radial distance between Si and O atoms; on the right hand side the O-Si-O angles

total DOS and the local DOS (LDOS) obtained by projecting onto the atoms belonging to different radial shells, which are represented in dark brown in Fig. (4.9b). We notice that the LDOSs reproduce unambiguously the different NW building blocks. Indeed, for $R \leq 0.4$ nm, which means within the NW core, both the LDOS (red and green curves in Fig. (4.9a)) and the band gap correspond to those of a SiC NW; for $R \geq 0.84$ nm the LDOS and the band gap are related to those of amorphous SiO_x (blue curve in (4.9a)); finally for R in the range $0.4 - 0.84$ nm, corresponding to the interface region, we find a shape of the LDOS (brown curve in Fig. (4.9a)) intermediate between the SiC core and the SiO_x shell (i.e. VBM reminds that of SiO_x , whereas the CBM resembles that of SiC).

Furthermore we studied also the Projected Density of States (PDOS) that will be us useful for interpretation of XANES spectra later. The latter is reported in Fig. (4.10) for the sample with $d = 1.2$ nm. We notice that p orbitals of oxygen atoms contribute to the top of the valence band only in the $-\text{OH}$ case, while the lower energy conduction states for both $-\text{H}$ and $-\text{OH}$ terminations are mainly composed by p - and d -hybridized silicon orbitals. This reduces the band gap in $-\text{OH}$ terminated NWs.

4.3.3 Simulations of XANES spectra

XANES experimental spectra were reproduced from ab-initio simulations using density functional theory. To perform these calculations we used the XSpectra computer code [52], which relies on the QUANTUM ESPRESSO suite [3]. The input of the approach implemented in XSpectra is basically the ground state electron density. K-edge absorption spectra are computed upon the knowledge of the electron density via the continued fraction method and the Lanczos chain algorithm, tailored to be used with pseudopotentials [52]. The convenience of using this approach is mainly

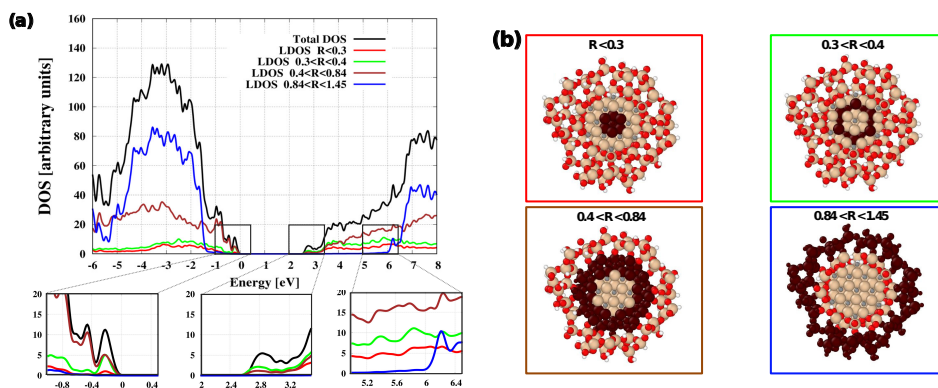


FIGURE 4.9: (a) DOS of our computational model of SiC/SiO_x core/shell NW; the upper panel (a) shows both the total Density of States (black line) and the local DOS (LDOS) obtained by projecting the DOS onto the atoms belonging to different radial shells; the three middle panels report zooms of the top (bottom) region of the valence band (conduction band); (b) NW radial shells (represented in dark brown) on which the DOS projections are performed.

due to its low computational cost, as it is based on one only self-consistent DFT run and does not require the explicit calculation of the empty states. The drawback of this method is that one loses useful pieces of information (e.g. symmetry) on the final transition states.

The absorption of X-ray photons results typically in a core-hole, while the electron is promoted to an empty state. To enable the pseudopotential approach, in which core electrons are typically frozen, to describe this mechanism, one needs to perform DFT simulations with pseudopotentials carrying an inner hole, typically in the $1s$ state for K-edge absorption spectroscopy. Ultra-soft core-hole pseudopotentials, used to perform XANES simulations, for treating the ionic core- valence electron interactions in C, O, and Si atoms can be found in the QUANTUM ESPRESSO database [53]. The all-electron wavefunction is then recovered via the projector augmented wave (PAW) formalism [54]. In particular, for the C pseudopotential we used two projectors on the s and p atomic states, while for Si and O we used two projectors for the s and p states and one for the d state. DFT simulations have been carried out using a kinetic energy cut-off equal to 544 eV for wavefunctions and four times as much for the electron density. A $1 \times 1 \times 2$ k -point sampling of the Brillouin zone was sufficient to obtain converged energy and DOS below chemical accuracy.

XANES spectra are calculated in the dipole approximation, thus due to symmetry K-edge spectroscopy probes only the transitions from $1s$ to np or s/p -hybridized

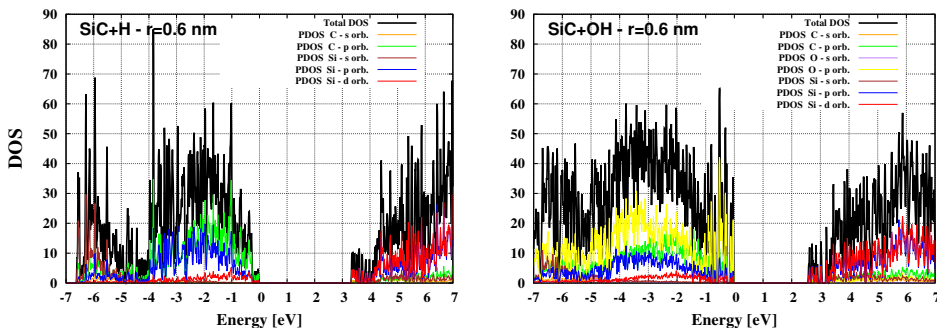


FIGURE 4.10: Total and Projected DOS of SiC core NWs with diameter equal to 1.2 nm for both $-H$ (left) and $-OH$ (right) terminations

orbitals. Spectra simulations were performed using a $1 \times 1 \times 4$ k -point grid for sampling the Brillouin zone. Three different polarization vectors of the incident light were considered, that is one along the NW symmetry axis (z -axis) and two perpendicular to it (x and y directions). A dependence of the spectral signals on polarization directions is expected in presence of radial anisotropy, e.g. for defected NWs. In all XANES simulations spectral lineshapes have been broadened by a convolution with a Lorentzian function having the half width at half maximum constant at all energies and equal to 0.8 eV.

Numerical tests were carried out in the case of SiC crystals and of SiC NW with $-OH$ terminations. Good agreement of our calculations with experimental measurements and similar computer simulations [35, 37] on these structures was found using the above-mentioned computational parameters and reported in Fig. (4.11).

These encouraging results on SiC NW led us to use the model of SiC/SiO_x core/shell NW previously introduced to interpret our experimental absorption data.

4.4 Results and Discussion

4.4.1 Silicon K-edge XANES spectra

Before investigating the Si, O, and C K-edge absorption lineshape of the SiC/SiO_x core/shell NW, we start our analysis by simulating the electronic and optical properties of the OH-terminated SiC core. This configuration represents a simplified model of the SiC core NW, which can be experimentally obtained by completely etching away the silica outer shell (HF-etched SiC NWs).

In Fig. (4.12) we report the theoretical Si K-edge spectrum (black dashed line) in comparison to our experimental data (red line). Furthermore, in this figure we report the spectral contribution to the total lineshape of the light polarized along the

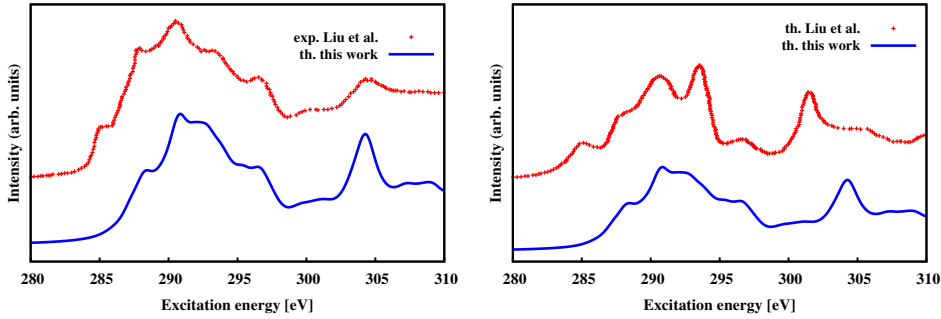


FIGURE 4.11: Left: comparison between experimental (from Ref. [35], red curve) and our theoretical C K-edge adsorption spectra of bulk SiC crystal (blue curve). Right: comparison between the theoretical (red curve) C K-edge adsorption spectra of bulk SiC crystal (from Ref. [35]) and our simulations (blue curve).

three orthogonal cartesian directions: the blue, khaki, and green curves show the spectra originating from x -, y -, and z -polarized electric fields, respectively. The total spectrum is obtained by averaging along the three polarization directions. The experimental lineshape of the Si K-edge exhibits five features A–E that are typically observed for 3C-SiC thin films [55, 56, 57] and HF-etched 3C-SiC NWs [35, 58]. Differently to previous reports, we observe an additional feature B* at 1847 eV that becomes only visible when the freshly etched sample was immediately inserted into the UHV chamber. Longer exposure to air leads to the disappearance of this feature, suggesting that it originates from the SiC/SiO_x interface (i.e., before any re-oxidation appears). We notice that the simulated spectra are in good agreement with experiments, and they reproduce all the peaks denoted in Fig. (4.12). It is noteworthy that the shoulder A (at 1841.5 eV in the experimental spectrum) strongly depends on the polarization direction: it is well separated from the main peak B for x - and y -polarized electric fields, whereas it decreases in intensity and appears as shoulder for z polarization direction. Moreover, peak B* is more pronounced in the spectrum with the z -polarized electric field. Overall, the theoretical spectral lineshape in the z polarization direction agrees well with the experimental one.

The peaks denoted as B, D, and E in Fig. (4.12) correspond to transitions from the Si1s orbital to hybridized states from both Si and C. In particular, the main resonance (B peak at 1845 eV), and the peaks D and E at 1849 and 1867 eV, respectively, can be attributed to the transition of Si1s electrons to orbitals that have lost their atomic character and arise by mixing hybridized 2s and 2p orbitals of C and hybridized 3s, 3p, and 3d orbitals of Si [58]. This combination is due to the overlap between 3s, 3p, and 3d orbitals from Si and 2s and 2p orbitals from C, which are degenerate as one can clearly see in Fig. (4.10).

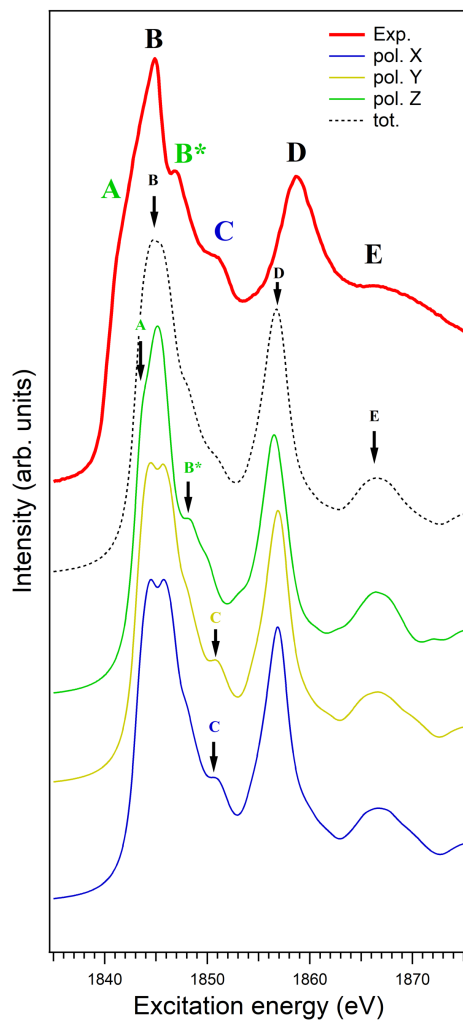


FIGURE 4.12: Experimental Si K-edge XANES spectrum of HF-etched SiC core nanowires (red), in comparison with theoretical XANES spectra of (dashed line) an OH-terminated SiC core NW. Blue, khaki, and green curves show the spectra originating from x -, y -, and z -polarized electric fields, respectively.

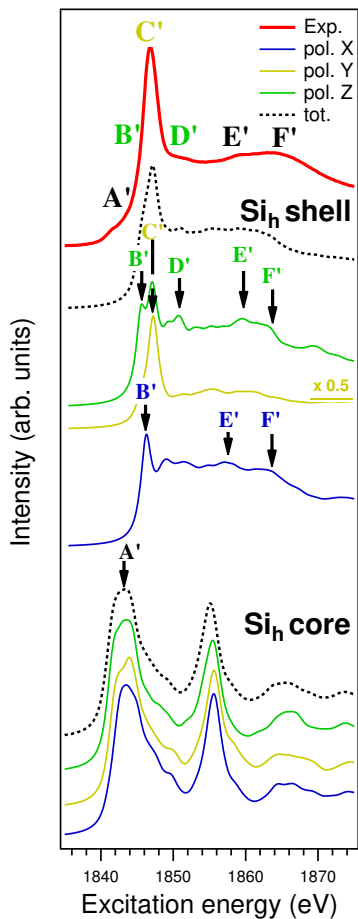


FIGURE 4.13: Experimental Si K-edge XANES spectrum of as-grown SiC/SiO_x core/shell NWs (red), in comparison with theoretical XANES spectra (dashed line) of a SiC/SiO_x core/shell NW (without carbon defects). Si_h^{shell} and Si_h^{core} represent the absorption spectra obtained by creating a core-hole in a silicon atom within the SiO_x shell and the SiC core, respectively. Blue, khaki, and green curves show the spectra originating from *x*-, *y*-, and *z*-polarized electric fields, respectively.

Theoretical interpretation of the Si K-edge absorption spectra has been carried out by comparison with our experimental measurements also in the SiC/SiO_x core/shell NW. Both simulated and experimental Si K-edge spectra, along with the contributions resolved in the polarization directions of the incident electric field, are reported in Fig. (4.13). Si atoms in different chemical environments are present in the SiC core as well as in the SiO_x outer shell. Thus, theoretical spectra were obtained by creating core-holes in two different locations of the NW. In Fig. (4.13) the K-edge spectrum obtained via photon absorption by Si atoms within the outer shell of the NW is labeled as Si_h^{shell} (black dashed line in the upper part of the figure), while the spectrum labeled as Si_h^{core} (black dashed line in the lower part of the figure) has been generated by creating the core-hole in the Si atoms within the NW SiC core. The Si_h^{shell} spectrum reports the features typical of silica, that is a single main peak C' [52]. At variance, the Si_h^{core} absorption spectrum is similar to that one obtained in the SiC+OH NW (see Fig. (4.12)). The pre-edge peak labeled as A' at 1842 eV in the experimental spectrum in Fig. (4.13) can be unambiguously attributed to a contribution stemming from the SiC core, since it cannot be found in the SiO_x NWs without SiC core. In general, the spectral lineshape can be rationalized as the convolution of the signals obtained by creating the core-hole in different locations in the SiC core and in the SiO_x outer shell. Nevertheless, a much stronger contribution of the Si_h^{shell} is visible. Taking into account this feature, which can be understood by considering that the TEY experimental technique probes mainly the sample's surface, good agreement is obtained between experimental (red line) and theoretical spectral lineshape. Similar to Fig. (4.12), the shoulder B' at 1845.5 eV is strongly dependent on the polarization direction (i.e., more pronounced for x- and z-polarized electric fields), and the spectral lineshape of the experimental data is mainly dominated by the theoretical one of the Si_h^{shell} in z polarization direction. We notice that the main peak C' in Fig. (4.13) (at 1847 eV) is largely due to electron transitions from Si1s to a combination of Si3p,3d orbitals, due to the selection rules (see Fig. (4.10) for a symmetry-resolved representation of the DOS)

4.4.2 Oxygen K-edge XANES spectra

The comparison between the theoretical O K-edge XANES spectra (black dashed lines) obtained in our SiC core+OH model NW and the experimental O K-edge XANES spectrum of HF-etched SiC core NWs (red line) is reported in Fig. (4.14). In all simulated spectra blue, khaki, and green curves show the features originating from x-, y-, and z-polarized electric fields, respectively. The two theoretical spectra (black dashed lines) in the upper and middle parts of Fig. (4.14), labeled as -Si-O_hH and -C-O_hH, correspond to spectral features originating from different locations of the excited O atom on the NW surface: on the one hand, O binds to Si (-Si-O_hH), and

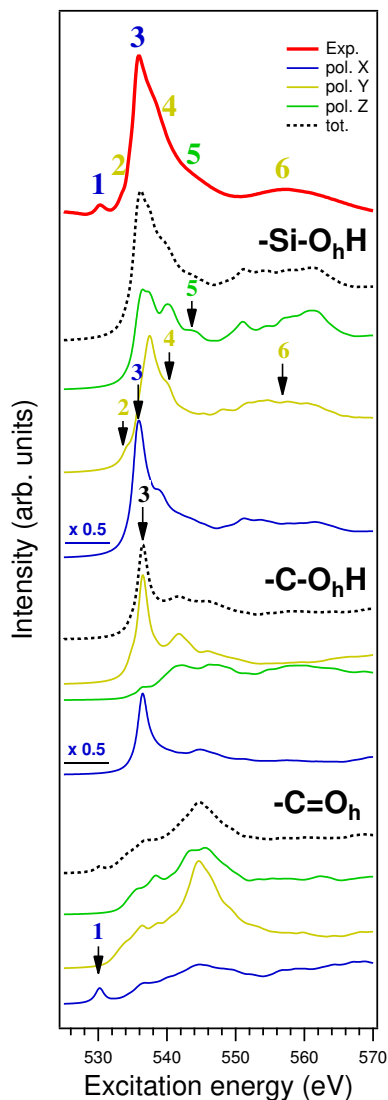


FIGURE 4.14: Experimental O K-edge XANES spectrum of HF-etched SiC core nanowires (red line), in comparison with theoretical spectra of an OH-terminated SiC core NW (black dashed lines). The three theoretical spectra with the relevant polarizations (blue, khaki, and green curves show the spectra originating from x -, y -, and z -polarized electric fields, respectively) refer to the -OH radicals attached to a silicon atom (upper theoretical spectrum), to a carbon atom (middle theoretical spectrum), to a carbon atom (middle theoretical spectrum), to a carbon atom (middle theoretical spectrum), and to unsaturated oxygen (lower theoretical spectrum).

on the other hand to C ($-\text{C}-\text{O}_h\text{H}$). We notice that good agreement between experimental and theoretical data is found, with the main features fully described by ab-initio simulations using our NW model. In particular, the main peak 3 at 536 eV is present in both simulated spectra $-\text{Si}-\text{O}_h\text{H}$ (x -polarization) and $-\text{C}-\text{O}_h\text{H}$ (x - and y -polarization), whereas the shoulder 2 at 534 eV and the features 4, 5 and 6 (at 540, 544 and 557 eV) are only reproduced by the $-\text{Si}-\text{O}_h\text{H}$ simulated spectra (contributions from y - and z -polarization).

Finally, in the lower part of Fig. (4.14) we report the spectrum, labeled as $-\text{C}=\text{O}_h$, simulating the presence of unsaturated oxocarbons (carbonyl groups) on the SiC NW surface. The lineshape, originating from O atoms that form double covalent bonds with the adjacent carbon atom, explains the pre-edge peak at 530 eV denoted by 1 in the experimental spectrum (red line). The peaks in all spectra can be described in terms of electron excitations from the $\text{O}1s$ orbital to a mixing between hybridized $2s,2p$ orbitals of C or $3s,3p$ orbitals of Si and the $2s,2p$ orbitals of O.

In Fig. (4.15) we report the comparison between experimental (red line) and simulated (black dashed line) O K-edge XANES spectra of the SiC/SiO_x core/shell NW. In addition, the lower part of Fig. (4.15) shows the simulated spectra of $-\text{C}=\text{O}_h$ carbonyl groups on the NWs' silica surface. The main features 2' – 6' of the experimental spectrum are all clearly visible in the theoretical spectrum without carbon defects, when the different polarization contributions are summed up (blue, khaki, and green curves show the spectra originating from x -, y -, and z -polarized electric fields, respectively). This finding further supports our computational model of the SiC/SiO_x core/shell NW. In particular, the main broad peak in the energy range 535-540 eV is split into two separate contributions, namely into peak 2' at 535 eV originating from the y - (khaki line) and z - (green line) polarization directions of the incident light, whereas peak 3' at 537 eV originates from the x - (blue line) polarization direction. Moreover, the shoulder 4' visible at 541 eV is recovered by convolution of features present in all the polarization directions x , y and z . The broad features 5' and 6' found in the experimental spectrum at 552.5 and 558 eV, respectively, are present in all the three polarization directions of the simulated spectra, but its lineshape can be mainly understood by looking at the lineshape of the y -polarization contribution (khaki curve).

A similar experimental lineshape of the O K-edge XANES spectrum, i.e., a relatively broad resonance between 535 – 550 eV, but no pre-edge peak 1' was previously observed in a SiO₂ thin film (4 nm) thermally oxidized on SiC [32] as well as in thermally oxidized Si NWs [59]. At variance, our SiO_x NWs (grown without SiC core) exhibit the same pre-edge peak at 530 eV than the SiC/SiO_x core/shell NWs. It is noteworthy that a different view about the origin of the pre-edge peak 1/1' in O K-edge XANES spectra of SiO_x-based materials exists in the literature. For instance, in SiO_x films grown on SiC it has been assumed that it originates from defect states such as O vacancies at the SiO_x/SiC interface [30]. Furthermore, a similar pre-edge peak has been observed in quartz [60], which has been assigned to the transition from the

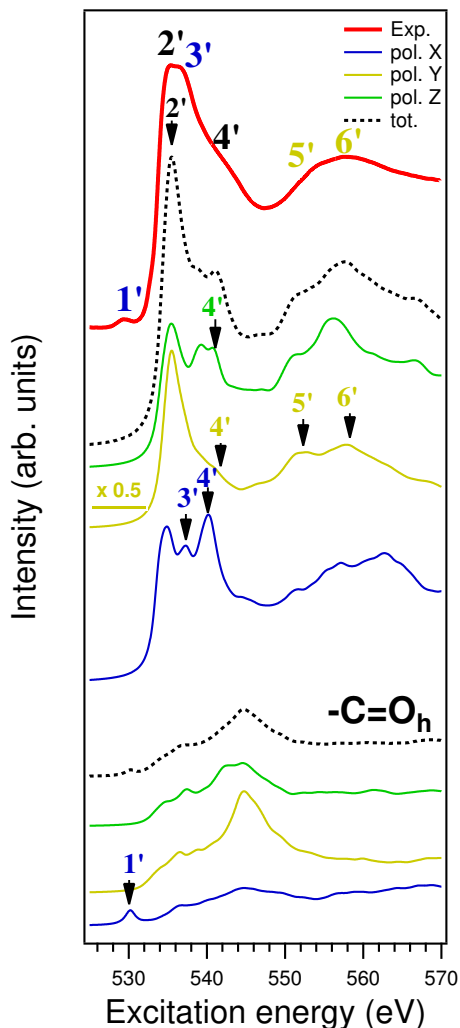


FIGURE 4.15: Experimental O K-edge XANES spectrum of as-grown SiC/SiO_x core/shell NWs (red), in comparison with theoretical spectra (black dashed line) of a SiC/SiO_x core/shell NW (without carbon defects). In the lower panel we report again the spectral features originating from unsaturated oxygen. Blue, khaki, and green curves show the spectra originating from *x*-, *y*-, and *z*-polarized electric fields, respectively.

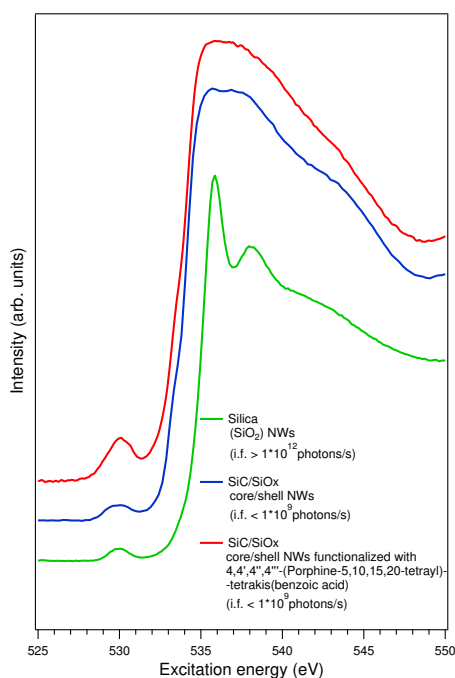


FIGURE 4.16: Experimental O K-edge XANES spectra of bare SiO_x NWs grown without SiC core (red) collected with high incident photon flux (i.f.), as-grown SiC/SiO_x core/shell NWs (blue) collected with low i.f., and SiC/SiO_x core/shell NWs functionalized with a porphyrin molecule bearing carboxylic acid functional groups (red) collected with low i.f..

O1s electron to the π^* orbital states of O₂ molecules that are induced by radiation damage from the X-ray beam with high incident flux [61]. At odds with this theory, we could observe the pre-edge peak even during acquisition at very low flux, thus, we can exclude any effects caused by radiation damage. As in the case of O K-edge spectrum of HF-etched SiC core NW (see Fig. (4.14)) the pre-edge peak 1' located at 530 eV in Fig. (4.15) can be safely attributed to double bonded oxygen, e.g. belonging to carbonyl groups (see simulated spectra of $-\text{C}=\text{O}_h$ in the lower part of Fig. (4.15)). To further confirm this theory, we measured the O K-edge XANES spectrum of NWs after surface functionalization with an organic molecule containing carboxyl groups (see Fig. (4.16)). Indeed, we found an increase of the pre-edge peak, supporting the idea that it originates from carbon-containing (functional) groups such as carbonyl and/or carboxyl groups [62].

4.4.3 Carbon K-edge XANES spectra

The comparison between the C K-edge XANES simulated spectrum of OH-terminated SiC core NW (black dashed line) and the experimental spectrum of HF-etched SiC core NWs (red line) is reported in Fig. (4.17). The color code for the three orthogonal polarization directions of the incident X-ray photon beam is the same as for the previously discussed Si and O K-edge XANES spectra. To consider contributions stemming from the SiC/SiO_x interface, we simulated a typical carbon-related defect (lower part of Fig. (4.17)). In principle, this structure is created when a Si atom in SiO_x is substituted by a C atom, and resembles a C atom in sp^3 configuration corresponding to SiO_xC_y species (i.e., silicon oxycarbides indicated as grey-shaded area in the structure in Fig. (4.17)), which are typically resistant to HF etching. We notice that the clusters represented in Figs. (4.17) and (4.18) were cut out of the full simulation cell with the only aim of zooming the several chemically different local environments in which carbon atoms can be found in their binding to others atoms. These realistic binding conditions of the carbon atoms within the different clusters, which are embedded in the NW, are then used to disentangle the spectral contributions of the single defects to the total lineshape. Nevertheless, XANES spectra are calculated on the full simulation cell.

Our experimental lineshape of the C K-edge XANES spectrum is in good agreement with previous reports for 3C-SiC thin films [63, 64, 65] and HF-etched 3C-SiC NWs [35, 58]. Apart from the first feature I located at 284.5 eV, the theoretical spectrum (without defects) reproduces well the experimental shape. In our model of SiC core NW with $-OH$ termination, C atoms that are not on the surface form sp^3 hybridized orbitals bonding with Si atoms. We assign the spectral features in the near edge region (energy range between 285 and 300 eV) to the dipole transitions from the C1s orbitals to σ^* -character bands formed by the sp^3 -hybridized orbitals of C, tetrahedrally coordinated with four Si atoms [35]. At variance, the pre-edge peak I can be attributed to the transition from the (sp^3) C1s atoms at the SiO_x/SiC interface (see lower panel in Fig. (4.17)), where a layer of silicon oxycarbides is typically formed due to the growth process and conditions and remains as residual thin (0.5 – 2 nm) layer around the SiC core [18].

It is noteworthy, that such a pre-edge peak I has been previously assigned in (HF-etched) 3C-SiC NWs to graphite-like π^* states of sp^2 bonded carbon atoms [58]. Although we cannot exclude any contributions from C atoms in sp^2 configuration, our recent findings strongly suggest that a strong contributions originates from the silicon oxycarbides (in sp^3 configuration) present at the SiO_x/SiC interface.

Finally, in Fig. (4.18) we report the C K-edge XANES theoretical spectra of the SiC/SiO_x core/shell NW (black dashed lines) compared to our experimental data (red line). Here we report four different simulated spectra corresponding to different chemical environments, and thus different bonding, in which C atoms can be reasonably found [66]. Special emphasis was drawn to simulate C atoms not only in sp^3

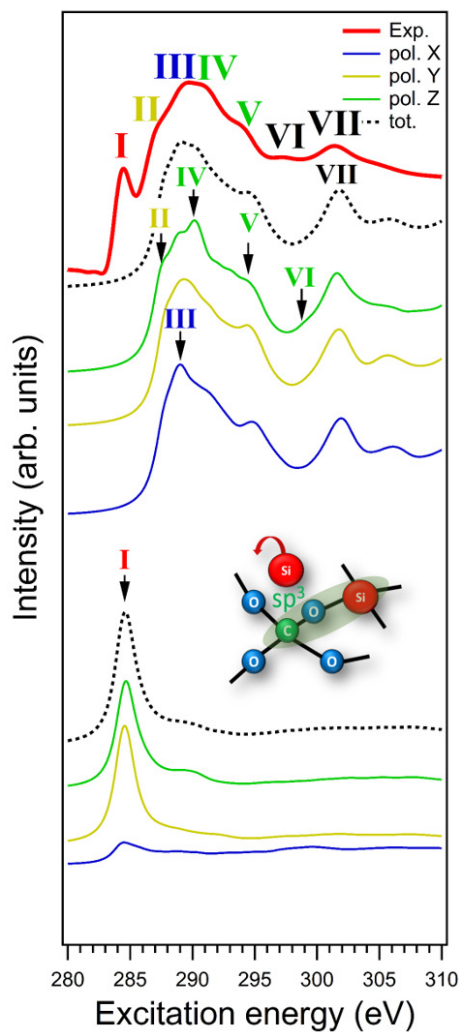


FIGURE 4.17: Experimental C K-edge XANES spectrum of HF-etched SiC core NWs (in red), in comparison with theoretical spectra (black dashed line) of an OH-terminated SiC core NW. The simulated spectra in the lower panel refer to residual silicon oxycarbides (grey-shaded area in the structure) that remain as residuals at the SiC surface after etching the SiO_x shell. Blue, khaki, and green curves show the spectra originating from *x*-, *y*-, and *z*-polarized electric fields, respectively.

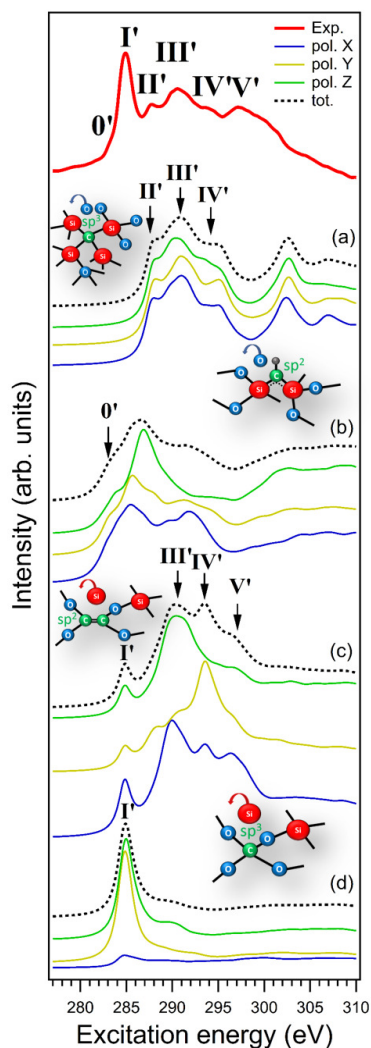


FIGURE 4.18: Experimental C K-edge XANES spectrum of as-grown SiC/SiO_x core/shell NWs (red), compared to theoretical XANES spectra (black dashed line) of SiC/SiO_x core/shell NW. The four spectra reported in this figure are obtained by including several different carbon defects in the shell, which are represented in the right hand side. Spectra originating from *x*-, *y*-, and *z*-polarized electric fields are reported in blue, khaki, and green respectively.

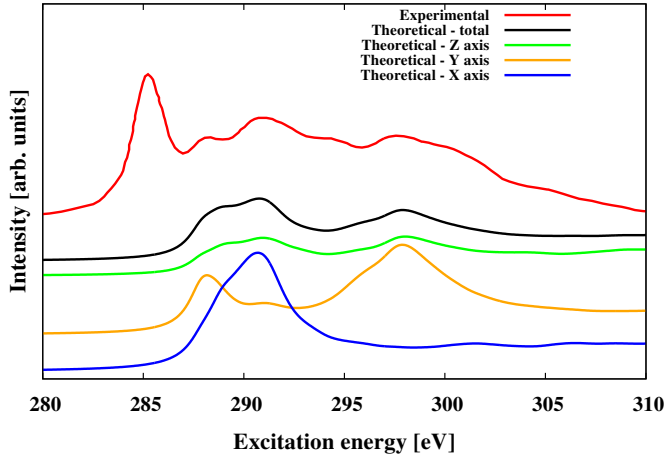


FIGURE 4.19: Experimental C K-edge XANES spectrum of as-grown SiC/SiO_x core/shell NWs (red), in comparison with theoretical XANES spectra from our SiC/SiO_x core/shell NW model including a carboxyl defect within the shell.

but also in sp^2 configuration, since additional peaks in the C K-edge XANES spectrum of SiC/SiO_x core/shell NWs have been associated to sp^2 C defects present in or on the silica shell, [35] similar to the SiC case. The different coordination bonds are represented close to the corresponding XANES spectrum in Fig. (4.18).

The upper theoretical spectrum in Fig. (4.18) (a) is obtained when an oxygen atom in the SiO_x shell is substituted by a carbon atom, i.e., a sp^3 configuration very similar to that reported in Fig. (4.17) (upper panel) for the $-OH$ terminated SiC NW. The presence of additional different C defects corresponding to the three lower spectra (b)-(d) in Fig. (4.18) could be explained by the carbothermal process used in the present study to synthesize the SiC/SiO_x core/shell NWs, which inevitably creates C inclusions/contaminants in the SiO_x shell. The additional defects studied in this work can be divided in two classes, namely substitutional inclusions and surface contaminants. Within the first class belongs the substitution of an oxygen atom in the shell with a $-CH$ group (sp^2 configuration, see Fig. (4.18b)), the substitution of a Si atom in the shell with two C atoms forming a double bond (sp^2 configuration, see Fig. (4.18c)), and the substitution of a silicon atom in the shell with a four coordinated carbon atom (sp^3 configuration, see Fig. (4.18d)), similar to the case in Fig. (4.17, lower panel). The second class of defects is characterized by the surface contamination of carboxyl group and the relevant spectrum is reported in the Fig. (4.19).

As can be seen, the theoretical spectrum in Fig. (4.18a) mainly reproduces the features II'-V' of the experimental spectrum, whereas the shoulder 0' at 283 eV and

the main peak I' at 285 eV, respectively, are not present.

However, the theoretical spectrum of the sp^2 configuration (b) in Fig. (4.18) indeed reproduces the shoulder O' , whereas the sp^2 configuration (c) in Fig. (4.18) contributes to the main peak I' . The spectrum of the sp^3 configuration in Fig. (4.18d) is once again composed by a single main peak which gives a strong contribution to peak I' .

Our detailed theoretical analysis for different configurations of the SiC/SiO_x core/shell NWs, while not claiming to be exhaustive, demonstrates that the XANES experimental signals are due to a variety of defects and that spectral lineshapes crucially depend on the local bonding environment of the excited atom, which must be carefully assessed.

4.5 Conclusions

SiC/SiO_x core/shell NWs are very promising systems in a variety of applications, ranging from energy harvesting to developing novel methods for cancer therapy and diagnosis. To optimize these procedures, an accurate characterization of the electronic and optical properties of these novel structures via a synergic experimental and computational study is necessary. To the best of our knowledge this work is aimed at developing for the first time a realistic model of SiC/SiO_x core/shell NWs, relying on information gained both at experimental and theoretical level.

SiC/SiO_x core/shell NWs were synthesized via a low-cost carbothermal method. Structural features of these NWs were investigated via the acquisition of XANES spectra in TEY mode and their theoretical interpretation from ab-initio simulations. Our NW model, including defected sites and interfacial boundaries between SiC and SiO_x, reproduces remarkably well the main features of C, Si, and O K-edge XANES spectra of these structures arranged in several configurations and stoichiometry.

Both optical and electronic characteristics, such as the DOS, of these systems are crucially affected by two counteracting effects, that is quantum confinement and surface termination. Quantum confinement, induced by the reduced dimensionality of the wire with respect to bulk SiC, results into the modification of the NWs band structure from indirect to direct band gap, with a VBM to CBM distance inversely dependent on wire diameter. Surface passivation of the dangling bonds affects both the NW boundaries and the interfacial region. We devised the presence of a variety of defects, such as substitutional C, and different chemical coordination to obtain an overall good agreement between simulated and experimental XANES spectral lineshapes at the Si, O, and C absorption K-edge. This study demonstrates the crucial importance of defective sites in affecting the electronic characteristics of SiC NWs, so to avoid unintentional doping that hinders the development of high-performance SiC-based field-effect transistors.

Finally, the realistic model of SiC/SiO_x core/shell NWs proposed in this combined experimental and theoretical study, being able to deliver an accurate interpretation of the recorded XANES spectra, demonstrates to be a valuable tool towards the optimal design and application of these nanosystems in real devices.

Bibliography

- [1] S. Plimpton, Fast parallel algorithms for short-range molecular dynamics, *Journal of Computational Physics* 117 (1) (1995) 1 – 19. doi:10.1006/jcph.1995.1039.
URL <http://dx.doi.org/10.1006/jcph.1995.1039>
- [2] B. Aradi, B. Hourahine, T. Frauenheim, Dftb+, a sparse matrix-based implementation of the dftb method, *Journal of Physical Chemistry* 111.
- [3] P. Giannozzi, S. Baroni, N. Bonini, M. Calandra, R. Car, C. Cavazzoni, D. Ceresoli, G. L. Chiarotti, M. Cococcioni, I. Dabo, A. D. Corso, S. de Gironcoli, S. Fabris, G. Fratesi, R. Gebauer, U. Gerstmann, C. Gougoussis, A. Kokalj, M. Lazzeri, L. Martin-Samos, N. Marzari, F. Mauri, R. Mazzarello, S. Paolini, A. Pasquarello, L. Paulatto, C. Sbraccia, S. Scandolo, G. Sclauzero, A. P. Seitsonen, A. Smogunov, P. Umari, R. M. Wentzcovitch, Quantum espresso: a modular and open-source software project for quantum simulations of materials, *Journal of Physics: Condensed Matter* 21 (39) (2009) 395502.
URL <http://stacks.iop.org/0953-8984/21/i=39/a=395502>
- [4] K. Zekentes, K. Rogdakis, Sic nanowires: Material and devices, *Journal of Physics D: Applied Physics* 44 (13) (2011) 133001. doi:10.1088/0022-3727/44/13/133001.
- [5] L. Latu-Romain, M. Ollivier, Silicon carbide based one-dimensional nanostructure growth: Towards electronics and biology perspectives, *Journal of Physics D: Applied Physics* 47 (20) (2014) 203001. doi:10.1088/0022-3727/47/20/203001.
- [6] J. Prakash, R. Venugopalan, B. M. Tripathi, S. K. Ghosh, J. K. Chakravartty, A. K. Tyagi, Chemistry of one dimensional silicon carbide materials: Principle, production, application and future prospects, *Progress in Solid State Chemistry* 43 (3) (2015) 98–122. doi:10.1016/j.progsolidstchem.2015.06.001.
- [7] Y. Zhang, X. Han, K. Zheng, Z. Zhang, X. Zhang, J. Fu, Y. Ji, Y. Hao, X. Guo, Z. Wang, Direct observation of super-plasticity of beta-sic nanowires at low temperature, *Advanced Functional Materials* 17 (17) (2007) 3435–3440. doi:10.1002/adfm.200700162.

- [8] P. Hu, S. Dong, X. Zhang, K. Gui, G. Chen, Z. Hu, Synthesis and characterization of ultralong SiC nanowires with unique optical properties, excellent thermal stability and flexible nanomechanical properties, *Scientific Reports* 7 (1) (2017) 3011. doi:10.1038/s41598-017-03588-x.
- [9] R. Wu, K. Zhou, Z. Yang, X. Qian, J. Wei, L. Liu, Y. Huang, L. Kong, L. Wang, Molten-salt-mediated synthesis of sic nanowires for microwave absorption applications, *CrystEngComm* 15 (3) (2013) 570–576. doi:10.1039/C2CE26510A.
- [10] M. Han, X. Yin, W. Duan, S. Ren, L. Zhang, L. Cheng, Hierarchical graphene/SiC nanowire networks in polymer-derived ceramics with enhanced electromagnetic wave absorbing capability, *Journal of the European Ceramic Society* 36 (11) (2016) 2695–2703. doi:10.1016/j.jeurceramsoc.2016.04.003.
- [11] W. M. Zhou, F. Fang, Z. Y. Hou, L. J. Yan, Y. F. Zhang, Field-effect transistor based on β -sic nanowire, *IEEE Electron Device Letters* 27 (6) (2006) 463–465. doi:10.1109/LED.2006.874219.
- [12] S. Z. Deng, Z. B. Li, W. L. Wang, N. S. Xu, J. Zhou, X. G. Zheng, H. T. Xu, J. Chen, J. C. She, Field emission study of SiC nanowires/nanorods directly grown on SiC ceramic substrate, *Applied Physics Letters* 89 (2) (2006) 023118. doi:10.1063/1.2220481.
- [13] M. Negri, S. C. Dhanabalan, G. Attolini, P. Lagonegro, M. Campanini, M. Bosi, F. Fabbri, G. Salviati, Tuning the radial structure of core–shell silicon carbide nanowires, *CrystEngComm* 17 (6) (2015) 1258–1263. doi:10.1039/C4CE01381F.
- [14] Z. J. Li, H. Y. Yu, G. Y. Song, J. Zhao, H. Zhang, M. Zhang, A. L. Meng, Q. D. Li, Ten-gram scale SiC@SiO₂ nanowires: high-yield synthesis towards industrialization, in situ growth mechanism and their peculiar photoluminescence and electromagnetic wave absorption properties, *Phys. Chem. Chem. Phys.* 19 (5) (2017) 3948–3954. doi:10.1039/C6CP07457J.
- [15] X. Li, J. Huang, J. Lu, Z. Feng, J. Luo, M. Xue, Fabrication and characterization of SiO₂@SiC shell–core nanowire prepared by laser sintering, *Journal of Materials Science* 52 (6) (2017) 3344–3352. doi:10.1007/s10853-016-0622-0.
- [16] Y. Ryu, Y. Tak, K. Yong, Direct growth of core-shell sic-sio₂ nanowires and field emission characteristics, *Nanotechnology* 16 (7) (2005) S370–S374. doi:10.1088/0957-4484/16/7/009.
- [17] S. Carapezzi, A. Castaldini, F. Fabbri, F. Rossi, M. Negri, G. Salviati, A. Cavallini, Cold field electron emission of large-area arrays of SiC nanowires: photo-enhancement and saturation effects, *Journal of Materials Chemistry C* 4 (2016) 8226–8234. doi:10.1039/C6TC02625G.

- [18] F. Fabbri, F. Rossi, G. Attolini, G. Salviati, S. Iannotta, L. Aversa, R. Verucchi, M. Nardi, N. Fukata, B. Dierre, T. Sekiguchi, Enhancement of the core near-band-edge emission induced by an amorphous shell in coaxial one-dimensional nanostructure: the case of SiC/SiO₂ core/shell self-organized nanowires., *Nanotechnology* 21 (34) (2010) 345702. doi:10.1088/0957-4484/21/34/345702.
- [19] M. Zhang, J. Zhao, Z. Li, H. Yu, Y. Wang, A. Meng, Q. Li, Bamboo-like 3c-sic nanowires with periodical fluctuating diameter: Homogeneous synthesis, synergistic growth mechanism, and their luminescence properties, *Journal of Solid State Chemistry* 243 (2016) 247–252. doi:10.1016/j.jssc.2016.08.032.
- [20] J. J. Niu, J. N. Wang, Q. F. Xu, Aligned silicon carbide nanowire crossed nets with high superhydrophobicity, *Langmuir* 24 (13) (2008) 6918–6923. doi:10.1021/1a800494h.
- [21] F. Fabbri, F. Rossi, M. Melucci, I. Manet, G. Attolini, L. Favaretto, M. Zambianchi, G. Salviati, Optical properties of hybrid T3Pyr/SiO₂/3C-SiC nanowires, *Nanoscale Research Letters* 7 (1) (2012) 680. doi:10.1186/1556-276X-7-680.
- [22] F. Rossi, E. Bedogni, F. Bigi, T. Rimoldi, L. Cristofolini, S. Pinelli, R. Alinovi, M. Negri, S. C. Dhanabalan, G. Attolini, F. Fabbri, M. Goldoni, A. Mutti, G. Benecchi, C. Ghetti, S. Iannotta, G. Salviati, Porphyrin conjugated sic/siox nanowires for x-ray-excited photodynamic therapy, *Sci Rep* 5 (2015) 7606. doi:10.1038/srep07606.
- [23] R. Tatti, M. Timpel, M. V. Nardi, F. Fabbri, F. Rossi, L. Pasquardini, A. Chi- asera, L. Aversa, K. Koshmak, A. Giglia, L. Pasquali, T. Rimoldi, L. Cristo- folini, G. Attolini, S. Varas, S. Iannotta, R. Verucchi, G. Salviati, Functionaliza- tion of sic/sio_x nanowires with a porphyrin derivative: a hybrid nanosystem for x-ray induced singlet oxygen generation, *Mol Sys Des Eng* 2 (2017) 165–172. doi:10.1039/x0xx00000x.
- [24] V. Presser, K. G. Nickel, Silica on silicon carbide, *Critical Reviews in Solid State and Materials Sciences* 33 (2008) 1–99. doi:10.1080/10408430701718914.
- [25] V. V. Afanasev, M. Bassler, G. Pensl, M. Schulz, Intrinsic SiC/SiO₂ Interface States, *Physica Status Solidi (a)* 162 (1) (1997) 321–337.
- [26] S. Dhar, L. C. Feldman, S. Wang, T. Isaacs-Smith, J. R. Williams, Interface trap passivation for SiO₂/(0001) C-terminated 4H-SiC, *Journal of Applied Physics* 98 (1) (2005) 014902. doi:10.1063/1.1938270.
- [27] K. C. Chang, J. Bentley, L. M. Porter, Nanoscale characterization of the silicon dioxide-silicon carbide interface using elemental mapping by energy-filtered transmission electron microscopy, *Journal of Electronic Materials* 32 (5) (2003) 464–469. doi:10.1007/s11664-003-0179-y.

- [28] Y. Hijikata, H. Yaguchi, M. Yoshikawa, S. Yoshida, Composition analysis of SiO₂/SiC interfaces by electron spectroscopic measurements using slope-shaped oxide films, *Applied Surface Science* 184 (2001) 161–166.
- [29] P. Soukiassian, F. Amy, Silicon carbide surface oxidation and SiO₂/SiC interface formation investigated by soft x-ray synchrotron radiation, *Journal of Electron Spectroscopy and Related Phenomena* 144-147 (2005) 783–788. doi:10.1016/j.eispec.2005.01.254.
- [30] D.-K. Kim, K.-S. Jeong, Y.-S. Kang, H.-K. Kang, S. W. Cho, S.-O. Kim, D. Suh, S. Kim, M.-H. Cho, Controlling the defects and transition layer in SiO₂ films grown on 4H-SiC via direct plasma-assisted oxidation, *Scientific Reports* 6 (2016) 34945. doi:10.1038/srep34945.
- [31] C. McGuinness, D. Fu, J. E. Downes, K. E. Smith, G. Hughes, J. Roche, Electronic structure of thin film silicon oxynitrides measured using soft x-ray emission and absorption, *Journal of Applied Physics* 94 (6) (2003) 3919–3922. doi:10.1063/1.1599629.
- [32] M. Tallarida, R. Sohal, D. Schmeisser, Resonant photoemission at the oxygen k edge as a tool to study the electronic properties of defects at SiO₂/Si and SiO₂/SiC interfaces, *Superlattices and Microstructures* 40 (2006) 393–398. doi:10.1016/j.spmi.2006.07.018.
- [33] R. E. Medjo, B. T. Sendja, J. M. Mane, P. O. Ateba, XAS study of the orientation of oriented carbon nanotube films, *Physica Scripta* 80 (5) (2009) 055602. doi:10.1088/0031-8949/80/05/055602.
- [34] J. Zhong, H. Zhang, X. Sun, S.-T. Lee, Synchrotron soft x-ray absorption spectroscopy study of carbon and silicon nanostructures for energy applications, *Advanced Materials* 26 (46) (2014) 7786–7806. doi:10.1002/adma.201304507.
- [35] L. Liu, Y. M. Yiu, T. K. Sham, L. Zhang, Y. Zhang, Electronic structures and optical properties of 6h- and 3c-SiC microstructures and nanostructures from x-ray absorption fine structures, x-ray excited optical luminescence, and theoretical studies, *The Journal of Physical Chemistry C* 114 (15) (2010) 6966 – 6975. arXiv:<http://dx.doi.org/10.1021/jp100277s>, doi:10.1021/jp100277s. URL <http://dx.doi.org/10.1021/jp100277s>
- [36] A. Laref, N. Alshammari, S. Laref, S. J. Luo, A theoretical study of electronic and optical properties of SiC nanowires and their quantum confinement effects, *Dalton Trans.* 43 (2014) 5505–5515. doi:10.1039/C3DT52043A. URL <http://dx.doi.org/10.1039/C3DT52043A>
- [37] E. Rosso, R. Baierle, Oxygen doped SiC nanowires: An ab initio study, *Chemical Physics Letters* 568-569 (2013) 140 – 145. doi:<https://doi.org/>

- //doi.org/10.1016/j.cplett.2013.03.039.
URL <http://www.sciencedirect.com/science/article/pii/S0009261413003710>
- [38] Z. Wang, M. Zhao, T. He, H. Zhang, X. Zhang, Z. Xi, S. Yan, X. Liu, Y. Xia, Orientation-dependent stability and quantum-confinement effects of silicon carbide nanowires, *The Journal of Physical Chemistry C* 113 (29) (2009) 12731–12735. arXiv:<https://doi.org/10.1021/jp903736v>, doi:10.1021/jp903736v.
URL <https://doi.org/10.1021/jp903736v>
- [39] R. Rurali, Electronic and structural properties of silicon carbide nanowires, *Phys. Rev. B* 71 (2005) 205405. doi:10.1103/PhysRevB.71.205405.
URL <https://link.aps.org/doi/10.1103/PhysRevB.71.205405>
- [40] W. Li, J. Zhao, D. Wang, An amorphous $\text{SiO}_2/\text{4H-siC}(0001)$ interface: Band offsets and accurate charge transition levels of typical defects, *Solid State Communications* 205 (Supplement C) (2015) 28 – 32. doi:<https://doi.org/10.1016/j.ssc.2014.12.020>.
URL <http://www.sciencedirect.com/science/article/pii/S0038109814005262>
- [41] M. Vörös, A. Gali, E. Kaxiras, T. Frauenheim, J. M. Knaup, Identification of defects at the interface between 3c-siC quantum dots and a SiO_2 embedding matrix, *Physica Status Solidi (b)* 249 (2) (2012) 360–367. doi:10.1002/pssb.201100527.
URL <http://dx.doi.org/10.1002/pssb.201100527>
- [42] M. Vörös, P. Deak, T. Frauenheim, A. Gali, The absorption spectrum of hydrogenated silicon carbide nanocrystals from ab initio calculations, *Applied Physics Letters* 96 (5) (2010) 051909. doi:10.1063/1.3308495.
URL <http://dx.doi.org/10.1063/1.3308495>
- [43] D. Beke, T. Z. Jánosi, B. Somogyi, D. A. Major, Z. Szekrényes, J. Erostyák, K. Kamarás, A. Gali, Identification of luminescence centers in molecular-sized silicon carbide nanocrystals, *The Journal Of Physical Chemistry (c)* 120 (1) (2016) 685–691. doi:10.1021/acs.jpcc.5b09503.
- [44] T. . G. S. J. Frenzel, A. F. Oliveira N. Jardillier, Semi-relativistic, self-consistent charge Slater-Koster tables for density-functional based tight-binding (dftb) for materials science simulations., TU-Dresden.
- [45] Y. Goldberg, M. E. Levinshtein, S. L. Rumyantsev, *Properties of Advanced Semiconductor Materials GaN, AlN, SiC, BN, SiC, SiGe*, John Wiley & Sons, New York, 2001.

- [46] K. Chenoweth, A. C. T. van Duin, W. A. Goddard, Reaxff reactive force field for molecular dynamics simulations of hydrocarbon oxidation, *The Journal of Physical Chemistry A* 112 (5) (2008) 1040–1053. arXiv:<http://dx.doi.org/10.1021/jp709896w>, doi:10.1021/jp709896w.
URL <http://dx.doi.org/10.1021/jp709896w>
- [47] A. D. Kulkarni, D. G. Truhlar, S. Goverapet Srinivasan, A. C. T. van Duin, P. Norman, T. E. Schwartzentruber, Oxygen interactions with silica surfaces: Coupled cluster and density functional investigation and the development of a new reaxff potential, *The Journal of Physical Chemistry C* 117 (1) (2013) 258–269. doi:10.1021/jp3086649.
URL <http://dx.doi.org/10.1021/jp3086649>
- [48] A. Cacchioli, F. Ravanetti, R. Alinovi, S. Pinelli, F. Rossi, M. Negri, E. Bedogni, M. Campanini, M. Galetti, M. Goldoni, P. Lagonegro, R. Alfieri, F. Bigi, G. Salviati, Cytocompatibility and cellular internalization mechanisms of SiC/SiO₂ Nanowires, *Nano Letters* 14 (2014) 4368–4375.
- [49] J. P. Rino, I. Ebbsjö, R. K. Kalia, A. Nakano, P. Vashishta, Structure of rings in vitreous sio₂, *Physical Review B* 47 (6) (1993) 3053 – 3062. doi:10.1103/physrevb.47.3053.
URL <http://dx.doi.org/10.1103/PhysRevB.47.3053>
- [50] J. Sarnthein, A. Pasquarello, R. Car, Model of vitreous sio₂ generated by an ab initio molecular-dynamics quench from the melt, *Physical Review B* 52 (17) (1995) 12690 – 12695. doi:10.1103/physrevb.52.12690.
URL <http://dx.doi.org/10.1103/PhysRevB.52.12690>
- [51] R. M. Van Ginhoven, H. Jonsson, L. R. Corrales, Silica glass structure generation for ab initio calculations using small samples of amorphous silica, *Physical Review B* 71 (2). doi:10.1103/physrevb.71.024208.
URL <http://dx.doi.org/10.1103/PhysRevB.71.024208>
- [52] C. Gougoussis, M. Calandra, A. P. Seitsonen, F. Mauri, First-principles calculations of x-ray absorption in a scheme based on ultrasoft pseudopotentials: From α -quartz to high- T_c compounds, *Phys. Rev. B* 80 (2009) 075102. doi:10.1103/PhysRevB.80.075102.
URL <https://link.aps.org/doi/10.1103/PhysRevB.80.075102>
- [53] <http://www.quantum-espresso.org>.
- [54] P. E. Blöchl, Projector augmented-wave method, *Phys. Rev. B* 50 (1994) 17953–17979. doi:10.1103/PhysRevB.50.17953.
URL <https://link.aps.org/doi/10.1103/PhysRevB.50.17953>

- [55] Y. K. Chang, H. H. Hsieh, W. F. Pong, M.-H. Tsai, K. H. Lee, T. E. Dann, F. Z. Chien, P. K. Tseng, K. L. Tsang, W. K. Su, L. C. Chen, S. L. Wei, K. H. Chen, D. M. Bhusari, Y. F. Chen, Electronic and atomic structures of the si-c-n thin film by x-ray-absorption spectroscopy and theoretical calculations, *Physical Review B* 58 (14) (1998) 9018–9024.
- [56] F. Neri, F. Barreca, E. Fazio, E. Barletta, G. Mondio, S. Trusso, B. Brendebach, H. Modrow, Influence of the deposition parameters on the electronic and structural properties of pulsed laser ablation prepared si₁l₁šxcx thin films, *J. Vac. Sci. Technol. A* 25 (2007) 117–125.
- [57] M. Liu, X. Yang, Y. Gao, R. Liu, H. Huang, X. Zhou, T. K. Sham, Investigation of the damage behavior in CVD SiC irradiated with 70 keV He ions by NEXAFS, Raman and TEM, *Journal of the European Ceramic Society* 37 (4) (2017) 1253–1259.
- [58] H. Zhang, Y. Xu, J. Zhou, J. Jiao, Y. Chen, H. Wang, C. Liu, Z. Jiang, Z. Wang, Stacking fault and unoccupied densities of state dependence of electromagnetic wave absorption in sic nanowires, *J. Mater. Chem. C* 3 (2015) 4416–4423. doi: 10.1039/C5TC00405E.
URL <http://dx.doi.org/10.1039/C5TC00405E>
- [59] L. Liu, T.-K. Sham, The Effect of Thermal Oxidation on the Luminescence Properties of Nanostructured Silicon, *Small* 8 (15) (2012) 2371–2380. doi:10.1002/smll.201200175.
- [60] Y. Wu, H. Fu, A. Roy, P. Song, Y. Lin, O. Kizilkaya, J. Xu, Facile one-pot synthesis of 3d graphite–sio₂ composite foam for negative resistance devices, *RSC Advances* 7 (66) (2017) 41812–41818.
- [61] G. S. Henderson, D. R. Neuville, L. Cormier, An O K-edge XANES study of glasses and crystals in the CaO-Al₂O₃-SiO₂(CAS) system, *Chemical Geology* 259 (1-2) (2009) 54–62.
- [62] K. Kim, P. Zhu, N. Li, X. Ma, Y. Chen, Characterization of oxygen containing functional groups on carbon materials with oxygen k-edge x-ray absorption near edge structure spectroscopy, *Carbon* 49 (5) (2011) 1745 – 1751. doi:<https://doi.org/10.1016/j.carbon.2010.12.060>.
URL <http://www.sciencedirect.com/science/article/pii/S0008622310009395>
- [63] M. Pedio, A. Giglia, N. Mahne, S. Nannarone, S. Giovannini, C. Cepek, F. Boscherini, R. Carboni, M. Benfatto, S. Della Longa, C k-edge nexafs of 6hsic and 3csic systems, *Physica Scripta T115* (2005) 308–311.

- [64] M. Tallarida, D. Schmeisser, F. Zheng, F. J. Himpsel, X-ray absorption and photoemission spectroscopy of 3c- and 4h-sic, *Surface Science* 600 (18) (2006) 3879–3883.
- [65] G. Monaco, M. Suman, D. Garoli, M. G. Pelizzo, P. Nicolosi, X-ray absorption study of silicon carbide thin film deposited by pulsed laser deposition, *Journal of Electron Spectroscopy and Related Phenomena* 184 (3-6) (2011) 240–244.
- [66] F. Devynck, A. Alkauskas, P. Broqvist, A. Pasquarello, Energy levels of candidate defects at sic/sio2 interfaces, *AIP Conference Proceedings* 1199 (1) (2010) 108–109. arXiv:<https://aip.scitation.org/doi/pdf/10.1063/1.3295319>, doi: 10.1063/1.3295319.
URL <https://aip.scitation.org/doi/abs/10.1063/1.3295319>

Chapter 5

Forging graphene pseudospheres to mimic curved space-times

5.1 A mathematical, physical and engineering problem

The honeycomb geometry of the graphene lattice enables the description of the electronic properties near Dirac's points in terms of relativistic, massless pseudo-particles [1]. This particular behaviour of low-energy excitations makes graphene suitable for testing some of the fundamental laws of theoretical physics in condensed matter as well as in high energy physics. For example, in principle, it can be shown [2, 3] that a graphene sheet, arranged in the shape of a Beltrami's pseudosphere, may lead to realizing the Hawking-Unruh effect, that is one of the most important prediction of quantum field theories in curved spacetimes. The latter effect leaves its signature in the particular behaviour of the local density of states (LDOS) of the carbon pseudosphere, which is similar to a Rindler thermal-like LDOS [2, 3]. In this chapter we present a computational model to build realistic carbon pseudospheres, and furthermore we calculate the LDOS of this structure for several sizes using an in-house developed TB method to confirm via numerical simulations the analytical description of the electronic properties obtained in a curved continuum.

The Beltrami's pseudosphere, reported in Fig. (5.1b), is a surface characterized by a constant negative Gaussian curvature $\kappa = -\frac{1}{R_p^2}$ where R_p is the pseudosphere radius. It represents the counterpart of the sphere, plotted in Fig. (5.1a), which is instead characterized by constant positive Gaussian curvature $\kappa = \frac{1}{R_s^2}$, where R_s is the sphere radius.

Basically the problem we are aiming to solve is to find the hexagonal tiling of the Beltrami's pseudosphere, obtained by using carbon atoms, which delivers the minimal-energy structure. The related problem on the sphere is called the Thompson

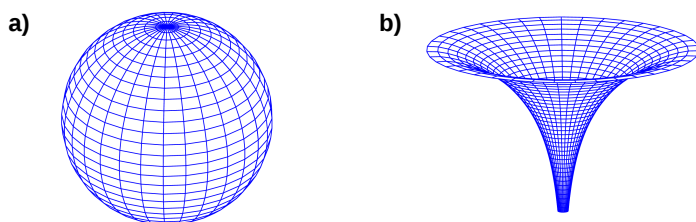


FIGURE 5.1: Left: Sphere (surface of constant positive Gaussian curvature). Right: Lower half part of the Beltrami pseudosphere (surface with constant negative gaussian curvature)

problem [4], and originally aims at finding the minimal energy configuration on the atomic sphere of a number of points interacting via a Coulomb potential. In the case of carbon atoms the solution of this issue leads to the creation of the fullerene structure, which represents a mechanically stable allotrope of carbon [5, 6, 7, 8].

The Beltrami's surface can be looked as a realization of two theorems in algebraic topology: the Hilbert theorem, which states that there are no analytic complete surfaces of constant negative Gaussian curvature in the Euclidean \mathbb{R}^3 , and additionally the Gauss-Bonnet theorem, which connects differential geometry (curvature) and topology (Euler characteristic) of manifolds by demonstrating that one cannot tile the pseudosphere surface using hexagons only, such as in planar graphene. This is a major consequence of the negative curvature.

A first insight for finding a minimal energy tiling of the Beltrami's pseudosphere was attempted in Ref. [9]. However, the latter study concerned model graphene pseudospheres to determine their energetic stability. Nevertheless, in order to observe the coupling of the Dirac electronic field with the curvature, the radius of the pseudosphere containing the geometrical model of sp^2 carbon atoms must be in principle the largest possible. The approach presented in this chapter aims first to go beyond that one proposed by Taioli *et al.* [9]. In particular, we develop a tailored dualization procedure to find energetically stable configurations containing millions of carbon atoms. Second, we calculate the electronic structure of these carbon pseudospheres using a multiscale approach. In this respect, indeed, due to the extended size of the system we devise a tight binding approach, in conjunction with the Kernel Polynomial Method (KPM) to avoid the diagonalization of the Hamiltonian matrix. The topics presented in this chapter represent by all means challenging and interesting tasks from many perspectives, spanning different research areas, such as geometrical topology (the tessellation problem), physics (black-hole analogue physics), and

mechanical engineering (the assessment of the structural stability of this novel carbon allotrope). Finally, we notice that all the computational results described in this chapter are based on in-house developed and tailored codes, which can be of course extended to study different geometrical arrangements tiled by atomic centers.

5.2 Computational Methods

5.2.1 Tiling the Beltrami's pseudosphere by three-coordinated carbon atoms

Once fixed the length of the pseudosphere along the axis of revolution, which means the top to bottom distance between the centers of the largest and minimum circles of the structure, the steps followed to tile the Beltrami's pseudosphere by carbon atoms can be summarized as follows:

- I. We assess the exact number of carbon atoms N that must be present to tessellate the surface of the Beltrami's pseudosphere by using the planar graphene density ($0.379 \text{ atoms}/\text{\AA}^2$) as a reference.
- II. We create a planar graph (N, F, E) of N vertices, F faces and E edges. The N vertices represent carbon atoms which are intentionally compressed in this initial configuration (meaning that the carbon-to-carbon bond lengths are shortened with respect to the usual value of 1.42 \AA). Each vertex is linked to the three nearest neighbours by edges, representing bonds, and is shared by three faces.
- III. The graph of compressed planar graphene is mapped on the Beltrami's pseudosphere surface via a one-to-one (injective) map as the value of the z coordinate (along the axis of revolution) of the vertices is unambiguously determined by fixing the (x, y) coordinate couple, i.e. $z = z(x, y)$.
- IV. We find the atomic arrangements that provide minima of the potential energy surface. In order to achieve that, we carry out mixed Monte Carlo (based on the WWW method [10]) and molecular dynamics (based on the FIRE approach [11]) simulations, whose details will be explained further below.
- V. Finally, once local minima are found, we developed a dualization algorithm to increase the number of atoms N by exploiting the 3-connectivity of the graph.

All these points will be explained in detail in the following.

Step I

The first issue we face is to assess the number of atoms necessary to tile the surface of the Beltrami's pseudosphere. The area of this surface, represented in Fig.

(5.1b), is given by $2\pi R_p^2$. Moreover, we notice that the carbon atoms at the very end of the pseudosphere, both in the top and in the bottom circumferences, are characterized by the presence of dangling bonds differently from the carbon atoms in the body of the structure which present sp^2 -hybridized and completely saturated bonds. It is arguable that the presence of these dangling bonds in proximity of the largest and smallest circumferences can modify dramatically the electronic properties of the carbon pseudosphere, particularly close to the Fermi level, where usually the fingerprint of defects can be found. Thus, on the one hand we decided to introduce periodic boundary conditions to saturate the outer carbon atoms of the maximum circumference. In this regard, at the very top of the pseudosphere (the maximal circumference has radius R_p and corresponds to $z = 0$) we add a rectangular supercell with side lengths a and b periodically repeated along the x and y directions, respectively. In this way, the surface area covered by carbon atoms is $ab + \pi R_p^2$ (obtained by $ab - \pi R_p^2 + 2\pi R_p^2$).

The graphene unit cell is also chosen rectangular with side lengths $a_g = \sqrt{3} \cdot d_0$ and $b_g = 3 \cdot d_0$, where $d_0 = 1.42013 \text{ \AA}$ is the distance between nearest neighbours in planar graphene, and contains four carbon atoms. Thus, the number of atoms which must be on the pseudosphere surface is $N_p = 4 \cdot \frac{2\pi R_p^2}{3\sqrt{3}d_0^2}$. This equation can be inverted and gives a Beltrami's surface radius $R_p = d_0 \sqrt{\frac{N_p \cdot 3\sqrt{3}}{8\pi}}$. Since we want to make use of the in-plane periodic boundary conditions, the graphene simulation supercell is determined by setting up the number of unitary cells along the x (n_a) and y (n_b) axes. Nevertheless, the density of carbon atoms within the trumpet is distorted with respect to planar graphene, due to the curvature that stretches the carbon-to-carbon bonds. In particular, mapping the disk of radius R_p , cleaved out in the middle of the rectangle of surface ab , into the pseudosphere results in an increase of the effective surface area to be covered by carbon atoms and, thus, in a decreasing of the density with respect to planar graphene. To enforce a density similar to graphene also within the pseudosphere we introduce a scale factor $f_s < 1$ to multiply the edges of the rectangular supercell satisfying the following condition:

$$f_s^2 = \frac{a_g n_a b_g n_b f_s^2}{a_g n_a b_g n_b f_s^2 + \pi R_p^2} \quad (5.1)$$

From Eq. (5.1) one obtains $f_s^2 + \frac{\pi R_p^2}{a_g n_a b_g n_b} - 1 = 0$ or $f_s^2 = 1 - \frac{N_p}{2 \cdot N}$, where $N = 4n_a n_b$ is the total number of atoms.

Moreover we notice that, while the Beltrami's pseudosphere is in principle infinite, we cannot of course make it endless in real configuration space. Thus, we chose to cut circumferentially the carbon structure at the very bottom and to saturate the bonds by a zig-zag nanotube with 6 hexagons. The final carbon atoms belong thus

to the bottom circle of radius $R_{min} = \frac{3 \cdot d_0 \cdot \sqrt{3}}{\pi} \text{ \AA}$. The area below this circle must be deleted in our computation of the surface carbon density. This area can be found by the following area formula valid for our surface of revolution parametrized with v ranging over $-\infty$ to z_{min} : $A_{inf} = 2\pi R_p^2 \int_{-\infty}^{z_{min}} \text{sech}(v) \cdot \tanh(v) dv$. After subtraction of the latter surface the scale factor reads $f_s^2 = 1 - \frac{N_p}{2 \cdot N} + \frac{A_{inf}}{n_a n_b a_g b_g}$. Finally, the surface area S_p covered by the carbon atoms is equal to

$$S_p = a_g n_a b_g n_b f_s^2 + \pi R_p^2 - A_{inf} \quad (5.2)$$

which can be further divided by the area of the unit cell of planar graphene $a_g \cdot b_g$ and multiplied by four (the number of carbon atoms within the unit cell) to obtain the number of vertices of the graph to tile appropriately the pseudosphere.

Step II

With such constraints in place on the total number of carbon atoms N , one can initialize the graph by writing a list of vertices, whereby we store the information of the initial coordinates, the indices of the three nearest neighbours and the indices of three faces to which the vertex belongs.

Furthermore, by virtue of the Gauss-Bonnet theorem the number of heptagonal faces needed to tile the Beltrami's surface must be in excess of six with respect to the pentagonal faces. Thus, we add to the starting configuration seven heptagons as shown in Fig. (5.2), where we show a graph with periodic boundary conditions containing 140 vertices.

Step III

The reference frame of the graph of Fig. (5.2) is pinned in the centre of the rectangle identified by the coordinates (0,0). The vertices satisfying the relation $\sqrt{x^2 + y^2} < R_p$ were then mapped into the Beltrami's pseudosphere by calculating the z -coordinate as follows:

$$z = z(x, y) = R \cdot \left[\sqrt{1 - \frac{x^2 + y^2}{R_p^2}} - \text{atanh} \left(\sqrt{1 - \frac{x^2 + y^2}{R_p^2}} \right) \right] \quad (5.3)$$

Indeed, for given x and y the z -coordinates of the vertices on the Beltrami's surface are unambiguously determined. In Fig. (5.3) we show an example of this map from planar graphene (a) to the pseudosphere geometry with periodic boundary conditions (b).

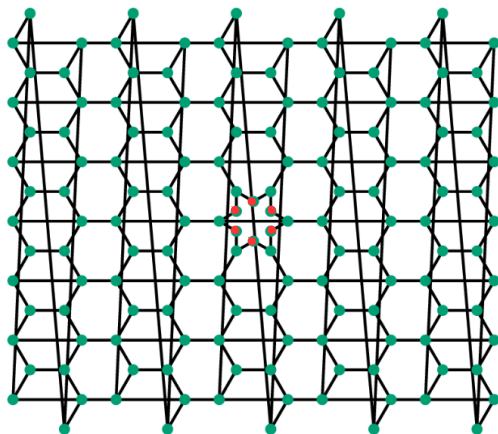


FIGURE 5.2: Starting configuration: this graph contains 140 vertices and each vertex is connected to the three nearest neighbours including periodic boundary conditions. Only the 6 atoms highlighted in red are 2-coordinated; the presence of these atoms was forced to have the excess of six heptagonal defects in the structure according to the Gauss-Bonnet theorem.

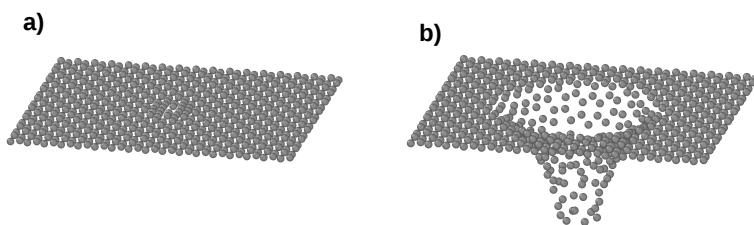


FIGURE 5.3: a) A supercell of planar compressed graphene. b) Graphene sheet mapped onto the pseudosphere surface

Step IV

To find the minimal energy configuration of carbon atoms over the surface we use the Wooten, Winer, Weaire (WWW) method [10], where materials are conceived as a net, i.e., a graph. More in detail, within this framework the information about the state of a system is embedded in both the bond topology and in the atomic coordinates, which are the variables that must be optimized. The knowledge of the bonds and positions gives access to the potential energy of the system. In particular, for the latter we chose a functional form of the Keating type, which reads [12]:

$$E = \frac{3}{16} \frac{\alpha}{d_0^2} \sum_{i,j} \left(r_{ij}^2 - d_0^2 \right)^2 + \frac{3}{8} \frac{\beta}{d_0^2} \sum_{i,j,k} \left(\mathbf{r}_{ij} \cdot \mathbf{r}_{ik} + \frac{d_0^2}{2} \right)^2 \quad (5.4)$$

where $\alpha = 25.88 \text{ eV } \text{\AA}^{-2}$ is the bond stretching force constant, $d_0 = 1.42013 \text{ \AA}$ is the carbon-to-carbon bond length in planar graphene, r_{ij} is the distance between atoms i and j , and $\beta \sim \frac{\alpha}{5}$ is the bond bending force constant [12]. The Keating model is thus a three-body potential, which depends on the bond net and the position of the atoms only.

The search for the optimal configuration that minimizes this functional form is of course an extremely complex task owing to the large number of spatial degrees of freedom. To find the minimal-energy configuration we must thus find a reliable as well as efficient and scalable procedure. We use in this regard a Monte Carlo (MC) algorithm in which the moves are given by the switching of bonds between atomic centers, and the move is accepted only if it lowers the total energy of the system according to a Metropolis algorithm [13].

In Fig. (5.4) we show a typical move to clarify our MC procedure. The trial bond-switch starts by randomly selecting an atomic center of the graph (B in Fig. (5.4)). Then, the procedure proceeds by randomly picking two neighbouring atomic centers, A and C, and another atom D, which is a neighbour of C (see Fig. (5.4a)). By breaking the bonds AB and CD and forming the new bonds AC and BD, a novel topology of the net is created (see Fig. (5.4b)). At this point we perform a trial twist, which transforms the 6-fold rings of pristine graphene into two 5-fold rings and two 7-fold rings, creating a Stone-Wales (SW) defect. This topological change of course results in moving the structure out of the minimum energy position. Therefore, the potential energy must be minimized with respect to the positions of the atoms to get the minimal potential energy (see Fig. (5.4c)).

Subsequently to each and every switch-twist trial move, the atomic coordinates of the system are “relaxed” by using the Fast Inertial Relaxation Engine (FIRE) algorithm [11]. This method is competitive with other quasi-Newton schemes and is not too difficult to implement into a computer program.

To summarize, to find the minimum energy configuration of the Beltrami’s structure at $T \sim 0 \text{ K}$ we perform the following steps:

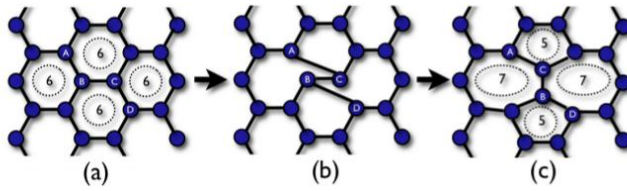


FIGURE 5.4: A bond-switch trial move in the case of graphene. (a) The initial configuration showing 6-fold rings identified by dashed circles. (b) Bonds are switched so that bonds AB and CD are broken, and AC and BD are formed. (c) The positions of the atoms have been optimized by searching the potential energy minimum. In particular, the move transforms the four 6-fold rings into two 5-fold rings and two 7-fold rings. Figure adapted from Ref. [14].

1. random switch (or switches) and twist;
2. relaxation of the geometry using the FIRE algorithm;
3. acceptance or rejection of the switch (or switches).

These steps were repeated up to when the energy did not decrease further between two switches-twists. Of course initially the number of accepted moves is large, while after some 20,000 steps for a thousand atoms all the moves were consistently rejected. At this point, being the structure close to the local minimum, the procedure halts.

Step V

The implementation of the last step stems from the need of finding in reasonable computational time Beltrami's pseudospheres containing a few millions atoms. Indeed, in order to deliver a reliable numerical test of the signature of the Hawking-Unruh effect, taking $v_F \sim 1 \times 10^6 m/sec$ [1], only electrons with an energy $E = \hbar v_F / R_p$ for $R_p \gg d_0$, which represents the intrinsic energy scale associated to the pseudosphere, have a long enough wave-length to "experience" the whole curved surface, hence their contribution to the LDOS is important. Thus, for our purposes we need to increase the size of the pseudosphere with respect to that obtainable by using the steps I to IV, through which the minimum energy configurations of structures with only a few thousands carbon atoms can be obtained.

Our approach "to move up the dimensional ladder" starts from the minimum energy configuration obtained upon completion of step IV above, and uses the 3-connectivity of the graph. We report the working scheme in Fig. (5.5). The pivotal idea is to create

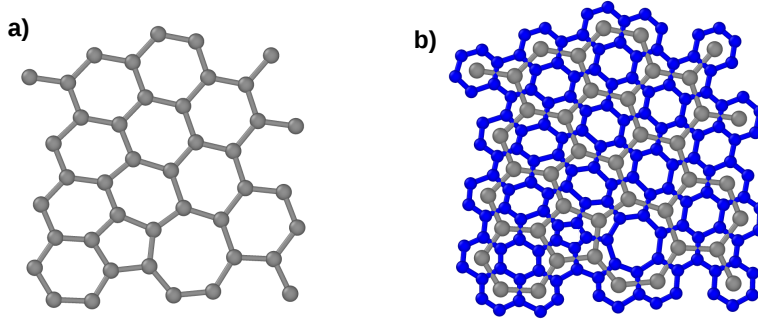


FIGURE 5.5: Example of local dualization exploiting the 3-connectivity of the planar graph. a) Parent geometry; b) Daughter geometry

a hexagon around each vertex of the initial optimized structure (see Fig. (5.5)). In such a way, the resulting structure would show bond lengths lower than those usually found in graphene. Nevertheless, by multiplying the coordinates by a $\sqrt{3}$ factor, one can stretch the bonds and recover the proper bond lengths between carbon atoms in the graphene net.

Of course the daughter structure need to be minimized after the augmentation as we will show in the results section. This simple algorithm enables us to build pseudospheres tiled by millions of atoms with a radius of the order of tens of nm. Below in Fig. (5.19), we will show an example of a pseudosphere with a radius $R_p \sim 740 \text{ \AA}$ which is the biggest one we have created, while in Fig. (5.11) we will report all the augmentation path to build a Beltrami pseudosphere with radius $R_p \sim 520 \text{ \AA}$.

5.2.2 Evaluating the electronic properties of large systems by the Tight Binding plus Kernel Polynomial Method

Multi-Orbital Tight Binding

Finally, we remind that our goal is to provide a numerical test of the Hawking-Unruh effect in pseudospheres. To do so we need to calculate the local density of states (LDOS) in extended structures, which is intimately related to this thermal effect. In order to deal with geometries containing millions of atoms, we make use of a Tight Binding (TB) approach, which is well known to describe correctly the dispersion of graphene around the six Dirac K-points in the first Brillouin zone (IBZ) [1]. In this

TABLE 5.1: Slater-Koster two-centre hopping parameters for s and p orbitals. We report the minimal elements; all the others can be obtained by permuting the direction cosines (l, m, n) between the involved atoms.

t_{ss}	$V_{ss\sigma}$
t_{sp_x}	$l V_{sp\sigma}$
$t_{p_x p_x}$	$l^2 V_{pp\sigma} + (1-l^2)V_{pp\pi}$
$t_{p_x p_y}$	$lm (V_{pp\sigma} - V_{pp\pi})$

work in particular, we are interested in the low-energy excitation region. Nevertheless, at odds with planar graphene, the Beltrami's pseudosphere has a curvature in which the p_z orbitals forming the π band are not anymore orthogonal to the in-plane direction as well as the sp^2 -hybridized orbitals do not lay in the graphene plane. Thus, a multi-orbital TB approach, in which all four valence orbitals ($2s, 2p_x, 2p_y, 2p_z$) are included in the simulation instead of the only p_z orbital, is necessary to deal with the curvature effects. In our model, the TB Hamiltonian must then be generalized to sum up also over orbital indices as follows:

$$H = \sum_{\xi i} \epsilon_{\xi}^i a_{i,\xi}^{\dagger} a_{i,\xi} + \sum_{\xi,\gamma < ij >} t_{\xi,\gamma}^{ij} a_{i,\xi}^{\dagger} a_{j,\gamma} \quad (5.5)$$

where ξ, γ are orbital label indices while i, j are site indices; $t_{\xi,\gamma}^{ij}$ indicates the hopping parameters, and the symbol $< ij >$ means that the nearest neighbours approximation is adopted. The parameters $t_{\xi,\gamma}^{ij}$ describing the hopping between orbitals in different sites were computed within the Slater-Koster formulation [15], which provides a scheme to relate the orbital symmetry, distances and directions of neighbour atoms (Tab. 5.1). We notice that owing to the non-planarity of our geometry we cannot make use of the multi-orbital parametrization typically used for graphene [16, 17] where the onsite energy of the p_z -symmetry orbitals are treated differently from the x, y orbital cartesian components along the in-plane directions (that is $\epsilon_{p_x} = \epsilon_{p_y} \neq \epsilon_{p_z}$). Therefore, we derived the TB parameters by fitting DFT ab-initio simulations of the graphene bands by further imposing that the onsite energies for the p orbitals are the same ($\epsilon_{p_x} = \epsilon_{p_y} = \epsilon_{p_z}$) and that the Fermi energy is equal to 0 eV. DFT calculations on equilibrium and strained configurations of graphene were carried out by using the Quantum Espresso code suite [18] with the same cut-off parameters adopted in chapter 3.

In Tab. (5.2) we report the TB parameters that we obtained using Eq. (5.5) for unstrained and strained graphene (second and third columns, respectively). In Fig. (5.6) we report the band structure obtained using the DFT and TB methods for several interatomic distances d ($d/d_0 = 0.96, d/d_0 = 1, d/d_0 = 1.04, d/d_0 = 1.08$) to

TABLE 5.2: Two-center integrals defined in the Slater-Koster parameters for graphene (second column) and for strained graphene (third column). Values are reported in eV and we assume the equilibrium distance in graphene $d_0 \approx 1.42$ Å

	Graphene	Strained graphene
ϵ_s	-2.8	-2.8
ϵ_p	0.0	0.0
$V_{ss\sigma}$	-5.6	$-5.6 \cdot \frac{r}{r_0} \cdot e^{-\frac{r-r_0}{0.55}}$
$V_{sp\sigma}$	5.2	$5.2 \cdot \frac{r}{r_0} \cdot e^{-\frac{r-r_0}{0.75}}$
$V_{pp\sigma}$	4.6	$4.6 \cdot \frac{r}{r_0} \cdot e^{-\frac{r-r_0}{0.55}}$
$V_{pp\pi}$	-2.44	$-2.44 \cdot \frac{r}{r_0} \cdot e^{-\frac{r-r_0}{0.41}}$

determine the variations of the hopping parameters for changing overlaps between the nearest neighbour carbon atoms.

Kernel Polynomial Method

The Kernel Polynomial Method (KPM) is a numerical approach useful to access spectral quantities of extended systems for which a direct diagonalization of the full Hamiltonian matrix is computationally unfeasible. Our aim, to find an analogy between the graphene pseudospin and a black-hole, requires to evaluate the Local Density of States (LDOS) in different regions of the largest possible Beltrami's structure. Thus, this approach turned out to be the most convenient for our purpose.

This method consists basically in the expansion of the sought quantity in terms of a set of orthogonal polynomials, and then in improving the convergence of the expansion with a kernel to avoid the spurious Gibbs oscillations [19].

In this investigation, we use the Chebyshev polynomials of the first kind, which are defined as follows:

$$T_n(x) = \cos[n \arccos(x)] \quad (5.6)$$

and of the second kind, which are defined by

$$U_n(x) = \frac{\sin[(n+1)\arccos(x)]}{\sin[\arccos(x)]} \quad (5.7)$$

Both kind of polynomials are defined in $x \in [-1, 1]$ and are orthogonal with weight functions $\frac{1}{\pi\sqrt{1-x^2}}$ and $\pi\sqrt{1-x^2}$, respectively:

$$\int_{-1}^1 T_n(x) T_m(x) \frac{1}{\pi\sqrt{1-x^2}} dx = \frac{1 + \delta_{n,0}}{2} \delta_{n,m} \quad (5.8)$$

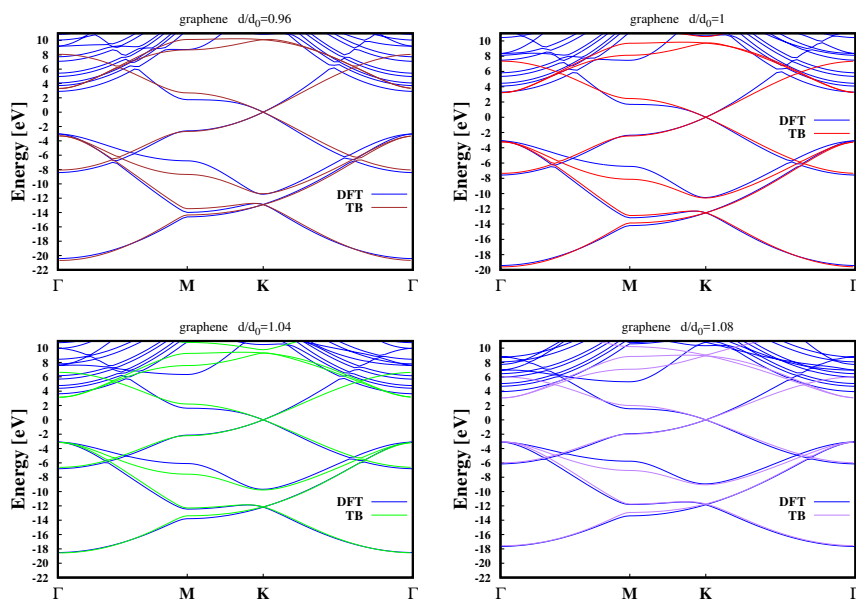


FIGURE 5.6: TB fit of the bands obtained from DFT electronic structure calculations of graphene. From left to right and from top to bottom we report the bands for a strain value $d/d_0 = 0.96$ corresponding to a biaxial compression of the graphene cell equal to 4 %; unstrained graphene ($d/d_0 = 1$); $d/d_0 = 1.04$, corresponding to a biaxial tensile strain of the graphene cell equal 4 %; $d/d_0 = 1.08$ representing a biaxial tensile strain of the graphene cell equal to 8%.

$$\int_{-1}^1 U_n(x)U_m(x)\pi\sqrt{1-x^2} dx = \frac{\pi^2}{2}\delta_{n,m} \quad (5.9)$$

With these definitions in place, one can show that the Chebyshev polynomials satisfy the following recursion relations

$$\begin{aligned} T_0(x) = 1; \quad T_1(x) = T_{-1}(x) = x; \quad T_{m+1}(x) = 2T_m(x) - T_{m-1}(x); \\ 2T_m(x)T_n(x) = T_{m+n}(x) - T_{m-n}(x); \end{aligned} \quad (5.10)$$

$$\begin{aligned} U_0(x) = 1; \quad U_{-1}(x) = 0; \quad U_{m+1}(x) = 2U_m(x) - U_{m-1}(x); \\ 2(x^2 - 1)U_{m-1}U_{n-1} = T_{m+n}(x) - T_{m-n}(x); \end{aligned} \quad (5.11)$$

The expressions (5.10) and (5.11) will be used later on in the iterative method through which the LDOS will be computed.

Generally, a function $f : [-1, 1] \rightarrow \mathbb{R}$ can be expanded in terms of Chebyshev polynomials as $f(x) = \alpha_0 + \sum_{n=1}^{\infty} \alpha_n T_n(x)$ where α_n are coefficients defined by $\alpha_k = \int_{-1}^1 f(x)T_k(x) \frac{1}{\pi\sqrt{1-x^2}} dx$. A convenient way to perform this expansion in numerical simulations is to use the modified Chebyshev polynomials defined by $\phi_n(x) = \frac{T_n(x)}{\pi\sqrt{1-x^2}}$ [19], which satisfy the same orthogonal relation as in (5.8) with the weight function of the Chebyshev polynomials of the second kind, i.e. $\int_{-1}^1 \phi_n(x)\phi_m(x)\pi\sqrt{1-x^2} dx = \frac{1+\delta_{n,0}}{2}\delta_{n,m}$. Finally, one can obtain the expansion and the relevant coefficients from:

$$\begin{aligned} f(x) = \frac{1}{\pi\sqrt{1-x^2}} \left[\mu_0 + \sum_1^{\infty} \mu_n T_n(x) \right] \\ \mu_k = \int_{-1}^1 f(x)T_k(x) dx \end{aligned} \quad (5.12)$$

The convergence of the sum in (5.12) can be improved by using a kernel, which avoids spurious oscillations close to the points where the function is not differentiable [19]. In this work, we used the Jackson kernel, for which a function can be approximated as:

$$f(x) = \frac{1}{\pi\sqrt{1-x^2}} \left[\mu_0 g_0 + \sum_{n=1}^{N_c-1} \mu_n g_n T_n(x) \right] \quad (5.13)$$

with the coefficients g_n are defined as

$$g_n = \frac{(N_c - n + 1) \cos \frac{\pi n}{N_c + 1} + \sin \frac{\pi n}{N_c + 1} \cot \frac{\pi}{N_c + 1}}{N_c + 1} \quad (5.14)$$

and N_c the truncation number related to the maximum momentum number. Using the Jackson kernel, the best achievable resolution Δ^J is

$$\Delta^J = \sqrt{1 - \cos \frac{\pi}{N_c + 1}} \quad (5.15)$$

In order to compute the moments in Eq. (5.12) one has to scale the Hamiltonian so to have eigenvalues within the range $[-1, 1]$. This can be achieved by

$$\tilde{H} = \frac{H - b}{a} \quad \text{with} \quad a = \frac{E_M - E_m}{2 - \eta}, \quad b = \frac{E_M + E_m}{2} \quad (5.16)$$

where E_m and E_M are the minimum and maximum eigenvalue, respectively, and η is a small value introduced to avoid numerical instability problems [19]. The eigenvalues E_M and E_m can be computed by using the Lanczos recursion method which, similarly to KPM, bypass the direct diagonalization of the Hamiltonian matrix [19, 20]. Furthermore, the DOS can be defined by:

$$\rho(E) = \frac{1}{L} \sum_{i=0}^{L-1} \delta(E - E_i) \quad (5.17)$$

where E_i are the eigenvalues of a L -dimensional TB Hamiltonian matrix H .

By defining $\tilde{\rho}(\tilde{E}) = \frac{1}{L} \sum_{i=0}^{L-1} \delta(\tilde{E} - \tilde{E}_i)$ the respective scaled quantity and by inserting this function into the definition of μ_n in Eq. (5.12), one obtains:

$$\mu_n = \int_{-1}^1 \tilde{\rho}(\tilde{E}) T_n(\tilde{E}) d\tilde{E} = \frac{1}{L} \sum_{i=0}^{L-1} T_n(\tilde{E}_i) = \frac{1}{L} \sum_{i=0}^{L-1} \langle i | T_n(\tilde{H}) | i \rangle = \frac{1}{L} \text{Tr}[T_n(\tilde{H})] \quad (5.18)$$

The recursion relations (5.10) of the Chebyshev polynomials can now be used to calculate the matrix elements $\mu_n = \langle i | T_n(\tilde{H}) | i \rangle$ by applying recursively $T_n(\tilde{H})$ to the state $|i\rangle$, i.e., $|i_n\rangle = T_n(\tilde{H})|i\rangle$ in the following way:

$$\begin{aligned} |i_0\rangle &= |i\rangle, \\ |i_1\rangle &= \tilde{H}|i_0\rangle, \\ |i_{n+1}\rangle &= 2\tilde{H}|i_n\rangle - |i_{n-1}\rangle \end{aligned} \quad (5.19)$$

For the moments in particular these recursion relations give

$$\begin{aligned}
\mu_0 &= \langle i_0 | i_0 \rangle, \\
\mu_1 &= \langle i_1 | i_0 \rangle, \\
\mu_{2n} &= \langle i_n | i_n \rangle - \mu_0, \\
\mu_{2n+1} &= \langle i_{n+1} | i_n \rangle - \mu_1
\end{aligned} \tag{5.20}$$

Finally, in order to compute the traces in (5.18) we used the stochastic evaluation method [19], by which

$$Tr[T_n(\tilde{H})] \approx \frac{1}{R} \sum_{r=0}^{R-1} \langle r | T_n(\tilde{H}) | r \rangle \tag{5.21}$$

where $|r\rangle$ are random vectors defined by $|r\rangle = \sum_{j=0}^{L-1} \zeta_{rj} |j\rangle$, with j running over the atomic sites of the structure, R is the number of random vectors and $\zeta_{rj} \in \mathbb{C}$ are random functions satisfying the following statistical averages:

$$\begin{aligned}
\langle\langle \zeta_{rj} \rangle\rangle &= 0, \\
\langle\langle \zeta_{rj} \zeta_{r'j'} \rangle\rangle &= 0, \\
\langle\langle \zeta_{rj}^* \zeta_{r'j'} \rangle\rangle &= 0
\end{aligned} \tag{5.22}$$

In this work, we choose $\zeta_{rj} = e^{i\phi}$ with $\phi \in [0, 2\pi]$. It can be shown that the error over the evaluation of the traces decreases as $1/\sqrt{L \cdot R}$ [19]. Using this method we can then compute either the Total DOS (TDOS) by initializing the normalized initial wavefunctions $|i\rangle$ of Eq. (5.19) over all the sites of the structure or the Localized DOS (LDOS) by initializing the normalized initial wavefunctions over a partial number of sites on which the DOS is projected.

5.3 Results

5.3.1 Computational model of the Beltrami's surface tiling

In this section we apply the approach discussed in section 1.2 to build a real Beltrami's pseudosphere. In Fig. (5.7) we report six minimization snapshots, starting from the initial configuration shown in the top left panel 1, of a structure containing $N = 1626$ carbon atoms, where we coloured in red those not belonging to purely hexagonal faces to identify the defected sites. The initial configuration, obtained by projecting the graphene net on the Beltrami's surface, is characterized by a high level of order, where defected faces are present only in the bottom part of the pseudosphere owing to the six heptagons added to the pristine graphene cell according to

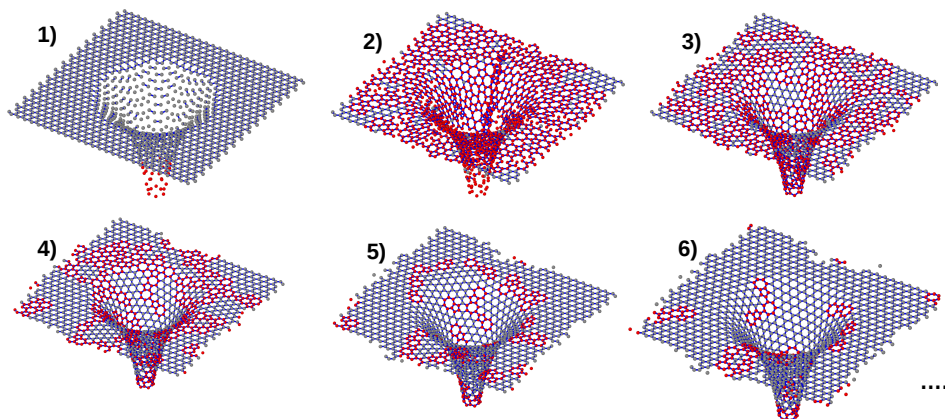


FIGURE 5.7: Optimization of a carbon pseudosphere containing 1626 atoms with radius $R_p = 18.26 \text{ \AA}$. Panels from 1) to 6) represent different optimization stages, where each move consists of a single trial switch-twist. We colour in red the carbon atoms that do not belong to the hexagonal faces. Starting from an initial configuration (panel 1) almost entirely tiled with hexagonal polygons, atoms rearrange to fill uniformly the surface reaching a local minimum after a few thousands steps (panel 6). After reaching this configuration, trial moves are increasingly rejected and the Metropolis algorithm becomes inefficient.

the step discussed in paragraph (5.2.1). In this configuration hexagonal faces clearly outnumber by far the heptagonal ones. We notice that in this initial configuration carbon-to-carbon bond lengths are generally too short in the flat region while are too long within the Beltrami's surface with respect to graphene. The carbon atoms tend to rearrange quickly after the first bond switching trial moves, which are seldom rejected. This effect is clearly visible in panel 2) of Fig. (5.7), representing the surface after about 1600 bond switches, where the number of heptagons, pentagons and hexagons becomes comparable. Further bond switching of the order of ten thousands Monte Carlo steps result into a rather stable structure, which has apparently reached a local minimum in configuration space. After reaching this configuration, trial moves are increasingly rejected and the Metropolis algorithm is inefficient being characterised by a drastically low number of accepted moves. Of course, owing to the use of a Monte Carlo algorithm, we obtain different structures from different simulations even though starting from the same initial conditions. Therefore, among the

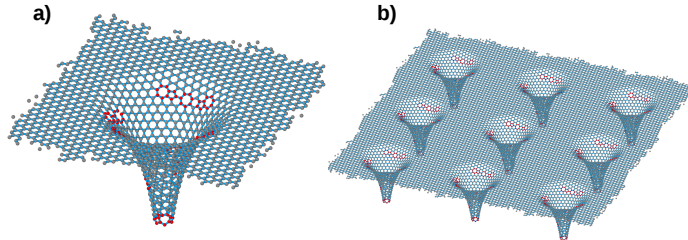


FIGURE 5.8: An example of a ‘good’ Beltrami’s structure containing $N = 1978$ carbon atoms with radius $R_p = 19.37 \text{ \AA}$ after optimization. In a) we report the simulation supercell, while in b) the 3×3 periodically repeated system.

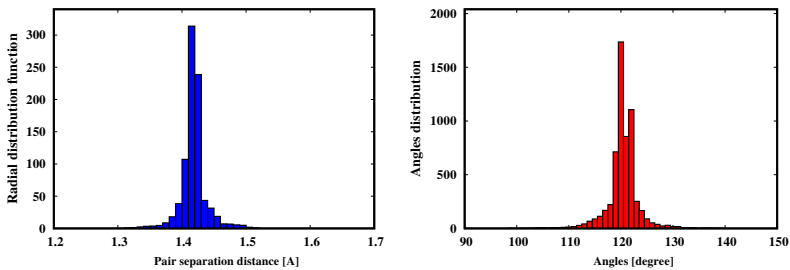


FIGURE 5.9: Pair distribution function (left panel) and angle distribution (right panel, where 120° corresponds to pristine graphene) for the structure in Fig. (5.8).

several configurations obtainable by our procedure we keep only the final structures that do not present defects on the flat region, where we expect to recover the pristine graphene net, which includes the maximum circle (the “event horizon” of the pseudosphere). In Fig. (5.8a) we show an acceptable Beltrami’s surface according to our criterion, where we observe the flat region corresponding to pristine graphene. Moreover, in Fig. (5.8b) we report also the 3×3 supercell periodically repeated along the x and y directions. Finally, in Fig. (5.9) we report the pair distribution function (left panel) and the angular distribution function (right panel). These distributions are peaked respectively at $d_0 \sim 1.42 \text{ \AA}$ and around $\theta_0 \sim 120^\circ$, which are the typical values for pristine graphene. The latter structure is characterised by 985 faces, of which 97.77% are hexagonal, 1.42% are heptagonal and only 0.81% are pentagonal.

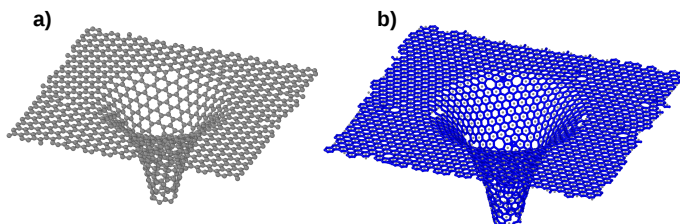


FIGURE 5.10: An example of application of the dualization algorithm: a) parent structure; b) daughter structure.

5.3.2 The dualization algorithm for three-fold coordinated graphs

In order to scale up the number of atomic centers we apply the dualization algorithm discussed in step V of section (5.2.1). Using this approach, we can increase the number of atoms by a factor of ~ 3 and the largest radius by a factor of $\sim \sqrt{3}$ after bond stretching. In Fig. (5.10) we report an example of application of our method.

Notice that the straight application of our algorithm to increase the system size conserves both the distances and the number of non-hexagonal faces passing from the parent to daughter structure, but splits the Stone–Wales defects (penta-heptagonal defects). This is clearly visible in Fig. (5.5), where after the dualization the non-hexagonal faces are not neighbouring any more. This effect is unphysical as it is known that the energetically favourable position of penta-heptagonal defects is to stick together, forming eventually chains of defects or “scars” [9]. Therefore, after the dualization procedure our strategy has been to perform further bond switching-twisting MC optimization steps, again based on the Metropolis acceptance ratio, of the atomic positions to overcome the potential energy barriers. This second stage of optimization results in a collapse of the pentagonal and heptagonal faces.

We notice that the major advantage of this approach is that allows to optimize initially a relatively small structure with a number of atoms in the range $N \in [1000, 2000]$ using only a few CPU hours of desktop machines and then to dualize the optimized structure to obtain a system with a triplicated number of atoms close to a local minimum, using again only a few CPU minutes of a desktop machine. Thus, we hasten to emphasize that all the simulations necessary to build extended Beltrami’s pseudospheres, having a number of carbon atoms in excess of a million (see e.g. Fig. (5.11)) can be carried out using only a few CPU hours in affordable commercial computer machines.

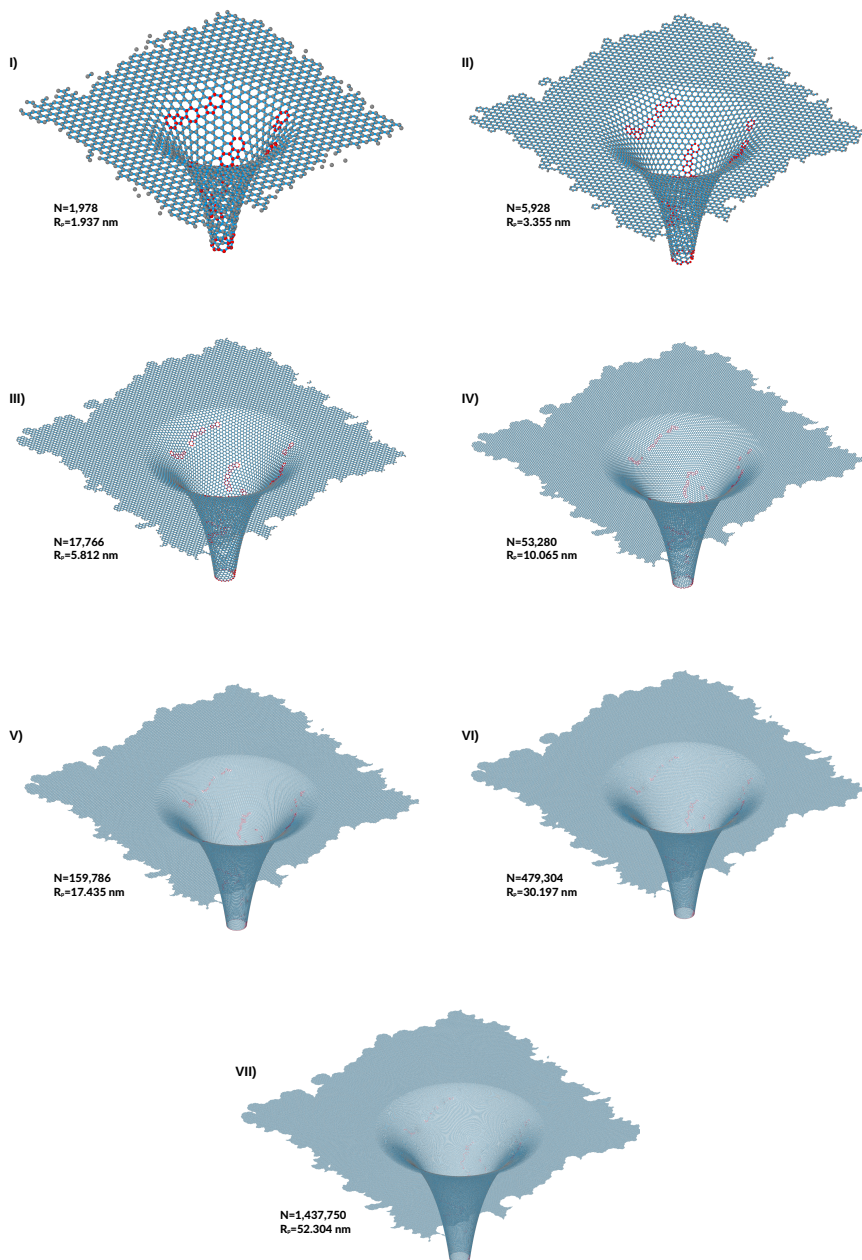


FIGURE 5.11: Example of six consecutive applications of our dualization algorithm. The starting structure is the same of Fig. (5.8a)

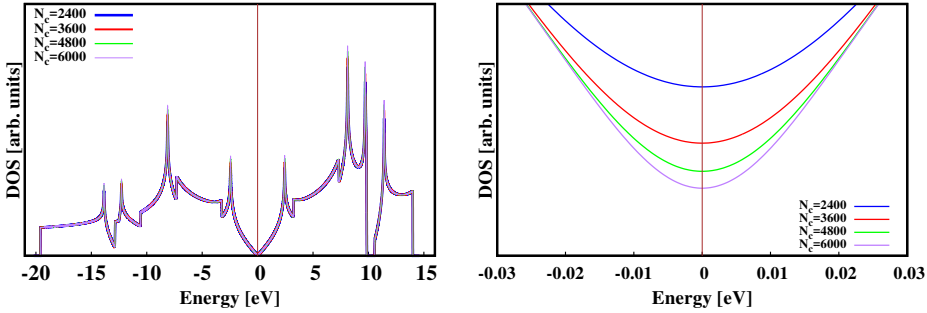


FIGURE 5.12: DOS of a graphene rectangular cell with $199.97 \text{ nm} \times 199.81 \text{ nm}$ sides, containing 1,525,188 carbon atoms for different values of the cut-off parameter N_c . In the left panel we report the full spectrum while in the right panel we zoom near the Fermi energy.

5.3.3 Density of States simulations

Planar graphene

In this section we discuss the TB simulations performed to calculate the DOS of planar graphene. This is of course a test for our newly developed code to investigate convergence properties, e.g., with respect to the number N_c of moments needed to expand the DOS, and the number of random vectors R needed for computing the matrix elements in Eq. (5.21).

First, we test the convergence of the DOS with respect to the cut-off number N_c . In the left panel of Fig. (5.12) we report the DOS in the energy range -20 to 15 eV for four different values of N_c . On this energy scale the curves calculated with N_c ranging from 2400 to 6000 are indistinguishable. However, by zooming near the Fermi level (see right panel of Fig. (5.12)) it is evident that a finer resolution of the DOS can be obtained by increasing the truncation value. The DOS of graphene indeed reproduces more closely the expected linear dispersion around the Fermi energy. In other words, by summing up more terms in Eq. (5.13) the approximate function becomes more accurate. Nevertheless, we found out that there is a threshold to the number of terms in the summation after which spurious oscillations appear in the DOS, leading to poor convergence, as can be seen in Fig. (5.13). A method for estimating the value of N_c that trades-off between accuracy and computational efficiency is reported in Ref. [21]. In this method one can track the change of an approximated function f_{approx} by modifying some parameters x and P , which in our case are represented by N_c and R , with

$$\delta_P f_{approx} = \left| \frac{f_{approx}(x, P + dP) - f_{approx}(x, P)}{f_{approx}(x, P)} \right|_{Max} \quad (5.23)$$

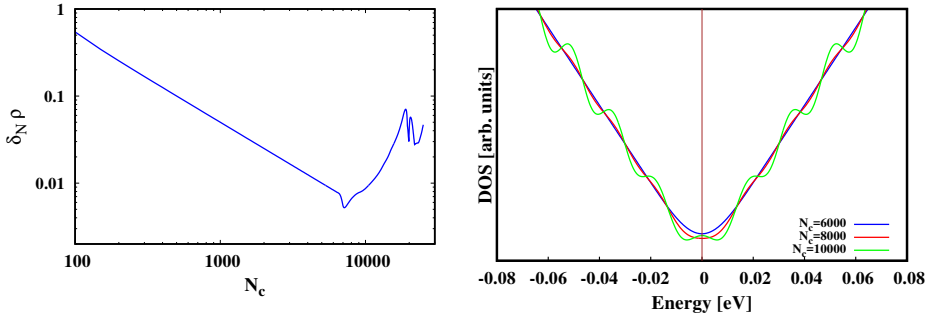


FIGURE 5.13: Left: $\delta_{N_c} \rho$ as by Eq. (5.23); the best trade-off value of N_c is found to be ≈ 6500 for this lattice containing around $1.5 \cdot 10^6$ atoms. Right: The DOS computed with $N_c = 6000$ (blue curve), 8000 (red curve), and 10000 (green curve).

In the left panel of Fig. (5.13), according to Eq. (5.23), we report the quantity $\delta_{N_c} \rho$ in the energy range $[-0.2, 0.2]$ eV, while in the right panel we show the DOS for different N_c zoomed in the energy range $[-0.03, 0.03]$ eV. This analysis shows that the “best” value of N_c to avoid numerical instabilities in the form of rapid oscillations in the spectrum without loss of accuracy is about 6500, corresponding to the value in which $\delta_{N_c} \rho$ deviates from linearity (see the left panel of Fig. (5.13)). These oscillations can be rationalized by noticing that the energy separation between levels in periodic graphene is infinitesimal and the DOS is a continuous function. At odds, in our simulations the pseudosphere is a large but finite system and the energy separation of the levels increases with respect to infinite periodic structures. Thus, a too big value of N_c may result in a KPM energy resolution marginally above the finite energy separation between levels of our finite system, leading to poor convergence [21]. The dependence of the convergence by R , which is the number of random vectors to use in Eq. (5.21), is easier since there is virtually no upper limit except the computational feasibility. Thus, one typically increases its value until spectra do not change by adding further terms to the summation. For example, a convergence test is reported in Fig. (5.14), where one can observe that the values $R = 1$ and $R = 5$ provide absolutely comparable results for a graphene lattice containing $1.5 \cdot 10^6$ carbon atoms. Thus, in this case a single initial random vector was enough to obtain a converged DOS.

Planar graphene with a single SW defect

In this section we investigate how the DOS of graphene is affected by the presence of a single Stone–Wales (SW) defect within a net of $N = 823,860$ carbon atoms. These

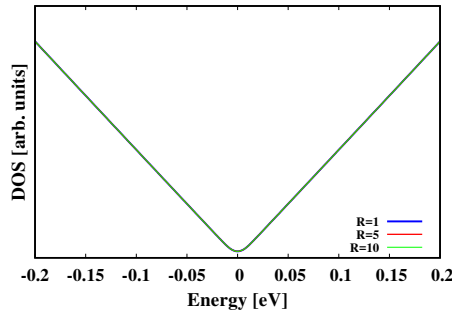


FIGURE 5.14: LDOS of graphene containing $\approx 1.5 \cdot 10^6$ atoms near the Fermi level for different values of R .

defects are indeed also present within the Beltrami's pseudosphere owing to the negative curvature. In Fig. (5.15) we report the LDOS projected over sites found at different distances from the SW defect. These calculations are carried out using $R = 100$ and $N_c = 5000$, a value that according to the formula (5.15) delivers a resolution of about 7.5 meV. In the left panel of Fig. (5.15) we observe not surprisingly that the shape of the LDOS is dramatically modified near the defect site, while far from it the graphene-like shape is recovered. It is worth to note that the presence of the SW defect still affects the LDOS projected at distances of $\approx 100 \text{ \AA}$ with small oscillations in the spectrum. In the right panel of (5.15) we zoom near the Fermi energy to search for possible symmetry breaking of the LDOS. We find that while the valence and conduction bands are significantly modified near the defects, far from it an asymmetrization of the LDOS clearly emerges in the energy range $[-0.02, 0.02] \text{ eV}$ up to a distance of $\approx 100 \text{ \AA}$.

It is also meaningful to analyse the LDOS projected over the two graphene sublattices, which are usually called A and B [1]. In Fig. (5.16) we report the two DOSs projected over the sites at the same distance ($\approx 56 \text{ \AA}$) from the single SW defect resolved for the sublattices A and B . Interestingly, we observe that the two LDOSs have a graphene-like shape but with an oscillatory behaviour in counterphase for the two sublattices. Therefore, we can safely conclude from this analysis that the fingerprint of the presence of a single SW defect in a graphene sheet, which breaks the spatial symmetry of the pristine net, is the loss of symmetric behaviour of the LDOS near the Fermi level.

Planar graphene with random SW defect density

The presence of a single SW in a graphene large area is of course unrealistic, while we aim at simulating a surface as close as possible to experimental conditions. Thus, we increased the number of SW defects, which were created randomly within the

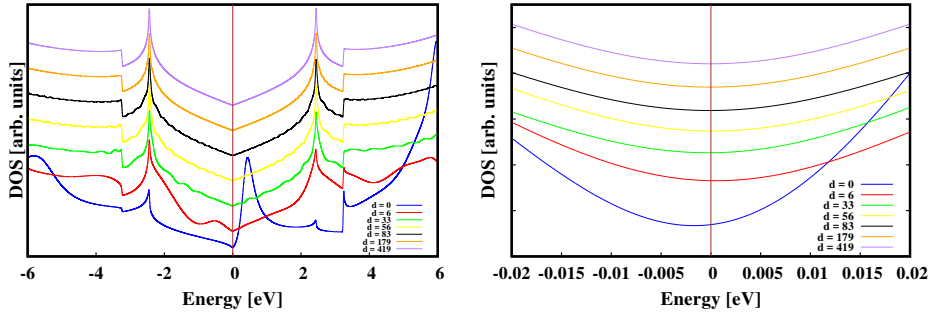


FIGURE 5.15: Left: LDOS projected over different sites of the graphene lattice for increasing distances from the single SW defect. Distances, d , are reported in Å. Right: zoom of the LDOS near the Fermi energy.

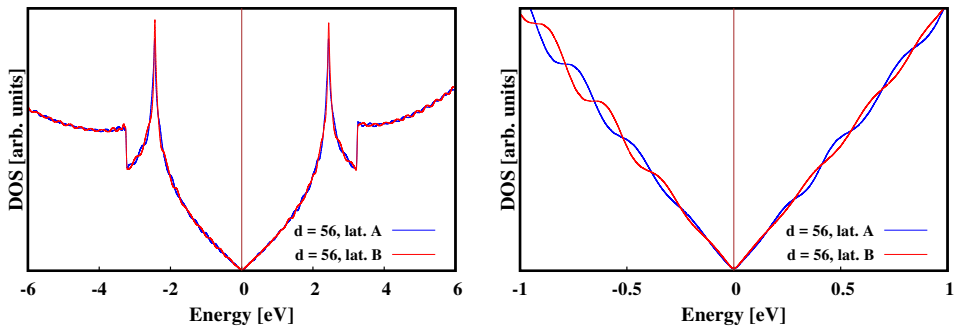


FIGURE 5.16: Left: LDOS projected at the same distance from the single SW defect over the two graphene sublattices A and B . Right: zoom of the LDOS in the range $[-1,1]$ eV.

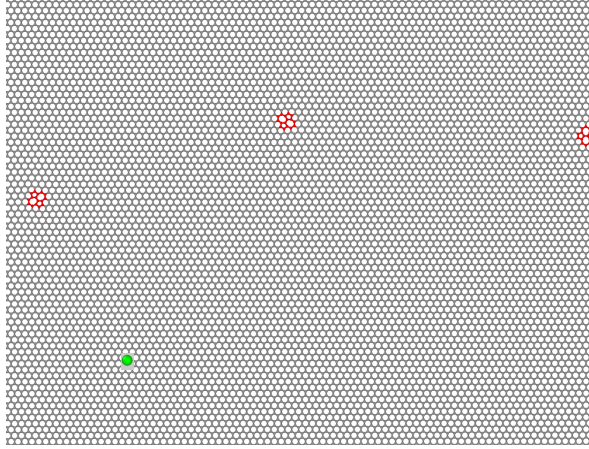


FIGURE 5.17: Supercell of graphene with 0.05% density of random SW defects. In red colour we design the atoms belonging to the SW, while the green sphere points out the atomic sites over which we project the LDOS.

graphene lattice. In this case, we calculate the DOS projection over sites positioned in both the two different sublattices. These simulations were carried out in a graphene lattice containing $N = 1,240,236$ carbon atoms, where we introduced 100 SW defects, of which a square cut is shown in Fig. (5.17). After testing the convergence parameters were set to $R = 100$ and $N_c = 6000$. In Fig. (5.18) we show the LDOS (blue and red curves) and the TDOS (black curve) of this structure. The LDOS, in particular, is plotted at a distance of approximately 100 \AA from the nearest defect site, comparable to the LDOS previously reported in Fig. (5.16). Surprisingly, here the LDOSs over the two sites belonging to the sublattices A and B have a lineshape similar to the single-defect case and to the pristine graphene (see Fig. (5.12)), but showing more noisy peaks. On the other hand, the TDOS is smoother, as the contributions of the defects averages out in this case.

Finally, we observe that an asymmetric behaviour is found again zooming the DOS near the Fermi energy (see the right panel of Fig. (5.18)).

LDOS of the extended Beltrami's pseudosphere

After having paved the way to perform the DOS computation in the Beltrami's pseudosphere by showing simulations in pristine and SW defected planar graphene, we are ready to show whether the former structure represents a condensed matter analogue of a curved spacetime. To make a Beltrami's surface, tiled with carbon atoms

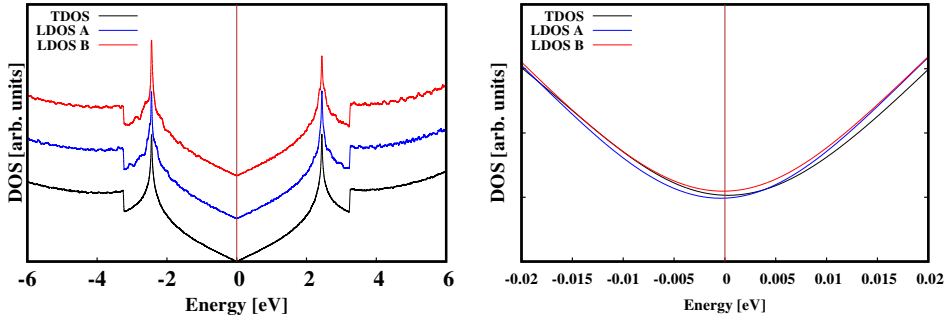


FIGURE 5.18: Left: LDOS (red and blue curves) and TDOS (black curve) of graphene with 0.05 % density of random SW defects. Right: zoom near the Fermi energy to show the asymmetric behaviour of the DOS.

in the equilibrium configuration, we use our multiscale algorithm discussed in section 1.3. The optimized Beltrami's pseudosphere of which we assess the LDOS is reported in Fig. (5.19). This structure contains $N = 2,615,976$ atoms, with a pseudosphere maximum radius of $R_p \approx 740 \text{ \AA}$. While our scale-up procedure can of course be applied recursively to obtain larger and larger structures, the only limiting factor being the computational feasibility, this pseudosphere is already enough extended to deliver suitable defect density distribution, large planar graphene area, sufficient distance between the bottom end and the "event horizon", and remarkable accuracy in terms of energy resolution of the DOS. Indeed, the natural energy scale in which the Hawking-Unruh effect should be observed is $E_r \sim \frac{l}{R_p} E_l$ where $l \approx 1.42 \text{ \AA}$ and $E_l \sim \hbar v_F / l \sim 4.63 \text{ eV}$. For $R_p \approx 740 \text{ \AA}$, we achieve an energy scale of $[-9,9] \text{ meV}$ near the Fermi energy. In this condition the Hawking temperature of this system defined by the relation [3]

$$\Theta(u, R_p) = \frac{\hbar v_F}{\kappa_B} \frac{l}{2\pi R_p^2} e^{u/R_p} \quad (5.24)$$

is around 16 K at the Hilbert horizon (where it achieves its maximum value).

The number of polygons tiling the Beltrami's surface amounts to 1,306,233 hexagonal faces, 799 heptagonal faces and 793 pentagonal faces. Pentagonal and hexagonal defects have been highlighted in Fig. (5.19) in red, while the green points show the sites over which the LDOS was eventually projected. In this regard, we have selected sites far from the defects, in order to at most avoid the noise described in the previous section close to the SW defects. Here, we aim to understand the behaviour of the LDOS moving from graphene (sites a and b), to regions in the proximity of the pseudosphere (sites c, d, e) and to regions belonging to the Beltrami's surface (sites from f

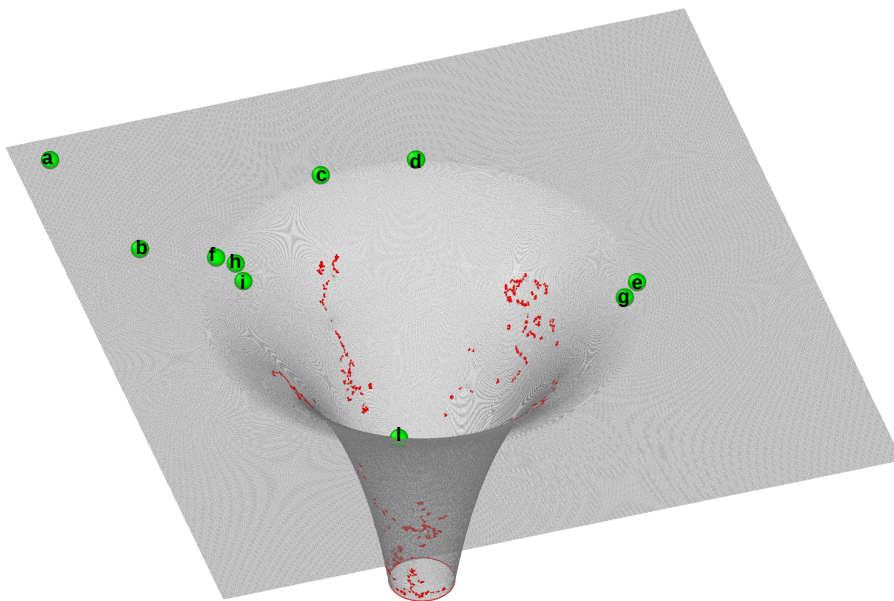


FIGURE 5.19: Beltrami's pseudosphere with a radius $R_p \approx 740$ Å . This structure contains $N = 2,615,976$ carbon atoms. In red we colour the atoms belonging to defected sites (pentagons or heptagons), while the green points highlight the sites over which we project the LDOS.

to l).

We notice that in evaluating the DOS in the curved Beltrami's surface, at odds with planar graphene, we deal with two concurring types of effects, both breaking the graphene symmetry: the proper defects, given by the non-hexagonal faces, and the spatial curvature. Indeed, while the influence of defected sites on the LDOS has been already investigated in planar graphene, in the case of the Beltrami's pseudosphere their contribution to valence and conduction states is cumbersome as the lattice spacing between carbon atoms is not as regular as in graphene; furthermore, we stress the fact that the presence of non-hexagonal defects is the consequence of a constant negative spatial curvature (as much as the presence of a constant positive curvature induces pentagonal faces in fullerene). In this sense curvature and defects are intimately related via the Gauss-Bonnet theorem, which links topology (curvature)

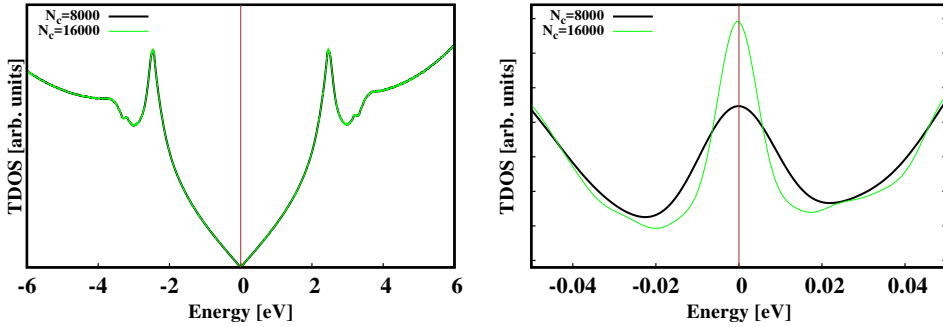


FIGURE 5.20: Left: TDOS of the graphene pseudosphere reported in Fig. (5.19) for $N_c = 8000$ (black curve) and $N_c = 16000$ (green curve). Right: zoom of the TDOS near the Fermi energy.

with the number of defected faces, and one cannot really disentangle their respective contribution to the LDOS. Thus, the LDOS lineshape in curved graphene can be considered as the result of the two overlapping effects of curvature and defects [22].

In Fig. (5.20) we show the TDOS of the Beltrami's structure plotted in Fig. (5.19) for two values of the cut-off parameter, that is $N_c = 8000$, leading to an energy resolution of 0.0058 eV, and $N_c = 16000$, leading to an energy resolution of 0.0029 eV. Looking at the left panel one might conclude incorrectly that 8000 moments (see Eq. (5.13)) are enough to get a well-resolved TDOS. However, by zooming near the Fermi energy, which we report in the right panel of Fig. (5.20), the width of the peak around 0 eV narrows by increasing the number of moments to 16,000. In general, we find that the shape of the TDOS in this energy range is similar to that one of graphene (see Fig. (5.12)), showing two symmetric peaks of the valence and conduction bands, respectively. The main difference is found in the energy range near 0 eV, where an asymmetric behaviour due to the emergence of a small peak is detected. We attribute the latter behaviour to the entangled interplay between the negative spatial curvature of our structure and to the presence of heptagonal defects.

The same behaviour can be recovered in the LDOS projected over different circumferences of the pseudosphere, as shown in Fig. (5.21).

This issue can be discussed more exhaustively by showing the LDOS over single sites of the structure. Indeed, in Figs. (5.22) and (5.23) we show the LDOS projected over the green-coloured sites of Fig. (5.19) for two different values of the cutoff parameter, that is $N_c = 8,000$ and $N_c = 16,000$ for better resolution, respectively. In both cases, we projected over two neighbour sites belonging, at least in the flat region out of the pseudosphere, to the two sublattices A and B of graphene.

We notice that the loss of spatial symmetry induced by deforming planar graphene

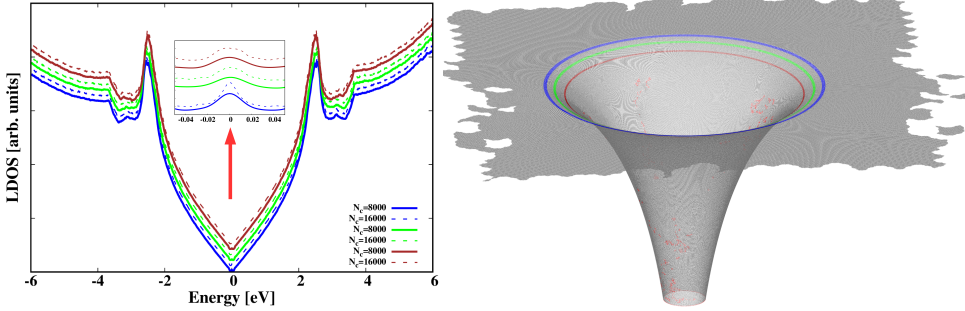


FIGURE 5.21: Left: LDOS of the graphene pseudosphere reported in Fig. (5.19) for $N_c = 8000$ (continuous curve) and $N_c = 16000$ (dashed curve), projected over the pseudosphere circumferences highlighted on the right.

into the pseudosphere shape, which leads forcibly to the formation of heptagonal defects to sustain the negative curvature, is reflected into the symmetry breaking of the LDOS over the two sublattices of graphene. While it does not make any sense to identify the sublattices A and B in the pseudosphere region, where this concept is rigorously inevitably lost, nevertheless in the outer region of the pseudosphere, characterised by the presence of pristine planar graphene (5.19), we can still disentangle the contribution of the two sublattices. For example, in the site a , which is $\approx 700 \text{ \AA}$ far from the defected region within the pseudosphere, one could guess that a graphene-like shape of the LDOS should be recovered. However, looking at the LDOS over the two neighbour atoms (see Fig. (5.22a)) we find that near 0 eV (Fermi energy) a small bump appears in the sublattice B. Moreover, we notice that the DOS is symmetric in this site. We rationalize this different behaviour of the two sublattices as due to the presence of a strong deformation induced by the Beltrami's pseudosphere also in the outer region, which substantially breaks the spatial symmetry [22]. In Fig. (5.22b), at the sites $\approx 240 \text{ \AA}$ far from the pseudosphere surface we observe a marginally sharper difference between the two sublattices (see Fig. (5.22a)), reinforcing this view.

5.3.4 Is the Beltrami's pseudosphere a condensed matter analogue of a black-hole?

In this final section we compare our results with the theoretical predictions by Iorio *et al.* [3] concerning the hypothesis that the Beltrami's pseudosphere can be regarded a condensed matter analogue of a black-hole and, thus, realizes a realistic analogue of a quantum field in curved spacetimes. The authors claim in particular that by solving

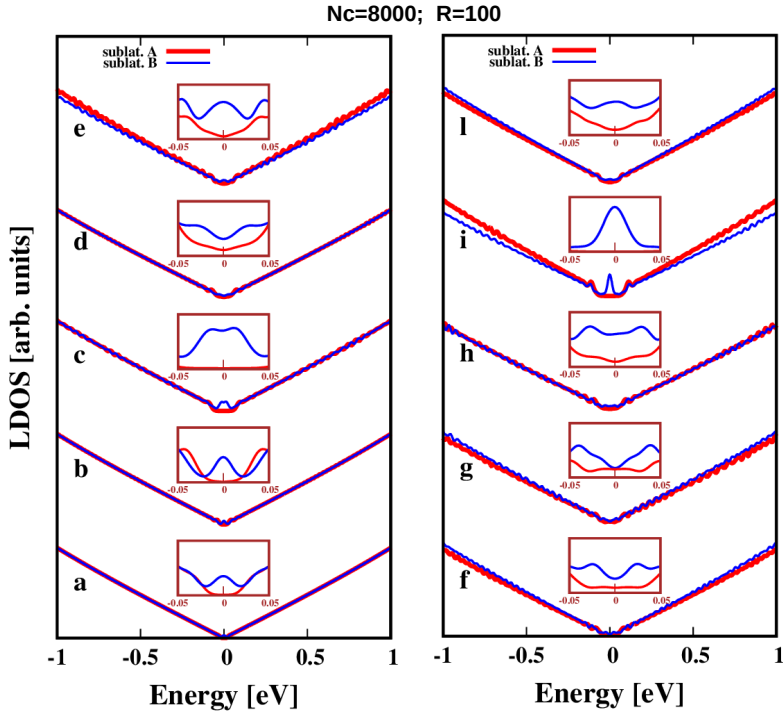


FIGURE 5.22: LDOS of the Beltrami's pseudosphere projected over the green-coloured sites of Fig. (5.19). The LDOS at each site was computed by projecting over two neighbour sites belonging, at least in the flat region out of the pseudosphere, to the two sublattices A and B of graphene. In the insets of each panel we report the LDOS close to the Fermi energy to zoom in the different behaviour of the two sublattices. These LDOSs were computed using a cut-off parameter $N_c = 8000$ and $R = 100$.

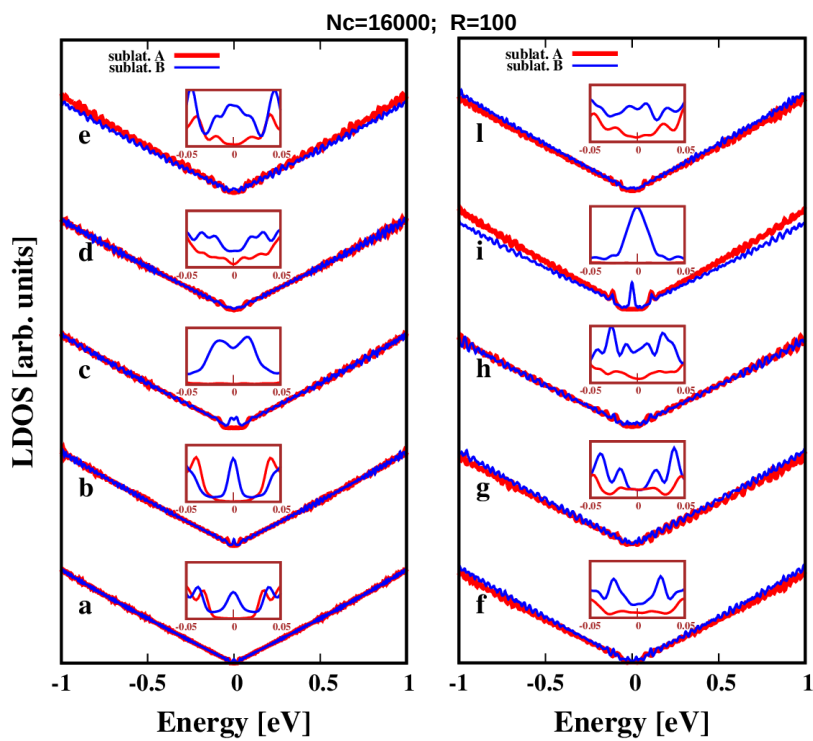


FIGURE 5.23: Same as in Fig. (5.22) but for $N_c = 16,000$ and $R = 100$.

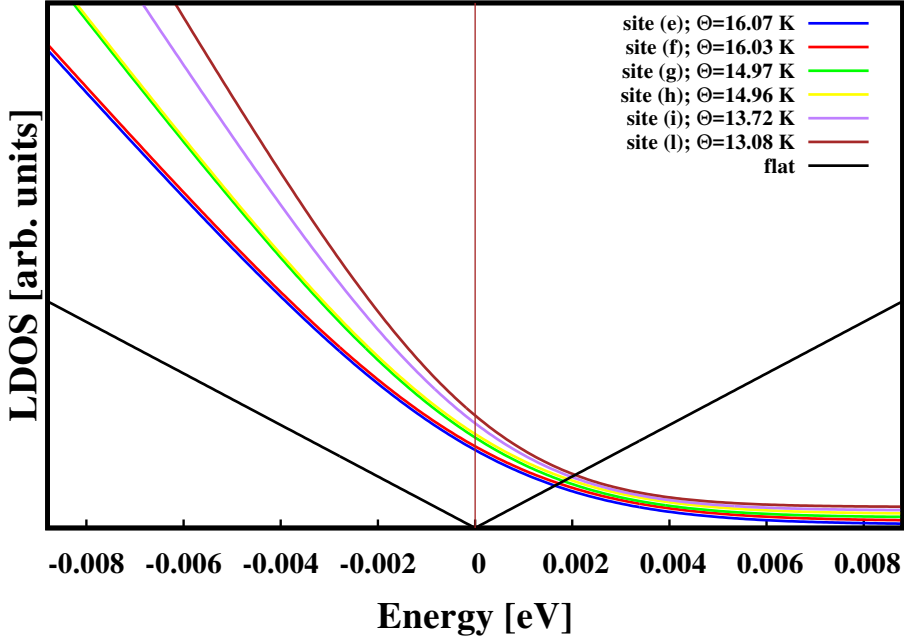


FIGURE 5.24: Shape of LDOS predicted over the sites of the Beltrami pseudosphere structure given in Fig. (5.19) by (5.25).

the Dirac equation in a curved continuum, the relevant LDOS, which can be used to test the physics of the Hawking-Unruh effect, has the following analytical form:

$$\rho^{IL}(E, u, R_p) = \frac{4}{\pi} \frac{1}{(\hbar v_F)^2} \frac{R_p^2}{l^2} e^{-2u/R_p} \frac{E}{e^{\frac{E}{\kappa_B \Theta(u, R_p)}} - 1} \quad (5.25)$$

where $v_F \approx \frac{c}{300}$ and u is the coordinate running over the Beltrami's surface related to the cartesian coordinates by $r(u) = \text{const} \cdot e^{u/R_p}$, with $r(u)$ the distance of a point on the Beltrami's surface from the rotational symmetry axis. The phenomena we are interested in occur near the horizon [3]. For example, the maximum value of the Hawking temperature is reached at the Hilbert (or event) horizon $\Theta(R_p \cdot \ln(R_p/l), R_p) = \frac{\hbar v_F}{\kappa_B 2\pi R_p}$ (see Eq. (5.24)).

For the Beltrami's pseudosphere shown in Fig. (5.19) we find a Hawking temperature of about 13 K, while the Hawking temperatures for the sites over which we project the LDOS on the pseudosphere surface (sites e to l) range from 13.72 K (site i) to 16.07 K (site e).

In Fig. (5.24) we report the LDOS over the green-coloured sites of Fig. (5.19) predicted by using the analytical formula (5.25). The exponential behaviour shown in Fig. (5.24) is derived in the continuum approximation and by ignoring elastic effects [2, 3], owing to the long wavelength excitations near the Fermi energy. On the other hand, in our computational model we cannot neglect the elastic effects induced by the curvature (or, which the same, by the defects) on the LDOS over the two sublattices of graphene. Thus, the comparison between our numerical results with the analytical predictions is non-trivial. Furthermore, our resolution is limited by two factors: the maximum number of recursion step, and the resolution achievable in the energy range $[-9,9]$ meV (which was ~ 3 meV in the case of $N_c = 16000$).

In Fig. (5.25) we zoom in the energy range $[-8,8]$ meV the LDOS projected over the same sites of the Beltrami's surface used in Figs. (5.22,5.23). The LDOS in the site (a) (flat case) is reported in both panels to have a "standard" for comparison. *A* and *B* in Fig. (5.25) label again the two neighbour sites belonging to the two different sublattices of graphene. We notice that the asymmetric exponential behaviour found in the analytical model, under the continuum approximation and neglecting elastic effects due to the heptagonal defects, is also reproduced in our realistic numerical simulations. In view of these results, we conclude that the Beltrami's pseudosphere may represent a valid analogue of a black-hole in the meaning explained above and, in this respect, we feel that the actual forging of the carbon pseudosphere in a lab should be pursued as well as the experimental measurements of the LDOS either by low temperature STM or optical near-field spectroscopy.

5.4 Conclusions

This chapter was aimed at discussing the modeling of a novel carbon-based allotrope having the shape of the Beltrami's pseudosphere. We have first demonstrated that this computational model can be achieved by tiling the surface with pentagonal, hexagonal and heptagonal polygons and that can be scaled up efficiently to dimensions useful to probe several properties by experiments (millions of atoms). Furthermore, we tackled also the problem of computing the electronic properties of this extended system. As this size is out of reach for ab-initio techniques, we used a tailored tight-binding approach, by which we were able to reproduce correctly graphene properties. Furthermore, we used the Kernel Polynomial Method to obtain accurate numerical LDOS and TDOS, to be compared with the analytical LDOS behaviour predicted in curved continuum. Notably, we find an asymmetric shape of the LDOS similar to the theoretical predictions, which can be the signature of the Hawking-Unruh effect in a condensed matter analogue of a black-hole. While in our model we cannot avoid the presence of topological defects and thus of elastic effects not present in the purely analytical calculation, which may produce some numerical noise in our

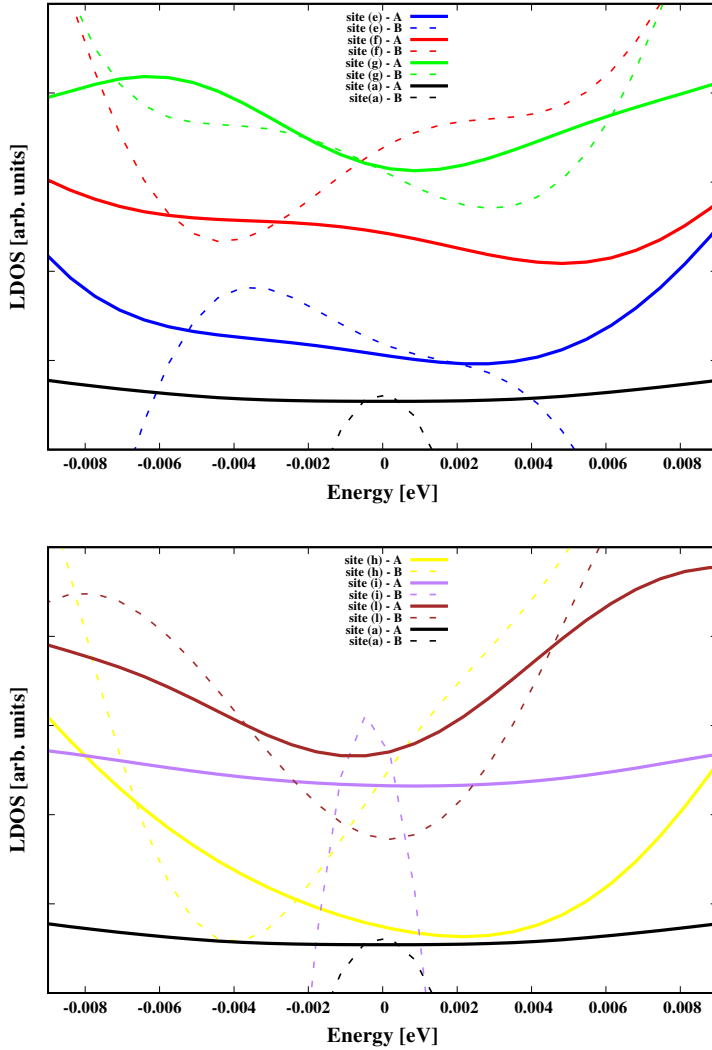


FIGURE 5.25: Zoom of the LDOS computed over the sites of the Beltrami's pseudosphere of Fig. (5.19). Top panel: sites e, f, g, a. Bottom panel: sites h, i, l. *A* and *B* label the two neighbour sites belonging to the two different sublattices of graphene. The LDOS in the site (a) (flat case) is reported in both panels to have a "standard" for comparison.

simulations, nevertheless we are rather confident that our simulations point towards a condensed matter analogue of a black-hole.

Bibliography

- [1] A. H. Castro Neto, F. Guinea, N. M. R. Peres, K. S. Novoselov, A. K. Geim, The electronic properties of graphene, *Rev. Mod. Phys.* 81 (2009) 109–162. doi:10.1103/RevModPhys.81.109.
URL <https://link.aps.org/doi/10.1103/RevModPhys.81.109>
- [2] A. Iorio, G. Lambiase, The hawking-unruh phenomenon on graphene, *Physics Letters B* 716 (2) (2012) 334 – 337. doi:10.1016/j.physletb.2012.08.023.
URL <http://www.sciencedirect.com/science/article/pii/S037026931200860X>
- [3] A. Iorio, G. Lambiase, Quantum field theory in curved graphene spacetimes, lobachevsky geometry, weyl symmetry, hawking effect, and all that, *Phys. Rev. D* 90 (2014) 025006. doi:10.1103/PhysRevD.90.025006.
URL <https://link.aps.org/doi/10.1103/PhysRevD.90.025006>
- [4] M. Bowick, A. Cacciuto, D. R. Nelson, A. Travesset, Crystalline order on a sphere and the generalized thomson problem, *Phys. Rev. Lett.* 89 (2002) 185502. doi:10.1103/PhysRevLett.89.185502.
URL <https://link.aps.org/doi/10.1103/PhysRevLett.89.185502>
- [5] C60: Buckminsterfullerene, *Nature* 318 (1985) 162. doi:10.1038/318162a0.
URL <https://doi.org/10.1038/318162a0>
- [6] S. Taioli, G. Garberoglio, S. Simonucci, S. a. Beccara, L. Aversa, M. Nardi, R. Verucchi, S. Iannotta, M. Dapor, D. Alfe', Non-adiabatic ab initio molecular dynamics of supersonic beam epitaxy of silicon carbide at room temperature, *The Journal of chemical physics* 138 (4) (2013) 044701.
- [7] R. Verucchi, L. Aversa, M. V. Nardi, S. Taioli, S. a Beccara, D. Alfe', L. Nasi, F. Rossi, G. Salviati, S. Iannotta, Epitaxy of nanocrystalline silicon carbide on si (111) at room temperature, *Journal of the American Chemical Society* 134 (42) (2012) 17400–17403.
- [8] L. Aversa, S. Taioli, M. V. Nardi, R. Tatti, R. Verucchi, S. Iannotta, The interaction of c₆₀ on si(111) 7 × 7 studied by supersonic molecular beams: interplay between precursor kinetic energy and substrate temperature in surface activated processes, *Frontiers in Materials* 2 (2015) 46.

- [9] S. Taioli, R. Gabbrielli, S. Simonucci, N. M. Pugno, A. Iorio, Lobachevsky crystallography made real through carbon pseudospheres, *Journal of Physics: Condensed Matter* 28 (13) (2016) 13LT01.
URL <http://stacks.iop.org/0953-8984/28/i=13/a=13LT01>
- [10] F. Wooten, K. Winer, D. Weaire, Computer generation of structural models of amorphous si and ge, *Phys. Rev. Lett.* 54 (1985) 1392–1395. doi:10.1103/PhysRevLett.54.1392.
URL <https://link.aps.org/doi/10.1103/PhysRevLett.54.1392>
- [11] E. Bitzek, P. Koskinen, F. Gähler, M. Moseler, P. Gumbsch, Structural relaxation made simple, *Phys. Rev. Lett.* 97 (2006) 170201. doi:10.1103/PhysRevLett.97.170201.
URL <https://link.aps.org/doi/10.1103/PhysRevLett.97.170201>
- [12] A. Kumar, M. Wilson, M. F. Thorpe, Amorphous graphene: a realization of zachariasen’s glass, *Journal of Physics: Condensed Matter* 24 (48) (2012) 485003.
URL <http://stacks.iop.org/0953-8984/24/i=48/a=485003>
- [13] H. Gould, J. Tobochnik, W. Christian, *An introduction to computer simulation methods*.
- [14] S. Alfthan, *Computational studies of silicon interfaces and amorphous silica* (2006).
URL <http://urn.fi/urn:nbn:fi:tkk-008820>
- [15] J. C. Slater, G. F. Koster, Simplified lcao method for the periodic potential problem, *Phys. Rev.* 94 (1954) 1498–1524. doi:10.1103/PhysRev.94.1498.
URL <https://link.aps.org/doi/10.1103/PhysRev.94.1498>
- [16] S. Yuan, M. Rösner, A. Schulz, T. O. Wehling, M. I. Katsnelson, Electronic structures and optical properties of partially and fully fluorinated graphene, *Phys. Rev. Lett.* 114 (2015) 047403. doi:10.1103/PhysRevLett.114.047403.
URL <https://link.aps.org/doi/10.1103/PhysRevLett.114.047403>
- [17] T. Stauber, J. I. Beltran, J. Schliemann, Tight-binding approach to pentagraphene, *Scientific Reports* 6 (2016) 22672. doi:10.1038/srep22672.
URL <https://doi.org/10.1038/srep22672>
- [18] P. Giannozzi, S. Baroni, N. Bonini, M. Calandra, R. Car, C. Cavazzoni, D. Ceresoli, G. L. Chiarotti, M. Cococcioni, I. Dabo, A. D. Corso, S. de Gironcoli, S. Fabris, G. Fratesi, R. Gebauer, U. Gerstmann, C. Gougoussis, A. Kokalj, M. Lazzeri, L. Martin-Samos, N. Marzari, F. Mauri, R. Mazzarello, S. Paolini, A. Pasquarello, L. Paulatto, C. Sbraccia, S. Scandolo, G. Sclauzero, A. P. Seitsonen, A. Smogunov, P. Umari, R. M. Wentzcovitch, *Quantum espresso: a modular*

- and open-source software project for quantum simulations of materials, *Journal of Physics: Condensed Matter* 21 (39) (2009) 395502.
URL <http://stacks.iop.org/0953-8984/21/i=39/a=395502>
- [19] A. Weiße, G. Wellein, A. Alvermann, H. Fehske, The kernel polynomial method, *Rev. Mod. Phys.* 78 (2006) 275–306. doi:10.1103/RevModPhys.78.275.
URL <https://link.aps.org/doi/10.1103/RevModPhys.78.275>
- [20] L. Torres, S. Roche, J. Charlier, *Introduction to Graphene-Based Nanomaterials: From Electronic Structure to Quantum Transport*, Cambridge University Press, 2014.
URL <https://books.google.it/books?id=bbGkAgAAQBAJ>
- [21] J. Garcia, The kernel polynomial method for quantum transport in disordered systems, Ph.D. thesis (06 2015). doi:10.13140/RG.2.2.23655.14244.
- [22] M. Schneider, D. Faria, S. Viola Kusminskiy, N. Sandler, Local sublattice symmetry breaking for graphene with a centro-symmetric deformation, <http://arxiv.org/abs/1501.02981> 91. doi:10.1103/PhysRevB.91.161407.

Chapter 6

Future works

To outline some possible future directions towards my post-doctoral studies, in this chapter we discuss a challenging investigation that we tackled at the end of my PhD. Thus, the following description is not in its final form, but still needs significant further investigations. This work concerns the computer simulation of a process in which an 8 keV X-ray beam impinges on an amorphous SiO_2 sample. In particular, our goal is to study how the light-matter interaction affects the sample at the atomic level with an emphasis on possible atomic displacements possibly due to bond breaking. This problem has been proposed by the experimental group of Prof. G. Monaco (University of Trento). In their measurements, performed at the ESRF synchrotron light source in France, they observe a local modification of the samples in terms of atomic displacements of as much as tens of atoms. The key quantity to assess this displacement is the so-called scattering function $F_s(q, \tau)$, which will be defined below. On the theoretical side, the basic issues that we wish to investigate by computer simulations are the following: i) do the atoms shift their positions only near the interaction site or in overall the sample, due to the presence of secondary electrons and photons emitted inside the material after the absorption of the X-ray photons? ii) What is the fundamental reason of this local modification of the atomic arrangement?

From the computational point of view, this is a very tricky problem to solve. Indeed, after X-ray scattering, photo-emitted core electrons of silicon or oxygen atomic centres travel within the sample, releasing their kinetic energy by exciting other electrons (secondary electrons). This leads to further de-excitation mechanisms, including both electrons and photons. Of course we are not able to simulate all the processes occurring after the initial the X-ray absorption. However, using the approach presented in the second chapter we can follow, by computing the electron inelastic mean free path in SiO_2 , the electron trajectories as a function of their energy prior stopping. Knowing this observable, one can guess that after a transient in which the electrons release the majority of their kinetic energy within the sample, the system reaches a state in which only low-energy electrons or photons are present in thermal

equilibrium with the sample. This is the starting point of our simulations.

In order to describe the after-scattering mechanisms we use a Non Adiabatic Molecular Dynamics approach, which allows us to investigate the coupling between nuclear and electronic degrees of freedom during the dynamical simulation of the system. These simulations were performed by the CPMD code suite [1], which implements this model. In particular, we studied three different structures of SiO₂: the quartz, an “ideal” amorphous geometry where the atoms are fully coordinated and do not have dangling bonds, and finally a defected amorphous geometry, where a few atoms have some dangling bonds. While the quartz structure is well known, the latter two geometries were obtained by Molecular Dynamics simulations.

6.1 Theory of Non Adiabatic Molecular Dynamics

Shortly, we sketch the non-adiabatic Molecular Dynamics (NAMD) approach [2]. Within this framework, to follow the system dynamics one has to solve the time-dependent Schrödinger equation, which in atomic units reads:

$$i \frac{\partial}{\partial t} \Psi(\{\mathbf{r}_i\}, \{\mathbf{R}_I\}; t) = \mathcal{H} \Psi(\{\mathbf{r}_i\}, \{\mathbf{R}_I\}; t) \quad (6.1)$$

where $\{\mathbf{r}_i\}$ and $\{\mathbf{R}_I\}$ are the electronic and nuclear degrees of freedom. The Hamiltonian of the system can be written:

$$\mathcal{H} = - \sum_I \frac{1}{2M_I} \nabla_I^2 - \frac{1}{2} \sum_i \nabla_i^2 + V_{n,e}(\{\mathbf{r}_i\}, \{\mathbf{R}_I\}) \quad (6.2)$$

where (6.3)

$$V_{n,e}(\{\mathbf{r}_i\}, \{\mathbf{R}_I\}) = \sum_{i < j} \frac{1}{|\mathbf{r}_i - \mathbf{r}_j|} - \sum_{i,I} \frac{Z_I}{|\mathbf{R}_I - \mathbf{r}_i|} + \sum_{I < J} \frac{Z_I Z_J}{|\mathbf{R}_I - \mathbf{R}_J|} \quad (6.4)$$

The total Hamiltonian \mathcal{H} can be split as a sum of two terms, which are functions of the electronic and nuclear degrees of freedom respectively as follows $\mathcal{H} = - \sum_I \frac{1}{2M_I} \nabla_I^2 + \mathcal{H}_e(\{\mathbf{r}_i\}, \{\mathbf{R}_I\})$. The second term depends parametrically on the nuclear coordinates. A possible ansatz for the total wave-function is

$$\Psi(\{\mathbf{r}_i\}, \{\mathbf{R}_I\}; t) \approx \Phi(\{\mathbf{r}_i\}; t) \chi(\{\mathbf{R}_I\}; t) \cdot \exp \left[i \int_{t_0}^t \langle \Psi(t') | \mathcal{H}_e | \Psi(t') \rangle dt' \right] \quad (6.5)$$

where the nuclear (χ) and electronic (Φ) contributions are factorised and the phase factor is added for later convenience. This approximation for the total wave-function is called single-configuration ansatz [2] and leads to a mean-field description of the dynamics, also called Ehrenfest dynamics. Indeed, inserting (6.5) into Eqs. (6.1), (6.2), after multiplication from the left by Φ^* and χ^* and integration over all the nuclear

and electronic coordinates, one can obtain the following system of coupled equations by imposing the conservation of the total energy $\frac{d\langle\mathcal{H}\rangle}{dt} = 0$:

$$i\frac{\partial}{\partial t}\Phi = -\frac{1}{2}\sum_i\nabla_i^2\Phi + \left[\int\chi^*(\{\mathbf{R}_I\};t)V_{n,e}(\{\mathbf{r}_i\},\{\mathbf{R}_I\})\chi(\{\mathbf{R}_I\};t)d\mathbf{R}\right]\Phi \quad (6.6)$$

$$i\frac{\partial}{\partial t}\chi = -\sum_I\frac{1}{2M_I}\nabla_I^2\chi + \left[\int\Phi^*(\{\mathbf{r}_i\};t)\mathcal{H}_e(\{\mathbf{r}_i\},\{\mathbf{R}_I\})\Phi(\{\mathbf{r}_i\};t)d\mathbf{r}\right]\chi \quad (6.7)$$

where electrons and nuclei move in a time-dependent averaged mean-field potential created respectively by nuclei and electrons. The method to extract semiclassical mechanics for nuclei is given by writing the χ wavefunction in terms of an amplitude A and a phase factor S :

$$\chi(\{\mathbf{R}_I\};t) = A(\{\mathbf{R}_I\};t)e^{iS(\{\mathbf{R}_I\};t)} \quad (6.8)$$

By inserting Eq. (6.8) into Eq. (6.7), one obtains after some algebra two coupled equations for the modulus and the phase factor of the nuclear wavefunctions [2]. The equation for the amplitude A can be rationalized as a continuity equation for the current [2], while the equation for the phase factor S , defining $\mathbf{P}_I = \nabla_I S$ and taking the classical limit $\hbar \rightarrow 0$, leads to a Newton equation of motion for the nuclei:

$$\begin{aligned} \frac{d\mathbf{P}}{dt} &= -\nabla_I \int \Phi^* \mathcal{H}_e \Phi d\mathbf{r} \\ \text{or } M_I \frac{d^2\mathbf{R}_I}{dt^2} &= -\nabla_I V_e^E(\{\mathbf{R}_I(t)\}) \end{aligned} \quad (6.9)$$

Equations (6.9) clearly describe nuclei moving according to classical mechanics where the potential V_e^E is called the Ehrenfest potential and it is obtained by solving the time dependent Schrödinger equation (6.6).

At this point also the nuclei in Eq. (6.6) can be approximated as classical point particles. By replacing the nuclear density $|\chi(\{\mathbf{R}_I\};t)|^2$ in the limit $\hbar \rightarrow 0$ by a product of delta functions $\prod_I \delta(\mathbf{R}_I - \mathbf{R}_I(t))$ centered at the instantaneous positions $\{\mathbf{R}_I(t)\}$ of the classical nuclei

$$\int \chi^*(\{\mathbf{R}_I\};t)\mathbf{R}_I\chi(\{\mathbf{R}_I\};t)d\mathbf{R} \rightarrow \mathbf{R}_I(t) \text{ for } \hbar \rightarrow 0 \quad (6.10)$$

one obtains finally the following equations:

$$\begin{aligned}
M_I \ddot{\mathbf{R}}_I(t) &= -\nabla \int \Phi^* \mathcal{H}_e \Phi d\mathbf{r} = -\nabla_I \langle \mathcal{H}_e \rangle \\
i \frac{\partial \Phi}{\partial t} &= \left[-\frac{1}{2} \sum_i \nabla_i^2 + V_{n,e}(\{\mathbf{r}_i\}, \{\mathbf{R}_I(t)\}) \right] \Phi = \mathcal{H}_e \Phi
\end{aligned} \tag{6.11}$$

This is a coupled set of quantum/classical equations that must be solved simultaneously. The assessment of the potential energy surface is avoided by solving the time-dependent electronic Schrödinger equation “on-the-fly”, as the nuclei are propagated using classical mechanics.

The equations of motion corresponding to Eq. (6.11) can be expressed by representing the electronic wave-function Φ in terms of the instantaneous adiabatic electronic states

$$\mathcal{H}_e(\{\mathbf{r}_i\}, \{\mathbf{R}_I\}) \Phi_k = E_k(\{\mathbf{R}_I\}) \Phi_k(\{\mathbf{r}_i\}, \{\mathbf{R}_I\}) \tag{6.12}$$

and the time dependent expansion coefficients deriving from the following expression for the wave function

$$\Phi(\{\mathbf{r}_i\}, \{\mathbf{R}_I\}; t) = \sum_{l=0}^{\infty} c_l(t) \Phi_l(\{\mathbf{r}_i\}, \{\mathbf{R}_I\}) \tag{6.13}$$

The coefficients $\{c_l\}$ satisfy $\sum_l |c_l(t)|^2 = 1$ and describe the time evolution of the different states labeled by l . In this way the Ehrenfest dynamic can be expressed by

$$\begin{aligned}
M_I \ddot{\mathbf{R}}_I(t) &= -\nabla_I \sum_k |c_k(t)|^2 E_k = \\
&= -\sum_k |c_k(t)|^2 \nabla_I E_k + \sum_{k,l} c_k^* c_l (E_k - E_l) \mathbf{d}_I^{kl} \\
i\hbar \dot{c}_k(t) &= c_k(t) E_k - i\hbar \sum_l c_l(t) D^{kl}
\end{aligned} \tag{6.14}$$

where the non-adiabatic coupling elements are given by

$$D^{kl} = \int \Phi_k^* \frac{\partial}{\partial t} \Phi_l d^3r = \sum_I \dot{\mathbf{R}}_I \int \Phi_k^* \nabla_I \Phi_l d^3r = \sum_I \dot{\mathbf{R}}_I \mathbf{d}_I^{kl} \tag{6.15}$$

Eqs. (6.14) include rigorously non-adiabatic transitions between different electronic states Φ_k and Φ_l within the framework of the classical nuclear dynamics and the mean-field approximation (6.5) to the coupled problem.

Here we make use of Tully molecular dynamics where the non-adiabatic effects are taken into account with a ‘fewest switches’ surface-hopping algorithm. More details about this approach can be found in [2].

6.2 Partial results for different allotropes of SiO₂

We remind that our aim is to study the role that the electronic excitations might play in the dynamics of SiO₂ samples hit by hard X-rays in order to interpret the experimentally observed collective displacements of atoms. Thus, our model of this scattering process is that, after X-ray photoionization, the sample thermalizes by exchanging energy between electronic and nuclear degrees of freedom. To better understand the role of non-adiabatic terms we performed both ground-state (adiabatic) and excited-state (non-adiabatic) ab-initio simulations. Of course, it is clear that this physical model cannot fully follow the atomic displacements, not to mention the bond breaking, upon X-ray irradiation of the sample.

CPMD is a Pseudo Potential (PP) code, i.e. calculates electronic properties of structures using effective potentials which lead to a reduction of the number of electrons in the system. In particular, simulations were performed using a norm-conserving PP (GO-BLYP type) with a cut-off of 90 Ry. This PP is able to reproduce both the experimental bond lengths between Si and O atoms (1.6 Å) and the band-gap (around 5 eV) in the 'ideal structure'. The basis set is given by plane waves and periodic boundary conditions are used. We studied in particular three different types of cells, reported in Fig. (6.1). These simulation cells have all 72 atoms, while they reproduce the quartz structure ('crystal structure'); amorphous phase without the presence of dangling bonds, i.e. each O atom displays two bonds while each Si has four bonds ('ideal structure'); amorphous phase showing some degree of dangling bonds ('defected structure'). In this way, we are able to compare the behaviour of different electronically excited SiO₂ architectures and to investigate their relevant relaxation dynamics.

MD simulations follow the ion trajectories, from which one can extract relevant observables for analysing the experimental data, such as the self-intermediate scattering function $F_s(q, \tau)$ and the mean square displacements $MSD(\tau)$. These quantities are defined as:

$$F_s(q, n_\tau) = \frac{1}{N_{at}} \frac{1}{N_t - n_\tau} \sum_{i=1}^{N_{at}} \sum_{j=1}^{N_t - n_\tau} \frac{1}{4\pi} \int d\Omega_q e^{i \cdot q \cdot \left[\mathbf{r}_i(n_\tau + j \cdot \Delta t) - \mathbf{r}_i(j \cdot \Delta t) \right]} \cos(\theta_{rq}) \quad (6.16)$$

$$MSD(n_\tau) = \frac{1}{N_{at}} \frac{1}{N_t - n_\tau} \sum_{i=1}^{N_{at}} \sum_{j=1}^{N_t - n_\tau} \left| \mathbf{r}_i(n_\tau + j \cdot \Delta t) - \mathbf{r}_i(j \cdot \Delta t) \right|^2 \quad (6.17)$$

where $N_{at} = 72$ in all the three cases, N_t is the number of time steps, n_τ is the correlation time step, $g(r, t_0)$ is the pair distribution function at a fixed time t_0 . The centre of mass drift was subtracted from our MD simulations, so that the position vector of atom j is written $\mathbf{r}_i(n_\tau + j \cdot \Delta t) - \mathbf{r}_i(j \cdot \Delta t)$ became

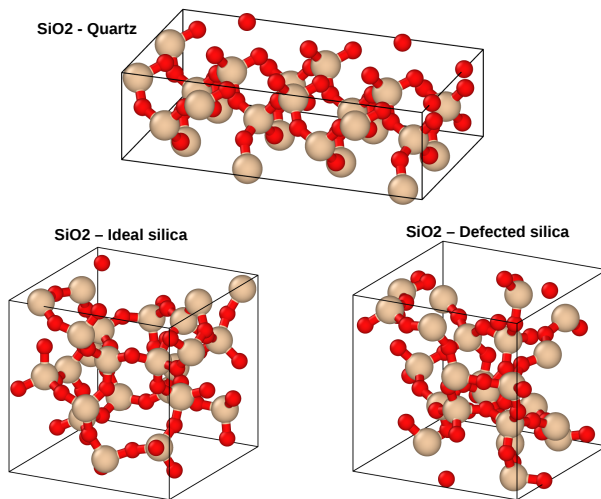


FIGURE 6.1: The three different geometries of SiO_2 studied in this work. They all contain 72 atoms (24 silicon atoms and 48 oxygen atoms). The crystal structure of quartz is tetragonal, while to simulate amorphous SiO_2 we built cubic cells of 10 \AA side.

$$\left[\mathbf{r}_i(n_\tau + j \cdot \Delta t) - \mathbf{r}_{cm}(n_\tau + j \cdot \Delta t) \right] - \left[\mathbf{r}_i(j \cdot \Delta t) - (\mathbf{r}_{cm}(j \cdot \Delta t)) \right].$$

In Fig. (6.2, 6.3, 6.4) we report the above mentioned quantities for the crystal, amorphous ideal and amorphous defected case, respectively. Ab-initio simulations proceed by optimizing the atomic positions within the supercells, and by thermalizing the systems to 300 K via a Nosè-Hoover thermostat. Adiabatic or Born-Oppenheimer (BO) and non-adiabatic (NA) simulations were performed starting from the same configuration. In the BO case electrons were assumed in their ground state for the given geometry, while in NA simulations electrons are initially excited to a low-energy excited state. In particular, NA simulations were carried out by considering only the first five excited states due to the high computational cost of these calculations with increasing number of excited states. CPMD deals with the excited states within the Linear Response TDDFT.

We can observe that for the quartz crystal structure the difference between BO and NA cases is not significant. We rationalize this similar behaviour by noticing that no empty space for the atoms to move can be found in the perfect crystal and amorphous systems, despite the excitation takes place. Possibly, to treat correctly amorphous systems a much bigger supercell than that we used here should be considered, to exclude that periodic boundary conditions force it to behave as a crystal. On the other hand,

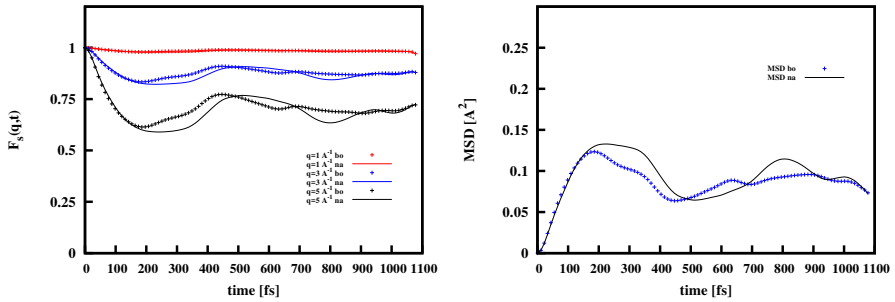


FIGURE 6.2: Left: Self part of the intermediate scattering function for the quartz crystal for different q values. Right: Mean square displacement of the atoms during the simulation. In both cases, points indicate Born-Oppenheimer, i.e. adiabatic, simulation, while continuous lines represent NAMD.

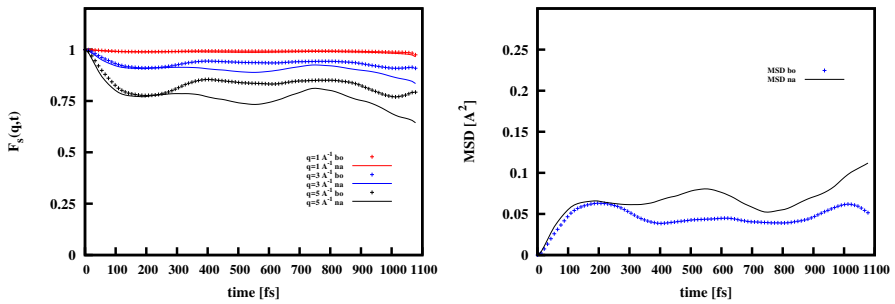


FIGURE 6.3: Same of Fig. (6.2), but for the ideal amorphous structure.

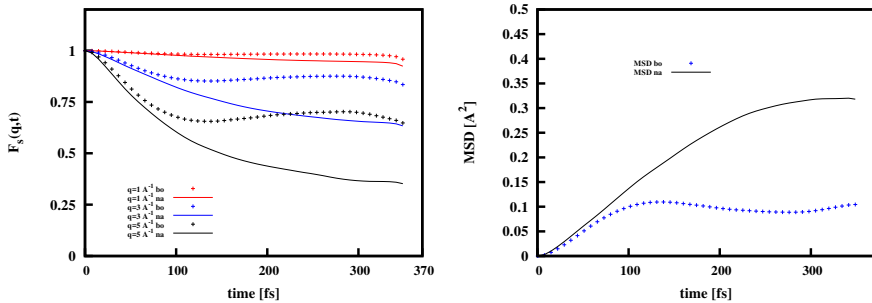


FIGURE 6.4: Same of Fig. (6.2), but for the defected amorphous structure. Simulations stop after 330 fs, due to convergence issues in the electronic structure calculations.

the difference between NA and BO in the defected amorphous structure is remarkable and the MSD and F_s functions are rather different with respect to the previous cases. However, further investigations must be performed as the self-consistency cycles to calculate the excited-state electronic structure did not reach a proper convergence.

In the nearest future we will thus try to improve the accuracy and stability of the NAMD simulations, to enlarge the simulation supercells and to achieve the picosecond time scale, in order to demonstrate that the collective atomic motion is the result of efficient energy transfer mechanisms among the electronic and nuclear degrees of freedom owing to non-adiabatic effects.

Bibliography

- [1] CPMD, <http://www.cpmc.org/>, Copyright IBM Corp 1990-2015, Copyright MPI für Festkörperforschung Stuttgart 1997-2001.
- [2] D. Marx, J. Hutter, *Ab Initio Molecular Dynamics: Basic Theory and Advanced Methods*, Cambridge University Press, 2009.
URL <https://books.google.it/books?id=VRZUw8Wk4CIC>

Conclusions

In this thesis, we presented several computational investigations with the focus on carbon-based structures, particularly at low-dimensionality where unique properties emerge. The back-bone and the theme of this thesis work are the theoretical and computational methods for treating accurately the Coulomb repulsion among the electrons.

In particular, we used state-of-the-art and developed novel computational techniques, ranging from *ab initio* approaches such as Dirac-Hartree-Fock and Density Functional Theory to the less accurate but efficient Tight Binding method. By these methods, we carried out the study of the electronic, optical and mechanical properties of systems characterised by different level of complexity, in both amorphous and crystalline phases. In several cases these systems, to the best of our knowledge, are new (e.g. bi-dimensional structures at low density and Beltrami's pseudosphere). Specifically, in the first chapter we introduced an original approach for calculating self-consistently the electronic levels of atoms and molecules using the Dirac-Hartree-Fock theory, and thus, with the inclusion of relativistic effects. The equations derived are general and can be used to model different types of interaction potentials, such as the nuclear forces.

In the second chapter we have shown that an *ab-initio* approach for calculating the dielectric properties of semiconductors and insulators is mandatory to properly take into account electronic correlation effects, such as the mixing of collective (plasmons) and single-particle excitations beyond the optical limit. From the knowledge of the dielectric function the Reflection Electron Energy Loss spectra are accurately described within Monte Carlo simulations of electron charge transport. On the other hand, for metal and semi-metal, such as graphite, a combined *ab initio* and semiclassical approach is accurate enough to understand the shape of these spectra.

Furthermore, we have studied prototype sp^2 carbon based systems at low density produced by an augmentation method using the graphene geometry as a texture. From Density Functional Theory we have obtained the electronic and mechanical properties of these systems, such as the Young's modulus, the Poisson's ratio and the stress-strain characteristics of these novel bi-dimensional materials. We found that, while lowering the density of graphene, one can retain some specific characteristic comparable to graphene, such as the Young's modulus and toughness. Nevertheless, in general the absolute values of these quantities deplete significantly for small density.

Moreover, we have presented a realistic model of SiC/SiO_x core/shell nanowire, a structure which can be possibly used in photodynamic therapy for cancer treatment. Density Functional Tight Binding simulations were carried out to study the effects of the radius size of the NW and different surface terminations on the electronic properties. In particular, measured XANES spectra were interpreted by DFT and a good agreement was found by introducing local defects into our model, especially in the case of the C-K edge. This work paves the way towards the inclusion of light sensitive porphyrin molecules in the model to be used as chromophores absorbing X-ray light within the patient body.

Finally, we developed a model of a graphene-like net over a Beltrami's pseudosphere. To that end, we developed a novel method which is able to scale up the size of all-*sp*² systems up to micrometric dimension. To compute the electronic properties in this extended systems the use of a Tight Binding approach is necessary. In this regard, we exploited the Kernel Polynomial Method to calculate the Density of States of prototypical Beltrami's pseudospheres; the latter approach avoids the diagonalization of the Hamiltonian matrix and scales linearly with the number of atoms. In particular, we were able to calculate Localized DOS resolved within the meV, which allows us to devise some fundamental hypothesis on the nature of the Dirac pseudo-particles within this structure.

This thesis deals with the theoretical and computational modelling of materials by using a variety of ab-initio approaches to accurately predict the properties of realistic structures. A number of known and novel carbon-based materials are studied, exploiting the unique versatility of carbon to bind into several bonding configurations, with the aim of tailoring their electronic and mechanical characteristics. In this regard, the methods used to carry out electronic structure simulations depend on the system size: from the Dirac-Hartree-Fock approach to model molecular properties, to Density Functional Theory used for periodic solids, such as diamond and graphene-related materials composed by a few to some hundred of atoms, to Density Functional Tight Binding or plane Tight Binding to study nanowires or Beltrami pseudospheres, which are composed by some hundreds to a few millions atoms. The details of these methods are introduced in the chapters where they are used. The criterion used to present these concepts is to organize the chapters, with the exception of the last one, according to the increasing dimension of the systems. More in details, the first chapter uses the Dirac-Hartree-Fock approach to simulate atoms and molecules, such bromotrifluoromethane; the second chapter deals with periodic systems characterized by unit cells with a relatively small number of atoms, such as diamond and graphite; the third one discusses graphene and graphene--related materials with lower density; the fourth one present a new computational and experimental model of silicon carbide nanowires coated with silicon dioxide shell; the fifth chapter is focused on the study of sp²-hybridized carbon atoms, arranged on a Beltrami surface. The latter topic spans different research fields such as geometrical topology, physics and mechanical engineering. Finally, the last chapter is dedicated to an on going work which deals with the Non-Adiabatic Molecular Dynamics simulation of amorphous silica samples where we couple the nuclear dynamic of the system to the electronic structure.

Tommaso Morresi was born in Ancona, Italy on November 16th 1986. He studied Physics at the University of Camerino and graduated with a Master's degree focusing on the simulation of the beta-decay spectra of ¹³⁸La with ab-initio methods. Then he moved to the University of Trento to complete his scientific formation with a PhD in collaboration with Fondazione Bruno Kessler and European Center for Theoretical Studies in Nuclear Physics and related areas. His research deals with the modeling and simulations with ab-initio approaches of electronic and mechanical properties of low dimensional materials and nanostructures.